MINISTÉRIO DA CIÊNCIA, TECNOLOGIA E INOVAÇÕES
INSTITUTO NACIONAL DE PESQUISAS ESPACIAIS

sid.inpe.br/mtc-m12e/2025/08.07.20.04-TDI

STUDY ON THE PROBLEM OF COOLING AND TEMPERATURE MAINTENANCE OF TEST MASSES IN CRYOGENIC LASER INTERFEROMETERS FOR GRAVITATIONAL WAVE DETECTION

Juliédson Artur Malaquias Reis

Doctorate Thesis of the Graduate Course in Astrophysics, guided by Dr. Odylio Denys de Aguiar, approved in July 24, 2025.

URL of the original document:
<http://urlib.net/8JMKD2USNRW34T/4E2JU5H>

INPE
São José dos Campos
2025

PUBLISHED BY:

Instituto Nacional de Pesquisas Espaciais - INPE
Coordenação de Ensino, Pesquisa e Extensão (COEPE)
Divisão de Biblioteca (DIBIB)
CEP 12.227-010
São José dos Campos - SP - Brasil
Tel.:(012) 3208-6923/7348
E-mail: pubtc@inpe.br

MINISTÉRIO DA CIÊNCIA, TECNOLOGIA E INOVAÇÕES
INSTITUTO NACIONAL DE PESQUISAS ESPACIAIS

sid.inpe.br/mtc-m12e/2025/08.07.20.04-TDI

STUDY ON THE PROBLEM OF COOLING AND TEMPERATURE MAINTENANCE OF TEST MASSES IN CRYOGENIC LASER INTERFEROMETERS FOR GRAVITATIONAL WAVE DETECTION

Juliédson Artur Malaquias Reis

Doctorate Thesis of the Graduate Course in Astrophysics, guided by Dr. Odylio Denys de Aguiar, approved in July 24, 2025.

URL of the original document:
<http://urlib.net/8JMKD2USNRW34T/4E2JU5H>

INPE
São José dos Campos
2025

Cataloging in Publication Data

Reis, Juliédson Artur Malaquias.

R277s Study on the problem of cooling and temperature maintenance of test masses in cryogenic laser interferometers for gravitational wave detection / Juliédson Artur Malaquias Reis. – São José dos Campos : INPE, 2025.

xxii + 131 p. ; (sid.inpe.br/mtc-m12e/2025/08.07.20.04-TDI)

Thesis (Doctorate in Astrophysics) – Instituto Nacional de Pesquisas Espaciais, São José dos Campos, 2025.

Guiding : Dr. Odylio Denys de Aguiar.

1. Cryogenic gravitational waves detectors. 2. LIGO voyager. 3. Cosmic explorer. 4. Next-generation gravitational waves detectors. 5. Silicon emissivity. I.Title.

CDU 551.511.31:543.632.492

MINISTÉRIO DA CIÊNCIA, TECNOLOGIA E INOVAÇÃO

INSTITUTO NACIONAL DE PESQUISAS ESPACIAIS

Aluno(a): Juliédson Artur Malaquias Reis

Título: "Study on the problem of cooling and temperature maintenance of test masses in cryogenic laser interferometers for gravitational wave detection"

Aprovado(a) pela Banca Examinadora em cumprimento ao requisito exigido para obtenção do Título Doutor (a) em Astrofísica

(assinado eletronicamente)
Dr. Francisco José Jablonski - Presidente da Banca (PGAST & DIAST/INPE)
(**X**) Aprovado ( ) Reprovado

(assinado eletronicamente)
Dr. Odylio Denys de Aguiar - Membro Interno – Orientador (PGAST & DIAST/INPE)
(**X**) Aprovado ( ) Reprovado

(assinado eletronicamente)
Dr. Carlos Alexandre Wuensche de Souza - Membro Interno (PGAST & DIAST/INPE)
(**X**) Aprovado ( ) Reprovado

(assinado eletronicamente)
Dr. Brian Thomas Lantz - Membro Externo (Stanford University, USA)
(**X**) Aprovado ( ) Reprovado

(assinado eletronicamente)
Dr. Elvis Camilo Ferreira - Membro Externo (IFMG)
(**X**) Aprovado ( ) Reprovado

(assinado eletronicamente)
Dr. Carlos Frajuca - Membro Externo (FURG)
(**X**) Aprovado ( ) Reprovado

Declaração de aprovação do membro estrangeiro Dr. Brian Thomas Lantz anexa ao processo.
Este trabalho foi aprovado por:

( ) maioria simples

(**X**) unanimidade

São José dos Campos, 24 de julho de 2025

Documento assinado eletronicamente por **Odylio Denys de Aguiar**, **Pesquisador**, em 25/07/2025, às 17:24 (horário oficial de Brasília), com fundamento no § 3º do art. 4º do Decreto nº 10.543, de 13 de novembro de 2020.

Documento assinado eletronicamente por **Francisco Jose Jablonksi**, **Pesquisador**, em 26/07/2025, às 08:51 (horário oficial de Brasília), com fundamento no § 3º do art. 4º do Decreto nº 10.543, de 13 de novembro de 2020.

Documento assinado eletronicamente por **Elvis Camilo Ferreira**, **Usuário Externo**, em 04/08/2025, às 16:46 (horário oficial de Brasília), com fundamento no § 3º do art. 4º do Decreto nº 10.543, de 13 de novembro de 2020.

Documento assinado eletronicamente por **Carlos Frajuca**, **Usuário Externo**, em 05/08/2025, às 10:50 (horário oficial de Brasília), com fundamento no § 3º do art. 4º do Decreto nº 10.543, de 13 de novembro de 2020.

Documento assinado eletronicamente por **Carlos Alexandre Wuensche de Souza**, **Pesquisador**, em 09/08/2025, às 05:23 (horário oficial de Brasília), com fundamento no § 3º do art. 4º do Decreto nº 10.543, de 13 de novembro de 2020.

A autenticidade deste documento pode ser conferida no site https://sei.mcti.gov.br/verifica.html, informando o código verificador **12986182** e o código CRC **54A4CD44**.

Referência: Processo nº 01340.005296/2025-23 SEI nº 12986182

*"**Santa Catharina**, nossa Padroeira*
Sede nosso guia nessa mortal carreira.
*Santa Catharina, **Mestra dos Doutores**,*
Rogai a Deus por nós, pobre pecadores."

Pia cum devotione filialiquae reverentia, haec Thesis Doctoralis
Beatissimo Domino atque Pontifici Maximo
***Leoni Papae XIV**, Ecclesiae Custodi ac Fidei Defensori atque*
***Beatae Catharinae Alexandriae**, Inclytae Martyri*
Doctorumque Patronae, gaudenter dicata est.

ACKNOWLEDGEMENTS

Sincere thanks to **God Almighty**, for the wonder created and set before our eyes, a marvel without which this study would have no purpose.

To the **One, Holy, Catholic, and Apostolic Church**, for the support throughout this journey and for making real the Eucharistic consolation for all faithful.

To my dearest **family and friends**, whose presence was indispensable through every moment shared until the completion of this thesis.

To my supervisor, **Dr. Odylio Denys de Aguir**, for his generous patience and the valuable time devoted to guiding this research.

To **INPE Astrophysics Division professors**. I also express my gratitude to the **GWINPE group collegues**, especially to Julio Martins, Ana Luisa Guimarães da Silva, and Dr. Tábata Aira Ferreira for a friendship full of scientific enthusiasm and inspiring discussions.

To **Dr. Brian O'Reilly**, coordinator of the LSC Fellows Program, who accepted me as an LLO Fellow and provided invaluable support, offering me unique opportunities to work at the LIGO Livingston Observatory. My gratitude also extends to the **LIGO Scientific Collaboration** and the **LSC Fellows Program** for granting me the privilege of contributing to one of the most fascinating scientific environments in the world. Visiting and working in LLO was a dream that came true.

To **Dr. Anamaria Effler**, an excptional LLO scientist, whose guidance led me to adventures as noise hunts along the interferometer, injections from the control room, and deep explorations into the PEM science. It was an honor to learn from her.

To all **LLO Staff**, specially to **Pricilla Godbey**, whose warmth and sincere kindness made me feel at home, despite being far from it.

To my **LLO Fellows and friends** from all over the world, especially Wenxuan, Masayuki, Maki, Abhinav, Terrence and Sushant. With them, I not only learned the art of *Mahjong* and the thrill of *Yakumans*, but also the deeper lessons of friendship and life far from home.

Finally, a special thanks goes to **CAPES**, for the commitment to funding and investing in high-quality Brazilian science.

ABSTRACT

Future ground-based gravitational wave detectors design proposes the use of cryogenics. Specifically, LIGO Voyager and Cosmic Explorer will use Silicon test masses at 123 K. On the other hand, Einstein Telescope proposes Silicon test masses at 10 K. However, it is important to know if Silicon test masses emissivity is enough to radiate power and maintain temperature. This thesis reports a series of experiments conducted with different Silicon specimens aiming to measure Silicon emissivity at cryogenic temperatures, specially at 123 K. Furthermore, it presents a model for semitransparent material effective emissivity at this low-temperature regime. The results are compared with the experimental data, and applied to estimate the effective emissivity for LIGO Voyager, Cosmic Explorer, and Einstein Telescope test masses. For Voyager and Cosmic Explorer, the estimated emissivity is $\epsilon = 0.685$ at 123 K. In contrast, for Einstein Telescope it was possible to calculate and overestimated emissivity value at 50 K, which is $\epsilon_{\mathrm{ET}} = 0.235$. The mentioned interferometers will require a cooling-down system besides maintaining the low temperature. The Gravitational Wave Group of INPE proposes a closed-loop pipeline with circulating liquid Nitrogen to create a cold environment around test masses to remove heat by radiation. Magnetically driven impellers will be responsible to pump liquid Nitrogen and generate flux. However, this mechanism will introduce Newtonian noise to the system. The impellers noise contribution to LIGO Voyager and Cosmic Explorer sensitivity curve was calculated by a new computational model. For a system using two 3-bladed impellers, the Newtonian noise is always below 1/10 of the sensitivity curve if their distance to the test mass center is greater than 2.3 m for LIGO Voyager. This critical distance is 2.4 m for Cosmic Explorer case. Moreover, There is a zero noise value for specific impeller's locations, depending on the blade number, as shown in this work. This region can be used to to minimize or mitigate Newtonian noise introduced by the impellers. Lastly, we report the work developed while the student visited the LIGO Livingston Observatory.

Keywords: Cryogenic gravitational waves detectors. LIGO Voyager. Cosmic Explorer. Next-generation gravitational waves detectors. Silicon emissivity.

ESTUDOS SOBRE O PROBLEMA DE RESFRIAMENTO E MANUTENÇÃO DA TEMPERATURA DE MASSAS TESTES EM INTERFERÔMETOS LASER CRIOGÊNICOS PARA DETECÇÃO DE ONDAS GRAVITACIONAIS

RESUMO

Detectores futuros de de ondas gravitacionais propõem o uso de criogenia. Mais especificamente, *LIGO Voyager* e *Cosmic Explorer* usarão massas de teste de silício a 123 K. Por outro lado, o design do detector *Einstein Telescope* propõe massas de teste de silício operando a 10 K. No entanto, é importante conhecer se a emissividade das massas de teste de silício é suficiente para irradiar calor por radiação e manter sua temperatura. Esta tese apresenta uma série de experimentos conduzidos usando diferentes espécimes de silício com o objetivo de medir a sua emissividade em temperaturas criogênicas, especialmente a 123 K. Além disso, apresenta um modelo para a emissividade efetiva de materiais semitransparentes neste regime de baixa temperatura. Os resultados teóricos são comparados com os dados experimentais e aplicados para estimar a emissividade efetiva para as massas de teste do *LIGO Voyager*, *Cosmic Explorer* e do *Einstein Telescope*. Para *Voyager* e o *Cosmic Explore*r, a emissividade estimada é $\epsilon = 0.685$ a 123 K. Em contrapartida, para as massas teste do *Einstein Telescope*, foi possível calcular um valor superestimado da emissividade efetiva a 50 K, que é $\epsilon_{\mathrm{ET}} = 0.235$. Espera-se um valor real menor que esse. Os interferômetros supracitados também necessitarão de um sistema de resfriamento, além de manter a temperatura de operação fixa. O Grupo de Ondas Gravitacionais do INPE (GWINPE) propõe uma tubulação em circuito fechado com nitrogênio líquido para criar uma fonte fria ao redor das massas de teste e remover o calor por radiação. Impulsores acionados magneticamente serão responsáveis por bombear o nitrogênio líquido e gerar seu fluxo. Porém, o uso desse mecanismo introduzirá ruído newtoniano ao sistema. Portanto, contribuição do ruído dos impulsores na curva de sensibilidade do *LIGO Voyager* e do *Cosmic Explorer* foi calculada por um modelo computacional. Considerando o uso de dois impulsores de 3 pás, o ruído newtoniano está sempre abaixo de 1/10 da curva de sensibilidade se sua distância até o centro da massa teste for maior que $2,3$ m para o *LIGO Voyager*. Essa distância crítica é de $2,4$ m para o *Cosmic Explorer*. Além disso, foram calculadas posições específicas do impulsor que não geram ruído newtoniano, dependendo do número de pás. Isso revelou uma nova região onde é possível minimizar ou mitigar o ruído introduzido. Por último, apresenamos as contribuições feitas durante o trabalho desenvolvido no observatório LIGO Livingston (USA).

Palavras-chave: Detectores de ondas gravitationais criogênicos. LIGO Voyager. Cosmic Explorer. Ruído newtoniano. Emissividade do Silício.

LIST OF FIGURES

Page

LIST OF TABLES

Page

CONTENTS

Page

1 INTRODUCTION

Using gravity as a foundation, Isaac Newton (1643 - 1727) showed a way for a comprehensive understanding of the Universe. This led to an unification that extended the gravitation to beyond celestial bodies and included the fall of objects on Earth, their trajectories, and other mechanical properties.

This paradigm was changed when Albert Einstein (1879 - 1955) elaborated the modern conception of gravity. In 1907, while drafting a review article on the Special Theory of Relativity, he attempted to reformulate Newtonian gravitation to align it with Relativity. As a result, Einstein proposed that the gravitational field only have relative existence, as illustrated by the free-falling person who does not perceive their own weight. This is known as the equivalence principle, one of the conceptual foundations of his theory (GAZZINELLI, 2009).

In addition to the equivalence principle, Einstein invoked the principle of covariance, which defines that natural laws must be expressed in a covariant form (FALCIANO, 2009). Under this view, coordinate systems are abstract constructions used to describe physical phenomena. These phenomena are assumed to be truly objective, i. e., remain invariant under arbitrary changes in coordinates. Therefore, the laws of nature must retain their form and validity in all reference frames, whether inertial (in the Newtonian sense) or accelerated.

This space-time theory dispenses with absolute objects, implying that accelerated observers perceive space-time with a non-Euclidean structure. Further, according to the equivalence principle, acceleration and gravitation are locally indistinguishable. Following this new way of thinking gravity, the dynamic structure of space-time defines the inertia of bodies. Then, since matter-energy is the source of gravity, it changes the structure of space-time (FALCIANO, 2009).

This conceptual development lead to a gravitational theory, known as Theory of General Relativity (GR), in which matter curves space-time, and this curvature determines the trajectories of bodies according to the geometry of curved space-time.

It was Einstein's insight that gravity is a manifestation of space-time curvature that redirected his efforts toward a mathematical formulation of General Relativity. The necessary theoretical framework was provided by his friend and former university colleague, Marcel Grossmann (GAZZINELLI, 2009), who introduced Einstein to ten-

sor calculus, the appropriate mathematical language for the theory. Together, they published an initial form of the field equations (RÄZ; SAUER, 2018).

General Relativity was thus constructed using differential geometry, where physical quantities are represented by tensors. Within this formalism, matter and energy are described by the energy-momentum tensor, which serves as the source of space-time curvature. The geometric structure of curved space-time is defined by a fundamental tensor—the metric tensor.

In 1915, Einstein published the final version of the GR, showing the Field Equations. This introduced a mathematical framework for understanding gravity not as a force, according to the Newtonian Mechanics, but the effect of space-time curvature induced by the presence of mass-energy density.

One of his theory implication is the existence of Gravitational Waves (GW), ripples in space-time that propagate through it at the speed of light. Einstein first derived the equation for gravitational waves in 1916. However, due to several conceptual and theoretical obstacles, besides the limited understanding of such phenomena at the time, even Einstein himself questioned whether gravitational waves were genuine physical phenomena or mere mathematical artifacts.

Over the decades, theoretical advancements and contributions from the scientific community clarified the nature of gravitational waves (CERVANTES-COTA et al., 2016). Their interaction with matter was characterized, along with their two polarization states, and their ability to carry energy. However, it was still needed to experimentally prove the existence of gravitational waves.

Joseph Weber began searching for gravitational waves in the 1960s by designing the first detector (WEBER, 1966). This detector consisted of a resonant aluminum bar suspended in a vacuum chamber. It was later improved, although remained sensitive only to signals from within our galaxy or its immediate surroundings (MAGGIORE, 2008). A new principle of detection was needed as an alternative to achieve a direct observation.

The use of laser interferometers for gravitational wave detection was proposed independently by several scientists, including Pirani, Gertsenshtein and Pustovoit, Weber, Weiss, and others (THORNE, 1989). Using interferometry, it would be possible to construct a long detector able to produce a measurable interference pattern when laser beams are recombined. The passage of a gravitational wave modifies the

arm lengths, while imprinting the gravitational wave signal.

In this context, the Laser Interferometer Gravitational-Wave Observatory (LIGO) sites were built. In simple words, it consists in a 4-km arm-length interferometer used to search for signals coming from the Universe. In fact, the first astrophysical gravitational wave signal was detected by LIGO in 2015 (ABBOTT et al., 2016b), inaugurating a new field in science, the Gravitational Waves Astronomy.

Nevertheless, there are numerous noise sources in a Gravitational Waves detector that make difficult signal detection. Substantial efforts have been made in order to improve interferometer sensitivity, enabling the first direct signal detection (ABBOTT et al., 2016a). One promising approach for future detectors involves the use of cryogenic technology.

Combining cryogenic temperatures with appropriate materials can improve the sensitivity of a gravitational wave detector. In particular, the cryogenic upgrade of current LIGO facilities, called LIGO Voyager, aims to reach the full instrument's potential. The knowledge learned from Voyager will benefit future third-generation detectors, as Cosmic Explorer.

As presented to the reader in the next chapters, LIGO Voyager and Cosmic Explorer will use Silicon test masses, since this material can suppress thermoelastic noise at 123 K (LIGO SCIENTIFIC COLLABORATION, 2021). However, it is essential to certify that the test mass will maintain its temperature, losing heat by radiation. In this context, remains the question of Silicon emissivity at cryogenic temperatures and, by extension, the test masses emissivity in this temperature range.

In order to address this question, this thesis reports experiments conducted in order to measure silicon emissivity at 123 K using different specimens. The experiments are complemented by a theoretical emissivity model for semitransparent materials at cryogenic temperatures. Results are applied to estimate the effective emissivity of specimens and also for LIGO Voyager, Cosmic Explorer, and the Einstein Telescope test masses.

On the other hand, cryogenic detectors will need a cooling-down system able of creating a cold environment around the test masses. The cooling-down system proposed by the Gravitational Waves Group of INPE (GWINPE) involves a closed-loop pipeline with circulating liquid Nitrogen. The pumping device can be a set of magnetically driven rotating impellers. This mechanism, however, will introduce Newto-

nian noise. In this context, a model was developed to calculate the noise contribution from the impellers.

This thesis is divided as follows: Chapter 2 presents the theoretical foundations of gravitational waves. It includes a derivation of the gravitational wave equation in vacuum, a discussion of the solution far from the source, the two polarizations, and the common astrophysical sources.

In Chapter 3, current and future gravitational wave detectors are discussed. The configuration and performance of Advanced LIGO (AdvLIGO) are presented, focusing on the instrumental noise sources that limit sensitivity. It also introduces LIGO Voyager and the designs of future detectors such as the Cosmic Explorer and the Einstein Telescope, which will operate fully or in part at cryogenic temperatures.

Chapter 4 is dedicated to describe the Silicon emissivity problem addressed in this thesis, as well as the experimental investigation conducted in order to measure this property at cryogenic temperatures. This chapter presents the theoretical background of heat transfer, describing the experimental setup, and data analysis.

The results of the emissivity measurements conducted in this work are presented in Chapters 5 and 6. Chapter 5 details the analysis performed on a well-characterized silicon specimen, based on three experimental runs. Chapter 6 presents the results from the run conducted on an irregularly shaped specimen.

Chapter 7 proposes a theoretical emissivity model for semitransparent materials at cryogenic temperatures. In order to validate this model, it was used to estimated the effective emissivity of the specimens and compare with the experimental results in Chapter 8. In addition, the model was extrapolated to estimate effective emissivity of silicon substrates in LIGO Voyager, Cosmic Explorer, and the Einstein Telescope.

Chapter 9 is dedicated to calculate the Newtonian noise induced by impellers responsible of generating liquid Nitrogen flux in the proposed cooling-down system. It calculates the critical distances and conditions under which this noise can be minimized or suppressed.

Finally, Chapter 10 presents the author's work at the LIGO Livingston Observatory (LLO) during his visit as LSC Fellow, highlighting activities aimed at improving detector's performance. It includes magnetic injection studies, analysis of physical and environmental noise coupling mechanisms, the investigation of an 83Hz noise source, and more.

In short, the components of this thesis aim to contribute to the new field of Gravitational Waves Astrophysics, more precisely on future cryogenic detectors technologies by combining theoretical modeling and experimental validation.

2 GRAVITATIONAL WAVES THEORY

2.1 Einstein's General Theory of Relativity

Published in 1915, Einstein's field equations describe the phenomenon of gravity, identifying it as the result of the curvature of spacetime due to a mass-energy density distribution. These equations, elegantly synthesized within the tensorial formalism, form the foundation of the modern understanding of gravity.

Einstein's field equations form a set of ten coupled, second order nonlinear differential equations, and can be written as:

$$G_{\mu\nu} = \frac{8\pi G}{c^4} T_{\mu\nu} \tag{2.1}$$

where $G_{\mu\nu}$ represents the Einstein tensor, G is the gravitational constant, c is the speed of light in a vacuum, and $T_{\mu\nu}$ denotes the energy-momentum tensor.

The Einstein tensor, $G_{\mu\nu}$, geometrically describes spacetime deformation caused by the presence of mass-energy, which in turn is represented by the energy-momentum tensor $T_{\mu\nu}$. For instance, one can consider the distortion of spacetime around a compact object such as a neutron star.

The Einstein tensor is defined as[1]:

$$G_{\mu\nu} = R_{\mu\nu} - \frac{1}{2} g_{\mu\nu} R \,, \tag{2.2}$$

where $R_{\mu\nu}$ is the Ricci tensor, $g_{\mu\nu}$ is the four-dimensional metric, and R is the Ricci scalar. The Greek indices range from 0 to 3, representing spacetime coordinates. Latin indices take values from 1 to 3. The Ricci curvature tensor and the Ricci scalar are derived from the Riemann tensor $R_{\sigma\mu\rho\nu}$ as follows:

$$R^{\rho}_{\mu\nu} = \Gamma^{\rho}_{\mu\nu,\sigma} - \Gamma^{\rho}_{\mu\sigma,\nu} + \Gamma^{\lambda}_{\mu\nu}\Gamma^{\rho}_{\lambda\sigma} - \Gamma^{\lambda}_{\mu\sigma}\Gamma^{\rho}_{\lambda\nu} \tag{2.3}$$

$$R_{\mu\nu} = R^{\rho}_{\mu\rho\nu} = g^{\rho\sigma} R_{\sigma\mu\rho\nu} \tag{2.4}$$

$$R = g^{\mu\nu} R_{\mu\nu} \,, \tag{2.5}$$

[1] Assuming the cosmological constant is zero.

where $\Gamma^{\mu}_{\nu\rho}$ is known as the Christoffel symbol or affine connection, given by:

$$\Gamma^{\mu}_{\nu\rho} = \frac{1}{2} g^{\mu\sigma} \left(g_{\sigma\rho,\nu} + g_{\sigma\nu,\rho} - g_{\nu\rho,\sigma} \right) . \tag{2.6}$$

Also:

$$g_{\mu\nu,\rho} = \partial_{\rho} g_{\mu\nu} = \frac{\partial g_{\mu\nu}}{\partial x^{\rho}} . \tag{2.7}$$

2.2 Far from source Gravitational Wave Equation

The gravitational wave equation, valid to regions far from the source, can be derived by linearizing Einstein's field equations. To do so, let us consider a flat spacetime described by the Minkowski metric $\eta_{\mu\nu}$, also called the flat metric. The Minkowski metric is given by:

$$\eta_{\mu\nu} = \begin{pmatrix} -1 & 0 & 0 & 0 \\ 0 & 1 & 0 & 0 \\ 0 & 0 & 1 & 0 \\ 0 & 0 & 0 & 1 \end{pmatrix} . \tag{2.8}$$

A small perturbation $h_{\mu\nu}$ is added to the flat spacetime, such that $|h_{\mu\nu}| \ll 1$. Thus, the metric is defined as:

$$g_{\mu\nu} = \eta_{\mu\nu} + h_{\mu\nu} . \tag{2.9}$$

Substituting 2.9 into the definition of the Einstein tensor (Equation 2.2) results in only linear components of $h_{\mu\nu}$:

$$G_{\mu\nu} = \frac{1}{2} \left(\partial_{\alpha}\partial_{\nu} h^{\alpha}_{\mu} + \partial_{\alpha}\partial_{\mu} h^{\alpha}_{\nu} - \partial_{\mu}\partial_{\nu} h^{\alpha}_{\nu} - \Box h_{\mu\nu} + \eta_{\mu\nu}\Box h - \eta_{\mu\nu}\partial_{\alpha}\partial_{\beta} h^{\alpha\beta} \right) , \tag{2.10}$$

where $\Box = \partial^{\alpha}\partial_{\alpha}$ is the d'Alembert operator, or wave operator, and $h = h^{\alpha}_{\alpha}$ is the trace of the metric perturbation.

This equation can be simplified by defining:

$$\bar{h}_{\mu\nu} = h_{\mu\nu} + \frac{1}{2}\eta_{\mu\nu}h \, . \tag{2.11}$$

Equation 2.11 represents the trace-reversed metric perturbation[2]. Substituting 2.11 into 2.10, we obtain:

$$G_{\mu\nu} = \frac{1}{2}\left(\partial_\alpha\partial_\nu\bar{h}^\alpha_\mu + \partial_\alpha\partial_\mu\bar{h}^\alpha_\nu - \Box\bar{h}_{\mu\nu} - \eta_{\mu\nu}\partial_\alpha\partial_\beta\bar{h}^{\alpha\beta}\right) \, . \tag{2.12}$$

By choosing an appropriate coordinate transformation, i.e., defining new coordinates $x'^\alpha = x^\alpha + \xi^\alpha\left(x^\beta\right)$ such that $|\partial_\beta\xi^\alpha| \ll 1$, and according to the Lorenz gauge[3] (also called the De Donder gauge), $\partial^\nu\bar{h}_{\mu\nu} = 0$, the Einstein tensor becomes:

$$G_{\mu\nu} = -\frac{1}{2}\Box\bar{h}_{\mu\nu} \, . \tag{2.13}$$

Substituting the linearized Einstein tensor (Equation 2.13) into the field equations (Equation 2.1):

$$\boxed{\Box\bar{h}_{\mu\nu} = -\frac{16\pi G}{c^4}T_{\mu\nu}} \tag{2.14}$$

Physically, the linearization of Einstein's field equations to derive 2.14 involves implicit approximations. First, it assumes that the bodies generating the gravitational wave move within a flat spacetime. In addition, the trajectories are defined by the mutual influence of the involved bodies. Therefore, for a given binary system, the flat spacetime $\eta_{\mu\nu}$ in which the bodies move implies that the problem is treated using only Newtonian physics, not general relativity (MAGGIORE, 2008). This should be considered when studying gravitational wave sources, adding the nonlinearity of general relativity to the solutions.

2.3 Vacuum solution

Considering that the observer is far from the source, which implies $T_{\mu\nu} = 0$, the wave equation can then be written as:

[2]It can be shown that $\bar{h}^\alpha_\alpha = -h$

[3]See Chapter 1 in Maggiore (2008) regarding the confusion over gauge naming.

$$\Box \bar{h}_{\mu\nu} = 0 \,, \tag{2.15}$$

where $\Box$ is the d'Alembertian operator defined by:

$$\Box = \nabla^2 - \frac{1}{c^2}\frac{\partial^2}{\partial t^2} \,. \tag{2.16}$$

Thus:

$$\left(\nabla^2 - \frac{1}{c^2}\frac{\partial^2}{\partial t^2}\right) \bar{h}_{\mu\nu} = 0 \,. \tag{2.17}$$

This implies that the metric perturbation propagation speed in vacuum is the same as the speed of light. Furthermore, the metric perturbations that propagate through spacetime at the speed of light, as described by Equation 2.15, are called **gravitational waves**.

2.4 Polarization of gravitational waves

The vacuum solution for the gravitational wave equation (see Equation 2.15) can be derived using another gauge (MAGGIORE, 2008) as:

$$h^{0\mu} = 0, \qquad h^i_i = 0, \qquad \partial^j h_{ij} = 0. \tag{2.18}$$

where $i, j = 1, 2, 3$, representing the spatial coordinates. These conditions define the *transverse and traceless gauge*, abbreviated as *TT gauge*. The metric perturbation under these constraints is written as $\bar{h}^{TT}_{\mu\nu}$. Since the trace is null, $\bar{h} = 0$, there is no distinction between $h^{TT}_{\mu\nu}$ and $\bar{h}^{TT}_{\mu\nu}$.

The TT gauge is particularly useful due to its great convenience, as it ensures that the metric perturbation $\bar{h}^{TT}_{\mu\nu}$ contains only physical information about the radiation (FLANAGAN; HUGHES, 2005).

Moreover, this gauge reveals that gravitational waves have two polarizations. Let's consider a metric perturbation propagating only in the direction $\hat{k}$, so that $h^{TT}_{ij} = h^{TT}_{ij}(t - z/c)$. From the Lorentz gauge, we have $\partial\, h^{TT}_{3j} = 0 \Rightarrow h^{TT}_{3j} = C^{te}$. As $h_{ij} \to 0$ with $r \to \infty$, we find $h_{3j} = 0$. This means that there is no metric perturbation in the direction of propagation of the gravitational wave. The non-zero components are, therefore, h^{TT}_{xx}, h^{TT}_{xy}, h^{TT}_{yy}, and h^{TT}_{yx}.

As a consequence of the TT gauge conditions, we can define two polarizations, termed "plus" (+) and "cross" (×), whose amplitudes are defined as $h_+ \equiv h_{xx}^{TT} = -h_{yy}^{TT}$ and $h_\times \equiv h_{xy}^{TT} = h_{yx}^{TT}$. Hence, we conclude that gravitational waves are transverse waves.

Under the TT gauge gauge, solutions to Equation 2.15 take the form $h_{ij}^{TT}(x) = e_{ij}(\mathbf{k})e^{ikx}$, where $k^\mu = (\omega/c, \mathbf{k})$ and $e_{ij}(\mathbf{k})$ is called the polarization tensor. For a monochromatic plane wave propagating in the direction $\hat{k}$, we can write:

$$h_{ij}^{TT}(t,z) = \begin{pmatrix} h_+ & h_\times & 0 \\ h_\times & -h_+ & 0 \\ 0 & 0 & 0 \end{pmatrix}_{ij} \cos\left[\omega\left(t - z/c\right)\right] \tag{2.19}$$

Assuming the propagation direction coincides with the z axis, a plus-polarized gravitational wave when interacting with matter first increase the distance between two points along the x axis, while decreasing the distance between two points in the y axis. It then decrease the particles distance along the x axis and increase it along the y axis. A cross-polarized gravitational wave presents a similar behavior interacting with matter, but rotated by 45°. Figure 2.1 illustrates this effect of each polarization on a ring of particles.

There are several gravitational wave sources, as even accelerated masses can emit such radiation (MAGGIORE, 2008). However, for low velocities and low masses, these waves have an negligible amplitude.

For instance, let's consider the following case. A pair of masses, each of 10^3 kg, separated by a rod of 10 m, rotating around their center similarly to a binary system. If it rotates at 10 cycles per second, the generated gravitational wave would have a frequency of 20 Hz. The amplitude h produced, at a wavelength distance, would be on the order of $h \sim 10^{-43}$ (SATHYAPRAKASH; SCHUTZ, 2009). Another example is provided by Weber (1961) with similar conclusions.

However, the Universe have many systems that combines large quantities of mass and high speed, comparable to the speed of light in vacuum. Therefore, these are promising candidates for the generation of gravitational waves.

In the next section, we will discuss the theory of gravitational wave generation, starting from Equation 2.21. To this end, we will use the mass quadrupole approximation and discuss the mechanism of gravitational wave generation.

Figure 2.1 - Effect of a gravitational wave passing through a ring of particles.

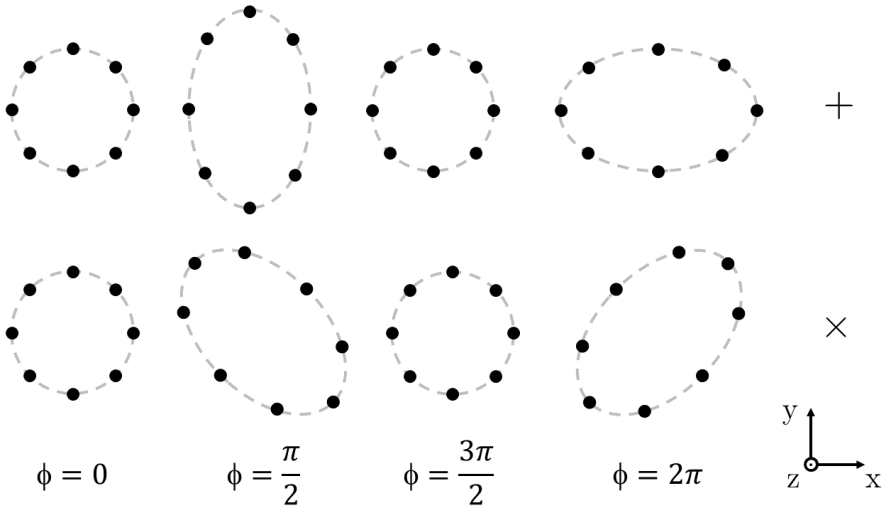

The effect of a gravitational wave passing through a ring of particles are shown for both polarizations, h_+ above and $h_\times$ below. The wave phase is indicated by ϕ, and it is assumed the propagation direction perpendicular to the surface, the z-axis direction, as indicated.

SOURCE: From the authors.

2.5 Generation of gravitational waves

Let us review the gravitational wave equation derived in Section 2.2:

$$\Box \bar{h}_{\mu\nu} = -\frac{16\pi G}{c^4} T_{\mu\nu} \tag{2.20}$$

In general, this equation can be solved using the Green's function, finding the perturbation $h_{\mu\nu}$ integrating the energy-momentum tensor $T_{\mu\nu}$:

$$h_{\mu\nu}(t, \mathbf{x}) = \frac{4G}{c^4} \int \frac{T_{\mu\nu}(\mathbf{x}, t - |\mathbf{x} - \mathbf{x}'|/c)}{|\mathbf{x} - \mathbf{x}'|} d^3x' \tag{2.21}$$

where $t_r = t - |\mathbf{x} - \mathbf{x}'|/c$ is the retarded time. Equation 2.21 can be simplified. First, it is assumed that the observer is far from the source, which implies that $\mathbf{x} \gg \mathbf{x}'$ for all points around the source, so $\frac{1}{|\mathbf{x}-\mathbf{x}'|} \approx \frac{1}{\mathbf{x}}$. Moreover, since many sources do not require a purely relativistic treatment, they can be treated in the weak-field limit, resulting in the **quadrupole momentumum** formula for gravitational radiation (MAGGIORE, 2008; KOKKOTAS, 2007):

$$h_{ij}^{TT}(t,\mathbf{x}) = \frac{1}{r}\frac{2G}{c^4}\ddot{Q}_{ij}^{TT}\left(t-\frac{x}{c}\right) \tag{2.22}$$

With this formula, one can note that the amplitude of the gravitational wave is proportional to the second derivative of the quadrupole momentum of the generating source. The quadrupole momentum is defined by:

$$Q_{ij}^{TT} = \int \rho(t,\mathbf{x})\left(x^i x^j - \frac{1}{3}r^2\delta^{ij}\right)d^3x \tag{2.23}$$

Equation 2.23 uses the transverse-traceless (TT) gauge, evaluated at the retarded time $t - r/c$, where ρ is the mass density within the volume element d^3x at position x^i.

Gravitational waves, therefore, are generated by variations in the quadrupole momentum of a system. Lower-order multipoles terms do not emit gravitational waves: the conservation of mass in the system prevents the existence of a monopole component of the radiation. Furthermore, the variation in the mass dipole moment is proportional to the system's *linear momentum*, a conserved quantity, and thus, gravitational waves cannot be produced through variations in the mass dipole moment within the framework of relativity (KOKKOTAS, 2007). In addition, there is no negative gravitational mass. Consequently, gravitational waves are at least quadrupolar in nature and are directly related to the moment of the mass distribution.

Higher-order mass moments, such as the octupole or hexadecapole moments also can generate gravitational waves. However, from such higher mass moments, the contributions are not dominant in most sources (MAGGIORE, 2008).

Finally, the total power radiated by a gravitational wave source can be calculated as a function of the quadrupole momentum of mass, more precisely, its third time derivative. Thus, using the mass quadrupole approximation, the luminosity of the source is expressed as (FLANAGAN; HUGHES, 2005):

$$L_{\mathrm{GW}} = -\frac{dE}{dt} = \frac{G}{5c^5}\left\langle \dddot{Q}_{ij}\dddot{Q}_{ij}\right\rangle \tag{2.24}$$

where the symbols $< ... >$ are a time average over several characteristic periods of the gravitational wave.

It is important to note that the approximation made through linearization, leading to the quadrupole formulas, provides a good qualitative understanding of the systems involved. For many cases, therefore, this approximation is quite robust. However, for highly relativistic sources, a more detailed description through post-Newtonian approximations or numerical relativity is necessary.

2.6 Classification of sources

It is common to classify the GW sources in four different groups considering the signal duration and the level of modeling involved. In general, they are:

a) Compact Binary Systems (CBS): these are short when compared to continuous signals, and well-defined by models. A classic example is the merger of two black holes or a pair of neutron stars. Gravitational waves generated by coalescent CBS produce signals that increase in frequency and amplitude over a short period of time. The nature of the objects involved in the system leaves an fingerprint in the signal. These signals provide relevant information about the strong gravitational field regime (ABBOTT et al., 2016b).

b) Bursts sources: these are short-duration signals. They are related to violent events in the Universe, such as supernovae. These sources are not well-modeled, a fact due to the limited understanding of the gravitational wave source.

c) Continuous Waves (CW): It is a periodic, long-duration signal (RILES, 2017). Their frequency practically does not change over time. The candidates for the source of this signal are essentially neutron stars with "mountains" on their surface.

d) Stochastic Background: long signals like continuous waves, but they are stochastic. The sum of a large number of sources results in a stochastic gravitational wave background. However, this signal can also contain a cosmological contribution, whether from the cosmic inflation period, phase transitions in the primordial universe, alternative cosmologies, or even cosmic strings (CHRISTENSEN, 2018).

Much science has been made due to detection of CBS signals. It is possible to estimate the merger rates of binary systems, whether composed of neutron stars

with black holes, black hole-only systems, or neutron star-only systems (ABBOT et al., 2018). Additionally, gravitational waves from neutron star systems can help to understand better the equation of state of these compact objects (MARKAKIS et al., 2009).

It is important to note that the nature of compact objects forming the system leaves its fingerprint on the waveform, meaning the amplitude and frequency evolution in time for a gravitational wave signal reflects whether the binary system consists of two neutron stars, two black holes, or a combination of both.

2.7 Selection of detected signals

In this Section, a selection of gravitational-wave events is presented to illustrate some of the most significant scientific contributions possible by detections of gravitational waves signals. The complete set of observed events is compiled in the Gravitational-Wave Transient Catalog (GWTC). To date, three editions of the catalog have been published (ABBOT et al., 2018; ABBOTT et al., 2021a; ABBOTT et al., 2023), with a fourth release currently in preparation.

2.7.1 GW150914: the first direct detection

The first direct detection of gravitational waves occurred on September 14, 2015, marking the beginning of gravitational-wave astronomy with the signal from black holes coalescence (ABBOTT et al., 2016b). Figure 2.2 shows the first signal detected.

This signal originated from the merger of two stellar–mass black holes with component masses of approximately $35.6^{+4.8}_{-3.0}\,M_\odot$ and $30.6^{+3.0}_{-4.4}\,M_\odot$. The final remnant was a single black hole of about $63.1^{+3.3}_{-3.0}\,M_\odot$. Therefore, approximately $3.1 \pm 0.4\ M_\odot c^2$ was radiated in form of gravitational waves within a fraction of a second.

The detection had a signal-to-noise ratio of about 24 and was observed nearly simultaneously in both LIGO detectors, with an arrival time difference of 6.9 ± 0.4 ms. The waveform matched the predictions of general relativity across the inspiral, merger, and ringdown phases, providing the first direct detection of an black hole merger. GW150914 confirmed the existence of binary black hole systems and demonstrated that such mergers occur within the age of the Universe at a rate consistent with astrophysical predictions (ABBOTT et al., 2016a).

2.7.2 GW170817: inaugurating the multimessenger astronomy with gravitational waves

On August 17, 2017, the Advanced LIGO and Advanced Virgo gravitational-wave detectors made their first observation of a binary neutron star (BNS) inspiral. The signal, named GW170817, was identified by matched filtering against post-Newtonian waveform models and presented a combined signal-to-noise ratio of 32.4 and a false-alarm-rate estimate of less than one per 8.0×10^4 years. Figure 2.3 shows the detected signal in both LIGO data and Virgo.

Surprisingly, a γ-ray burst was observed just 1.7 s after the coalescence time (ABBOTT et al., 2017a). The combination of data from the LIGO and Virgo detectors allowed a sky position localization to an area of approximately 28 deg^2, near the southern end of the constellation Hydra. This location enabled an electromagnetic

Figure 2.2 - GW150914 Signal.

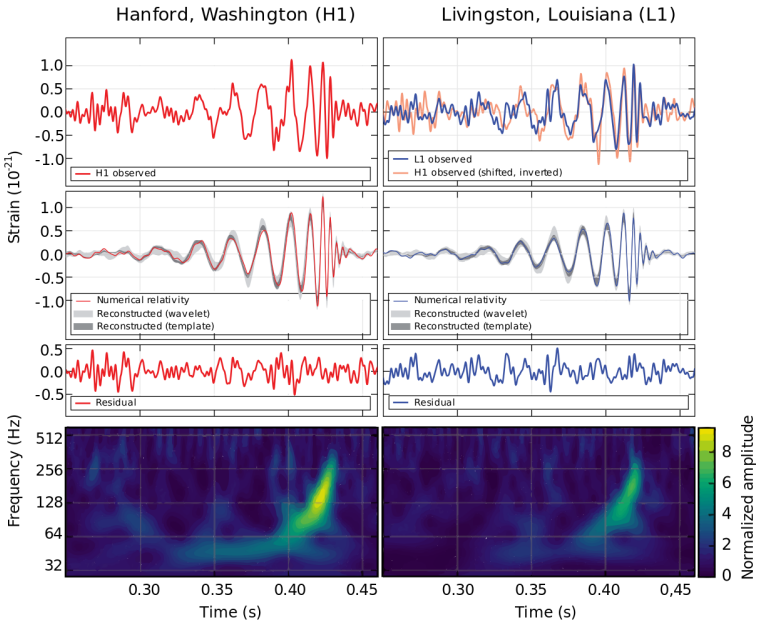

First signal observed by LIGO. The signals received by Hanford (left) and Livingston (right) detectors are shown, along with comparisons between reduced data and the theoretical prediction expected for the coalescence of two black holes. At the bottom, one can note the spectrogram to this signal, and the characteristic "chirp" shape, increasing frequency and amplitude until the merging time.

SOURCE: Abbott et al. (2016b).

follow-up campaign that identified the counterpart near the galaxy NGC4993 (ABBOTT et al., 2017b). This galaxy was consistent with the localization and distance inferred from gravitational-wave data.

Figure 2.3 - GW170817 Signal.

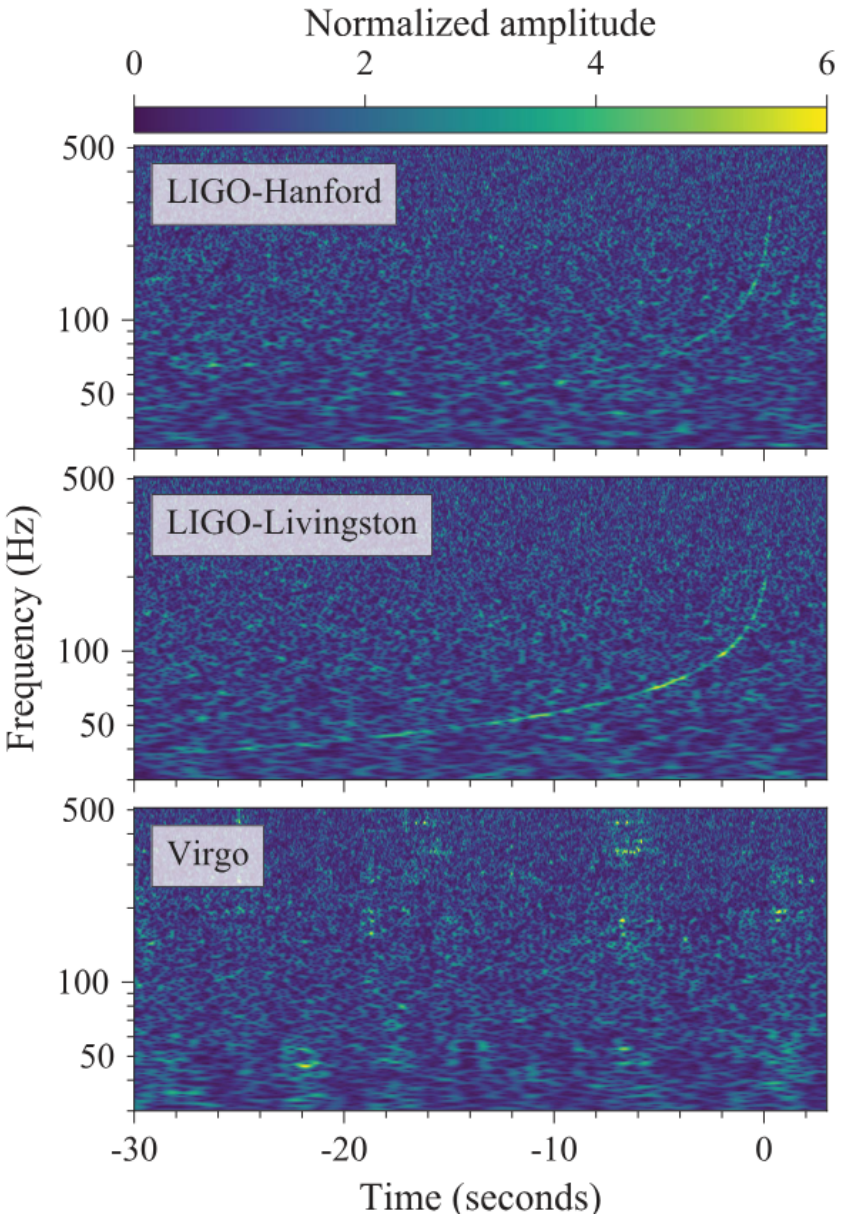

Spectrogram of data containing the GW170817 event, observed by the Hanford (top), Livingston (middle), and Virgo (bottom) detectors. Time equals to zero matches the signal peak at August 17, 2017 12:41:04 UTC. The amplitude scale in each detector is normalized to that detector's noise amplitude spectral density.

SOURCE: Abbott et al. (2017a).

Figure 2.4 - GW170817 location in sky.

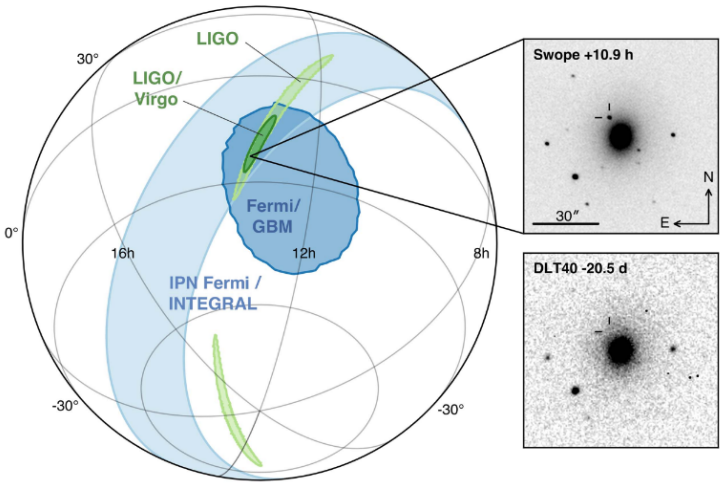

Localization of GW170817 event, gamma-ray, and optical signals. The left panel shows an orthographic projection of the 90% credible regions from LIGO, of 190 deg^2 in light green. Dark green region shows the initial LIGO-Virgo localization of 31 deg^2. Light blue shows the triangulation from the time delay between Fermi and INTEGRAL, and Fermi-GBM in dark blue. The inset shows the location of the host galaxy NGC 4993 in the Swope optical discovery image at 10.9 hours after the merger and the DLT40 pre-discovery image from 20.5 days prior to merger (bottom right). They show, by a reticle, the position of the transient in both images.

SOURCE: Abbott et al. (2017b).

The component masses of the binary was inferred to be $1.46^{+0.12}_{-0.10}\,\mathrm{M}_\odot$ and $1.27^{+0.09}_{-0.09}\,\mathrm{M}_\odot$, for the primary and secondary bodies, respectively. It is likely that the remnant of this merger is also a neutron star. By the signal, the remnant mass is expected to be between $0.86 - 2.26\ \mathrm{M}_\odot$, which is consistent with the known neutron star masses. In addition, the association with the γ-ray burst GRB 170817A (ABBOTT et al., 2017b), detected by Fermi-GBM, corroborates the hypothesis of a binary neutron star merger stead of having a black hole component.

The following identification of transient counterparts in different parts of the electromagnetic spectrum, as seen in Figure 2.4, for the same location supports the interpretation of this event as a neutron star merger. This was the first signal from two neutron stars, which had an associated electromagnetic counterpart, opening the way for gravitational waves in multi-messenger astronomy (ABBOTT et al., 2017a).

2.7.3 GW200115: the first neutron star–black hole merger detected by the network

On January 15, 2020, during the third observing run, the LIGO and Virgo observatories detected the GW200115 event, the first confidently confirmed merger between a neutron star and a black hole (NSBH). This was the first signal of this nature detected by the three observatories in a network, what gave this event high confidence of its astrophysical in origin.

Analysis of the waveform indicates a primary mass, for the black hole, of $5.7^{+1.8}_{-2.1}\,\mathrm{M}_\odot$. This is above the known neutron stars masses (FONSECA et al., 2021). The secondary mass, for the neutron star, was estimated in $1.5^{+0.7}_{-0.3}\,\mathrm{M}_\odot$, consistent with the expected for a neutron star. The luminosity distance was estimated at 300^{+150}_{-100} Mpc.

GW200115 represents a milestone in gravitational-wave astrophysics by confirming the existence of neutron star–black hole binaries, side to GW200105 (ABBOTT et al., 2021b). Analysing both signals, it was possible to model the system's formation, suggesting they form through isolated binary evolution, particularly in environments with sub-solar metallicity (CHATTOPADHYAY et al., 2022). In addition, combining the signal data and electromagnetic flux upper limits, since it was not detected an electromagnetic counterpart, it is possible to constraint the neutron star magnetic field to be $\leq 10^{15}$ G (D'ORAZIO et al., 2022).

2.7.4 GW230529: evidence for compact objects in the low-mass gap

During the O4 observing run, on May 29, 2023, LIGO Livingston detected the GW230529 event (ABAC et al., 2024), while Hanford and Virgo were offline. KAGRA was in observing mode, but its sensitivity was insufficient to impact this event analysis. Despite being a single-detector detection, three independent search pipelines confidently identified the signal as astrophysical.

Parameter estimation favors a binary with component masses of $3.6^{+0.8}_{-1.2}\,\mathrm{M}_\odot$ and $1.4^{+0.6}_{-0.2}\,\mathrm{M}_\odot$, resulting in a mass ratio of $q \approx 0.39^{+0.41}_{-0.12}$. The luminosity distance was estimated at 201^{+102}_{-96} Mpc.

The lighter object mass strongly suggests it is a neutron star, while the heavier body lies within the lower mass gap, i. e., between the heaviest neutron stars and the lightest black holes. The most probable interpretation is thus a NSBH merger, although the primary mass nature is not well defined. This event provides an evidence that compact objects may populate the 3–5 $\mathrm{M}_\odot$ gap.

Figure 2.5 - GW231123 Signal.

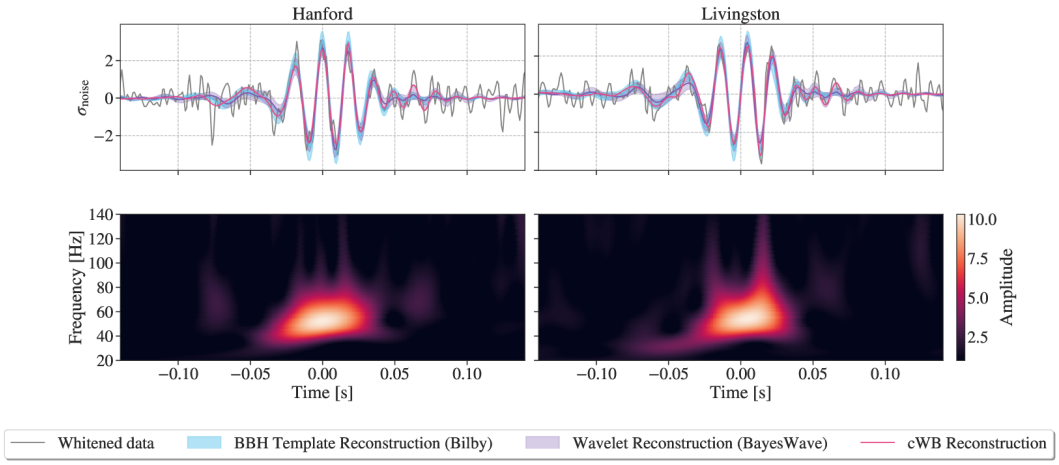

GW231123 signal as observed by the LIGO Hanford (left) and LIGO Livingston (right). Time is measured relative to the merger. The top plots show data (in black) whitened and bandpass-filtered. Also, in red, the estimated waveform from the cWB-BBH search. The bottom plots display the corresponding whitened time-frequency representations of the strain data, obtained using a wavelet transform.

SOURCE: Abac et al. (2025).

2.7.5 GW231123: BBH with extreme mass and spin

On November 23, 2023, both LIGO interferometers observed the signal of GW231123 (ABAC et al., 2025), which lasted less than 0.1 s and was recovered with high significance, with a network signal-to-noise ratio of about 22.5. Its short duration indicated a very massive binary system, merging in the frequency band of 30–80 Hz, as shown in Figure 2.5.

This signal was produced by a Binary Black Hole (BBH) merger. The estimated primary mass is $137^{+22}_{-17}\,M_\odot$ and $103^{+20}_{-52}\,M_\odot$ (90% credible intervals). From this merger, there is a remnant black hole with a mass of $225^{+26}_{-43}\,M_\odot$. Both components were inferred to have high spins, $\chi_1 \approx 0.90^{+0.10}_{-0.19}$ and $\chi_2 \approx 0.80^{+0.20}_{-0.51}$. The source was located at a luminosity distance of 0.7–4.1 Gpc, corresponding to a redshift of $z \approx 0.39$.

This system challenges the current black-hole formation paradigm. The masses place at least one component within the pair-instability mass gap (WOOSLEY; HEGER, 2021), where stellar evolution predicts no black-hole remnants. The high spins and extreme masses suggest a hierarchical merger origin in dense astrophysical environments (ABAC et al., 2025), such as globular clusters or active galactic nucleus disks.

GW231123 is the most massive binary black hole detected to date and produced a remnant in the intermediate-mass black hole regime, i. e., a black hole heavier than those formed from stellar collapse, although much lighter than the supermassive black holes in galaxies' center. It is also the fastest-spinning black hole binary confidently observed, setting new constraints on compact binary formation mechanisms.

2.8 Chapter summary

This chapter covered the fundamental principles of gravitational waves. By linearizing Einstein's field equations under weak-field conditions, considering flat spacetime, a small metric perturbation, and the transverse-traceless gauge we deduced the gravitational wave valid to regions far from source (Equation 2.14). We also explored the characteristic polarization modes ($+$ and $\times$). Thereafter, we explored gravitational wave generation, showing that leading-order term for emission comes from the second time derivative of the quadrupole moment. A common classification of astrophysical sources was presented, including examples of them, such as compact binary systems, asymmetric supernovae, deformed neutron stars, and others. Finally, we highlighted some remarking signals detected by LIGO instruments or LIGO-VIRGO-KAGRA (LVK) Collaboration.

The next chapter will cover gravitational wave detectors, noise sources, and future perspectives.

3 GRAVITATIONAL WAVES DETECTORS

Gravitational waves can be detected using different instruments and techniques. These include resonant-mass detectors (AGUIAR, 2010), ground-based and space-based interferometers (NI, 2024; FREISE; STRAIN, 2015), and also Pulsar Time Arrays (PTA) (MAIORANO et al., 2021). In this work, we focus on ground-based interferometric detectors, as such LIGO (AASI et al., 2015).

Following the General Theory of Relativity, we known that spacetime geometry dictates how particles move in it, including photons. In addition, the time a photon spend to travel from one point to another also depends on spacetime geometry. On the other hand, gravitational waves are oscillations in spacetime, which propagates at the speed of light. Therefore, we can conclude that the same photon would spend a different amount of time to travel between two positions depending on the presence of a gravitational wave. In addition, it is possible to detect these perturbations in spacetime by measuring changes in the travel time by photons.

Following this thought, an interferometer looks to be a promising instrument to detect gravitational waves. This idea was independently proposed by several scientists, including Pirani, Gertsenshtein, Pusttovoit, Weber, Weiss, among others (THORNE, 1989).

An interferometric detector can be basically understood as a laser beam split in two perpendicular ones, which travels trough the interferometer arms. Once reflected by the suspended mirrors at the end, back to the beam splitter, the beams are recombined and directed to a photodetector. The distance from the beam splitter to the end mirrors is adjusted to ensure destructive interference. These mirrors are isolated to work as nearly free test masses as possible (WEISS, 2019).

Ideally, no light signal is detected by the photodetector. However, when a gravitational wave passes through the interferometer, it changes the arm lengths, increasing one light path while decreasing other one. The mirrors will follow the distortion of space-time, measuring the change in length of the detector's arms through interferometry. As a result, the recombination of the laser beams no longer results in destructive interference. In other words, the photodetector registers a light signal, recorder as a time series, from which information about the gravitational wave can be extracted. This instrument can, basically, convert a gravitational wave signal into a laser intensity signal read by a photodiode.

As shown by Maggiore (2008), considering a simple Michelson interferometer as a detector, the arm length L can be estimated by:

$$L \approx 750\,\text{km} \left(\frac{100\,\text{Hz}}{f_{gw}}\right) \tag{3.1}$$

where f_{gw} is the frequency of the gravitational wave. It can be noted that detecting a signal at a frequency of 100 Hz requires an interferometer of 750 km arm length. Evidently, this is impractical and extremely expensive to build.

Nevertheless, the operational detectors are interferometers with arms that are 4 km in length. This is much shorter than the mentioned result of $L = 750$ km. The following section will conceptually discuss how it is possible to construct a detector sensitive enough to detect a gravitational wave signal with an interferometer arm length of "only" 4km. This is a relatively simple instrument when compared to those currently in operation, which include a series of improvements that will be discussed bellow.

3.1 Advanced LIGO (aLIGO)

In order to achieve the required sensitivity to detect a gravitational wave signal, several improvements must be done to a Michelson interferometer. In this section, we will briefly discuss these enhancements, which enabled the first direct detection of gravitational waves.

The first LIGO detectors, also known as Initial LIGO, were a pair of 4 km interferometers built in the late 1990s at two different sites: one in Livingston (Louisiana) and one in Hanford (Washington), separated by approximately $3,000$ km. This first generation of interferometers was unable to detect gravitational waves.

The current LIGO detectors, known as Advanced LIGO, form the second generation of interferometers designed to operate at the two facilities. Their simplified optical layout is shown in Figure 3.1. It was designed to improve sensitivity from the initial LIGO by a factor of 10, which means increasing the number of detectable sources by a factor of 10^3.

Technically, aLIGO can be defined as a Michelson interferometer with Fabry-Perot cavities, power recycling cavities, and signal recycling. It is referred to as the "Dual-recycled Fabry-Perot Michelson interferometer".

Figure 3.1 - Schematic of the Advanced LIGO optical system.

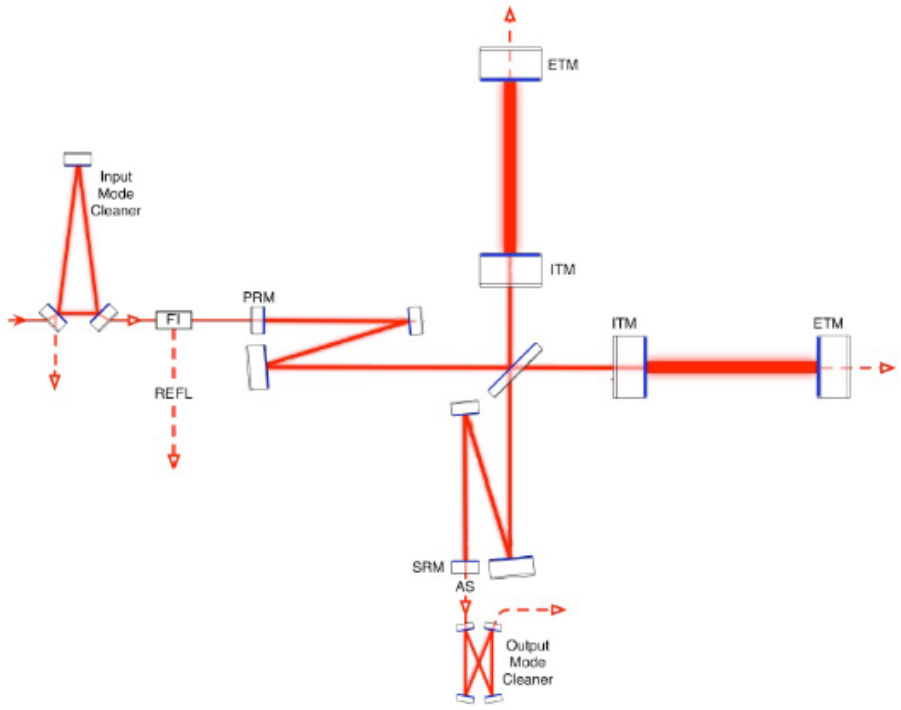

Representation of the Advanced LIGO optical system. After leaving the input source, the laser passes through an amplitude and frequency cleaning module (input mode cleaner - IMC), then reaches the Faraday isolator (FI), enters the power recycling mirror (PRM), is split by the beam splitter, and travels through the interferometer arms. The Fabry-Perot cavities are formed between the test masses described by ITM (Input Test Mass) and ETM (End Test Mass). Since the beams are recombined, the laser (possibly with a gravitational wave signal) passes through the signal recycling mirror (SRM), the output mode cleaner, and then reaches the photodetector.

SOURCE: Adapted from Waldman (2011) by Constancio et al. (2020).

In order to reach the designed sensitivity, the laser and input optical subsystems must be able to generate 125 W laser beam. This will keep the photon shot noise at a lower level (Subsection 3.2.2). The same laser beam must propagate through the 4 km arms in such a way that it does not spread and exceed the test mass surface. The laser wavelength is 1064 nm.

Each arm have an "input mirror"[1] placed near to the beam splitter in order to form two Fabry-Perot cavities. This cavity consists of a pair of mirrors: the Intermediate Test Mass (ITM) and the End Test Mass (ETM). Their reflective faces are directed

[1]This is a semitransparent mirror, unlike the test masses at the End Stations, which can reflect about 99.99% the incident light (MCIVER; SHOEMAKER, 2021).

toward each other, confining the laser beam. By adjusting the correct frequency, a resonance is generated inside the cavity (MCIVER; SHOEMAKER, 2021), which significantly increases the optical path and the power of the incident laser on the test masses (MAGGIORE, 2008).

The End Station mirrors, also known as End Test Masses (ETM), play a fundamental role, as they serve as test masses and reflective surfaces for the laser beam. They are made of fused silica and have a cylindrical shape with a diameter of 34 cm and a length of 20 cm. Their mass is 40 kg. Additionally, the test masses must reflect most of the laser, absorbing as little as possible, avoid to scatter the photons, minimize thermal friction noise (subsection 3.2.1), and resist to radiation pressure by their inertia.

Other improvements can also be considered, such as power recycling cavity (PRC). When the laser is recombined at the beam splitter, part of the light returns to the source. It is possible to place a partially reflective mirror between the laser source and the beam splitter, in such a way that the light from the interferometer is reflected in phase with the input light. This forms another cavity capable of generating a resonance that increases laser intensity and contributes to the sensitivity (KAWAMURA; NAKANO, 2019).

Another semitransparent mirror, called the signal recycling mirror (SRM), can be placed at the output of the interferometer, i.e., between the beam splitter and the photodetector. According to Mciver and Shoemaker (2021), signal recycling can be thought of as an additional resonant cavity formed not for light, but for the gravitational wave signal. Given a position for this mirror, the sensitivity of the detector increases for a certain frequency range, but the detector's bandwidth is reduced.

As a result, small adjustments to the SRM position can tune the sensitivity for a specific gravitational wave source or even increase the bandwidth of the detector, costing sensitivity in that band (MAGGIORE, 2008).

The aLIGO also includes: a noise filtering system for frequency and amplitude to provide a stable beam for the interferometer; a Faraday isolator (FI) to reflect laser from the interferometer for control loops, preventing it from reaching the injection system; and a seismic isolation and suspension system with pendulums controlling the test masses positions while reducing seismic noise (Subsection 3.2.3).

In summary, Advanced LIGO have test masses made of fused silica, each weighing 40 kg, suspended by SiO_2 fibers at room temperature. The laser has an initial injected power of 125 W and reaches 800 kW in the arms. The laser wavelength is 1064 nm.

However, although it is a extraordinary instrument for detecting gravitational waves, the interferometers like Advanced LIGO presents several sensitivity-limiting noises. These will be discussed below.

3.2 Advanced LIGO instrumental noise

There are several noise sources in interferometric detectors. Some are transient, i.e., they are limited in time. Transient noise includes environmental and unknown noise sources. Physical and environmental noises are produced by the nature or by human activities, just as excess of ground motion produced by earthquakes, electromagnetic interferences due to a thunderstorm, high-speed wind, scattered light, etc.

On the other hand, there are also permanent noises forming a baseline level of noise in the detector's sensitivity curve, also known as the budget noise. Each noise budget component contributes to the total noise, shown in dark gray in Figure 3.2.

Furthermore, ongoing run noise budget can also include unknown components. The real picture can be very different, since it may present more or less transient noise generated by earthquakes, thunderstorms, scattered light, etc. Also, non-transient noise onsite generated by unknown sources can also last for long periods of time until be mitigated, as the 83.15 Hz line mentioned in Chapter 10. Several factors can effect the resulting sensitivity curve. Figure 3.3 presents the current understanding of limiting noise sources based on O3, showing the budget for both observatories. One can note the several different contributions to the total measured noise.

The detector's sensitivity can also be quantified by the Binary Neutron Star (BNS) Range. This is defined as the maximum distance at BNS gravitational wave signal can be detected, considering the detector's antenna pattern and the distribution of sources in the sky. By default, it is used a BNS system with equal masses of $1.4\,M_{\odot}$, and a signal-to-noise ratio (SNR) of 8.

During O4a, LLO and LHO reached BNS ranges of 160 Mpc and 150 Mpc, respectively. During O4b, these ranges improved to 170 Mpc for LLO and 160 Mpc for LHO. In addition, it is expected a BNS range of 190 Mpc for aLIGO operating with design sensitivity.

Figure 3.2 - Noise budget of aLIGO.

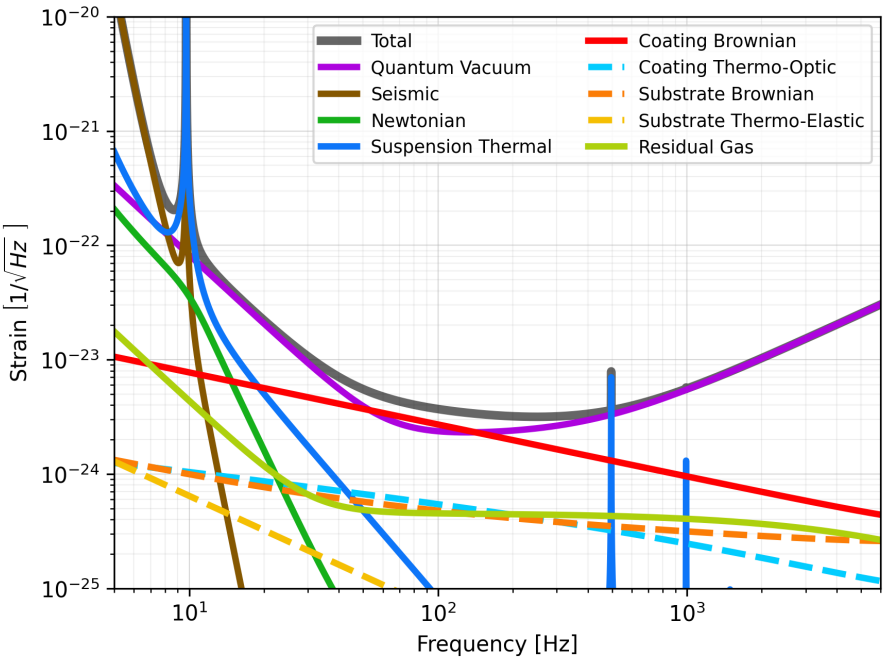

SOURCE: Rollins et al. (2020).

Concerning the noise sources in aLIGO budget, we highlight the major sources: thermal noise, quantum noise, seismic noise, and Newtonian noise. These major sources are discusses bellow.

3.2.1 Thermal noise

In mechanical experiments, thermal noise is one of the most fundamental sources of noise. It also plays an important role limiting the gravitational wave detectors sensitivity (WEISS, 2019).

Thermal motion in the test mass substrate, optical coating and suspension cause displacement noise in DARM (Differential Arm Length). Among these, for Advanced LIGO, the dominant source is the coating Brownian noise (AASI et al., 2015). It arrives from Brownian motion in the mirror coatings and limits the sensitivity around 100 Hz. The optical coatings are made of alternate multilayers of low and high-index of refraction materials. Advanced LIGO uses silica (SiO_2) as low index material, and titania doped with Tantala (TiO_2:Ta_2O_5) as high index one (BUIKEMA et al., 2020).

The suspension system was designed to limit its thermal noise into a known mea-

Figure 3.3 - Full noise budget of LIGO detectors during O3.

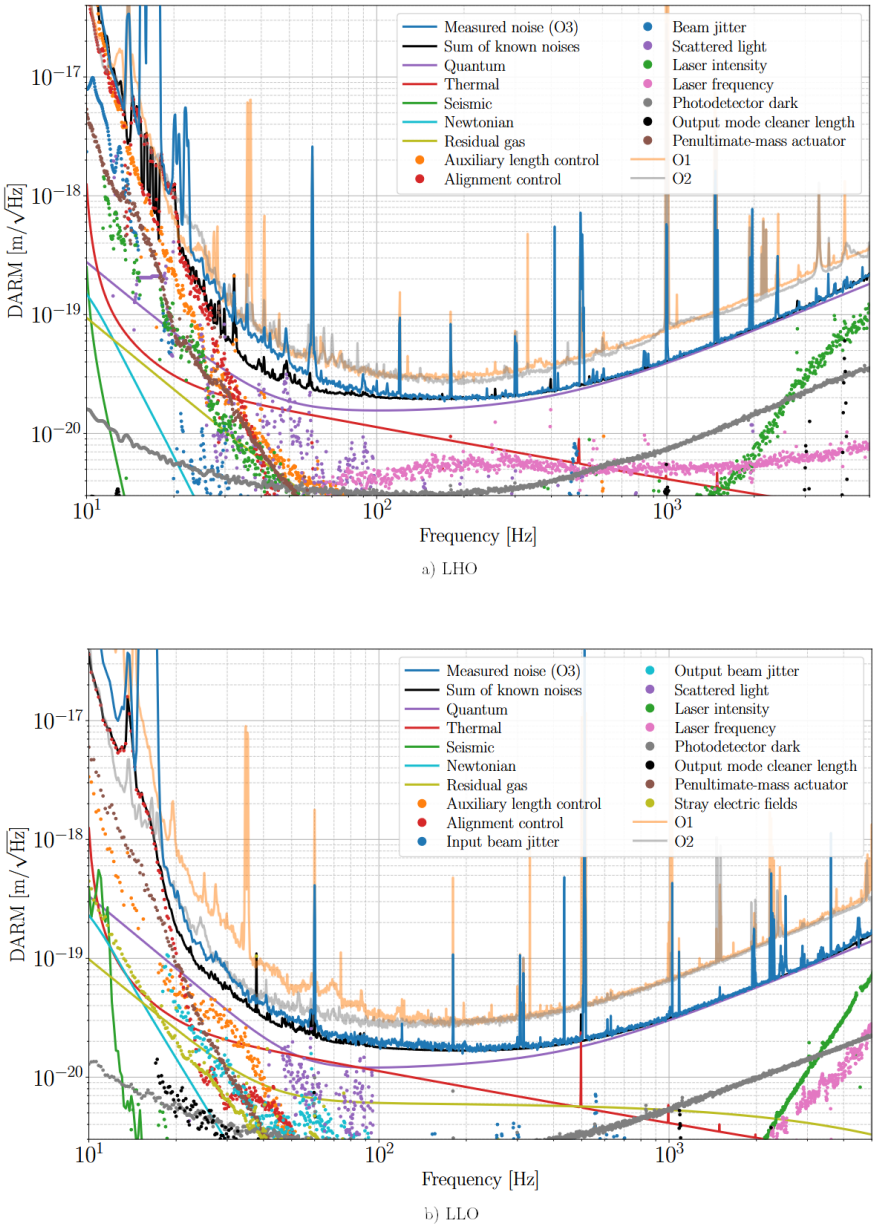

Full noise budget for both LIGO detectors: (a) for LIGO Hanford Observatory (LHO) and (b) for LIGO Livingston Observatory (LLO). Calculated noise components are shown in solid lines and measured ones are shown by dots.

SOURCE: Buikema et al. (2020).

surement band. Also the substrate is made of a material of low mechanical loss and, fused silica, also to minimize thermal noise (BUIKEMA et al., 2020).

Statistical fluctuations in the temperature of the material causes thermoelastic noise. Variable temperature gradient induces thermal displacements through the linear thermal expansion coefficient. This applies to the suspension fibers, the test mass substrates and coatings (ROWAN, 2019).

3.2.2 Quantum noise

Quantum noise limits LIGO sensitivity's across most of the astrophysical band (CAPOTE et al., 2024) and it is intrinsically related to the quantum nature of light, i.e., its discrete nature. There are two ways in which quantum noise is present in the interferometer: quantum radiation pressure noise, and photon shot noise.

It is known that, due to its quantum nature, the laser light carries uncertainty in its amplitude and phase. Quantum radiation pressure noise arises from fluctuations in the laser amplitude (MCCLELLAND et al., 2019). In order to understand it, one can associate light amplitude fluctuations to variations in the number of photons colliding with the test masses. Consequently, this causes a fluctuating momentum on the interferometer optics which leads to displacement noise (BUIKEMA et al., 2020). This noise increases with laser power and can be a limiting source below ≈ 50 Hz (CAPOTE et al., 2024).

Shot noise, on the other hand, is related to statistical fluctuations in the arrival time of photons at the interferometer output. Furthermore, because it follows a Poisson distribution, it is a frequency independent noise (AASI et al., 2015), decreases with laser power (CAPOTE et al., 2024), and dominates the high-frequency region of the spectrum (BUIKEMA et al., 2020).

Although it is not possible to remove the quantum noise, Heisenberg uncertainty principle allows to redistribute this noise in amplitude and phase quadratures. "Squeezing" the phase quadrature leads to anti-squeezing the amplitude one. Hence, it can lower shot noise floor, but also leads to raising quantum radiation pressure, since it is anti-squeezing the amplitude quadrature.

The non-classical states of light, the "squeezed vacuum", began to be injected in LIGO detector in O3 (GANAPATHY et al., 2023). Therefore, shot noise was reduced using this technique, the squeezed injection in the phase quadrature. The raised quantum radiation pressure was acceptable because it does not dominate the low frequency band (BUIKEMA et al., 2020).

During O4a, a new Squeezing method was implemented: the frequency-dependent squeezed vacuum. The O3 LIGO squeezer produces squeezed vacuum around the interferometer laser frequency, by the optical parametric oscillator (OPO). Then the squeezed light undergoes a frequency-dependent phase shift by reflecting inside a new filter cavity installed at the facilities. It produces a frequency-dependent rotation in the squeezed state, according with the cavity resonance frequency (GANAPATHY et al., 2023). Other optic components were improved to O4, reducing squeezing losses (CAPOTE et al., 2024).

It was the first demonstration of the frequency-dependent squeezing of light on real gravitational wave detectors. Figure 3.4 shows a comparison to both detectors, LLO and LHO. The unsqueezed states are shown in black. The frequency-independent squeezing (without filter cavity) are in green, which has high-squeezing. In purple, the frequency-depended phase rotation action on the squeezed light lowered the noise budget. Non-quantum noises are also shown, as a model for unsqueezed quantum noise.

3.2.3 Seismic noise

At low frequencies, seismic and Newtonian noise dominate (WEISS, 2019). These types of noise have been systematically reduced over the years and across generations of detectors due to improvements in suspension and vibration isolation systems (BRAND, 2019).

Seismic noise is caused by seismic waves, i.e., the ground movements, and can be understood as a stochastic process. Several types of noise contribute to this category. We highlight: i) slow ground motion caused by the gravitational forces experienced by Earth's surface (due to the Sun and the Moon); ii) large movements of the ground, such as earthquakes, or microseismic noise caused by cyclones, ocean waves crashing against the shore, and monsoon winds; iii) seismic noise produced by human activity (cultural or anthropogenic seismic noise); iv) wind noise, or seismic movements correlated with the wind speed in the environment surrounding the detector.

Advanced LIGO test masses are in the bottom of a quadruple pendulum chain (BRAND, 2019). This is because this chain can reduce coupling of ground motion to the test mass. Therefore, the pendulums are suspended from seismic isolation platforms. This design ensures that a minimum amount of seismic noise contaminates the gravitational wave band.

Figure 3.4 - Advanced LIGO noise budget comparison using frequency-dependent squeezing.

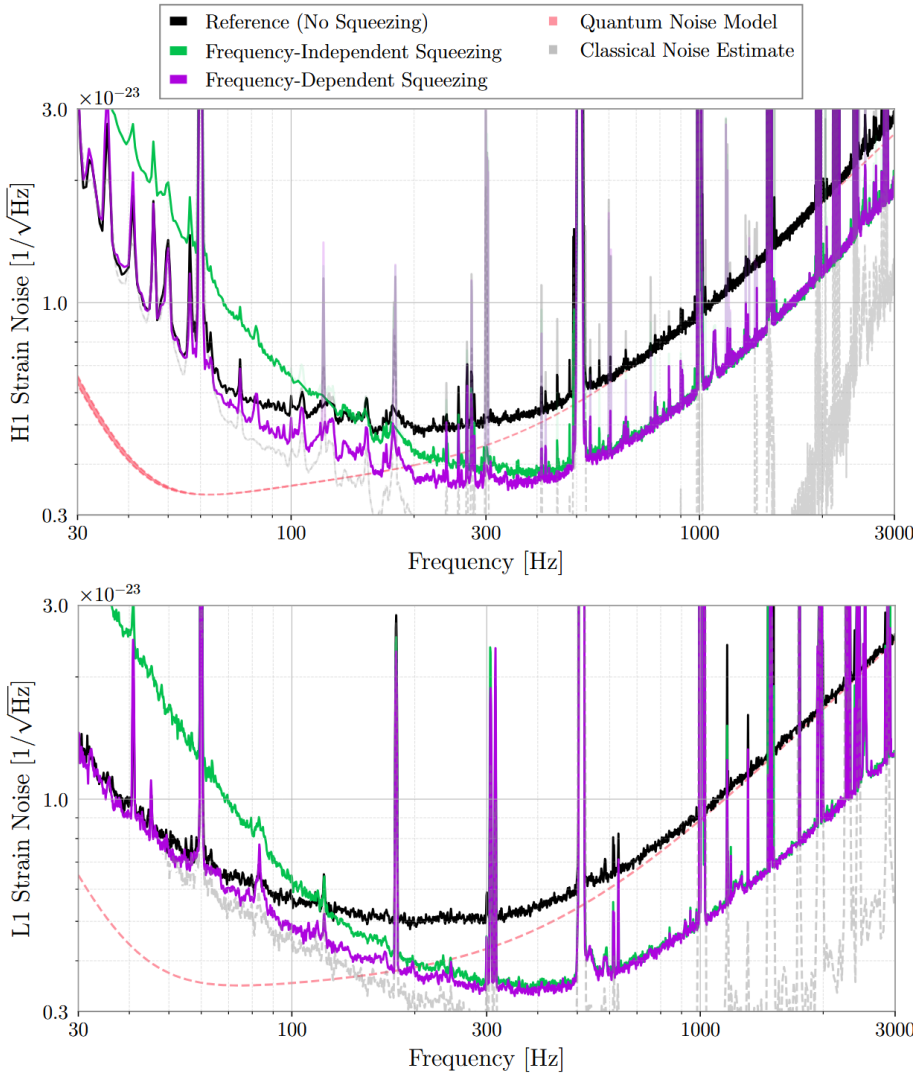

Frequency-dependent squeezing in LIGO detectors. The plots show strain noise spectra for LHO (H1) and LLO (L1) in amplitude spectral density units. No squeezing spectra are shown in black. Frequency independent squeezing spectra are shown in green and frequency-dependent squeezing spectra are shown in purple. Also, estimations for classical noises (non-quantum) and a quantum noise model are shown in gray and red, respectively.

SOURCE: Ganapathy et al. (2023).

3.2.4 Newtonian noise

Newtonian noise, also known as gravity-gradient noise, arises from fluctuations in the gravitational field that couples directly to the test masses, exerting varying gravitational forces on them (AASI et al., 2015). These variations can have seismic and atmospheric origins. Also, as we will show in Chapter 9, instruments working in the interferometer can also produce Newtonian noise. Considering them and the calculating the noise magnitude it introduces can shed light in the design choices.

It is expected Newtonian noise dominates aLIGO design sensitivity curve from 10 Hz to 20 Hz, although it was not observed in the detectors at the time of this writing (BUIKEMA et al., 2020). A more detailed discussion of seismic and Newtonian noise can be found in Brand (2019).

3.2.5 Other noise sources

There are, still, some noise sources which is important to mention briefly, since them also contribute to noise budget. More details in (BUIKEMA et al., 2020).

Laser frequency fluctuations results in noise, since variations in frequency can mimic a changing in the detector's arm length. Therefore, the control loops can wrongly correct for the optics positions. On the other side, intensity fluctuations can also produce noise. One can relate laser intensity variations to the changing number of photons reaching the mirrors. This can lead to a displacement noise and, once again, the control loops can correct something that is not real.

Scattered light is another prominent noise. Photons can leave the beam path, reflect on any surface inside the interferometer, and then recombine with the original laser. These photons will absorb energy from the moving walls and, reaching the dark port, introducing noise. Baffles and beam dumps are used to reduce scattered noise.

Advanced LIGO works under high vacuum. However, this is not perfect. Residual gas can cause phase noise when interacting with the laser beam. Also, it can transfer linear momentum to optics.

3.3 LIGO Voyager

It is expected the current LIGO detectors to reach their designed sensitivity in the next few years. In addition, improvements will reduce noise sources, including quantum noise through frequency-dependent squeezed light, and thermal noise by

improving the coating of the test masses. This upgrade is called "LIGO A+" and aims to improve sensitivity by approximately a factor of 2 (MCIVER; SHOEMAKER, 2021), which corresponds to an increase of 8 times in the event rate detection.

However, there is a substantial and ambitious upgrade called LIGO Voyager. This will involve reducing several types of noise: quantum noise, thermal noise from the test masses and suspension, and Newtonian noise.

LIGO Voyager was designed to achieve the maximum performance that the LIGO facilities can offer. This means that much of the current infrastructure will be reused. For instance, the system with two Fabry-Perrot cavities, as well as the power and signal recycling, will remain as in the design of Advanced LIGO and A+ (MANSELL, 2018).

Moreover, the novel aspect of LIGO Voyager is to use cryogenics to cool the test masses and maintain their temperature at 123 K. Other significant changes will include the wavelength of the laser, the use of a frequency-dependent squeezed light injection (as in aLIGO), and the combination of seismometers with an adaptive noise regression system (ADHIKARI et al., 2020).

Voyager test masses are planned to be bigger than Advanced LIGO. The designed one are cylindrical mirrors made of Silicon (Si), with a diameter of 450 mm, a length of 550 mm, and 200 kg. Figure 3.5 shows the End Test Mass (ETM) design, where the mirror is surrounded by two independent shields. This new configuration will reduce the Brownian noise from the mirror coating and provide greater inertial resistance to disturbances from radiation pressure forces.

Figure 3.6 shows the theoretical noise budget for LIGO Voyager. The test masses substrate will be made of Silicon (Si), due to several advantages that this material presents, as shown by Adhikari et al. (2020).

The major component of thermal noise in Advanced LIGO is Brownian noise, produced by the fused silica test masses. However, Si has low mechanical dissipation, and consequently, lower Brownian noise.

On the other hand, thermoelastic noise emerges as a prominent noise source due to its high thermal conductivity. As mentioned before, thermodynamic fluctuations of heat in the substrate are the source of this noise (Subsection 3.2.1). These fluctuations produce surface displacements of the mirror via the thermal expansion coefficient α. The spectral density of power for thermoelastic noise is proportional

Figure 3.5 - Schematic view of the LIGO Voyager test masses.

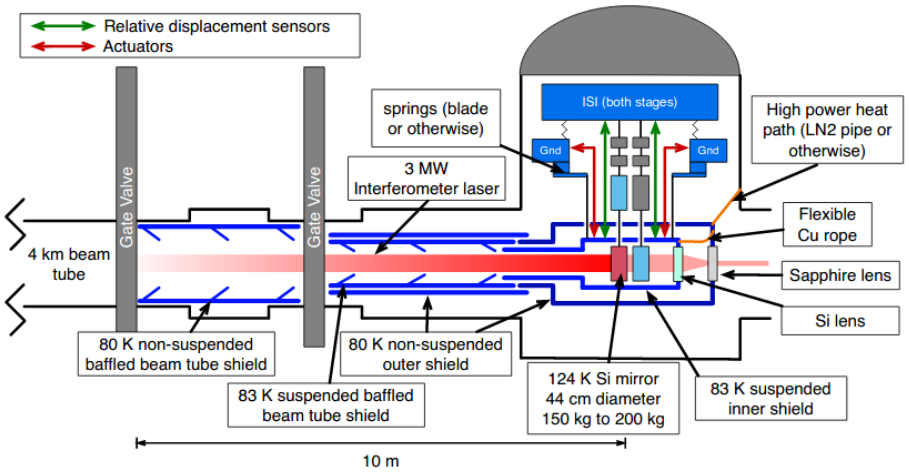

Configuration for the LIGO Voyager test masses (End Test Mass). We highlight the shields surrounding the suspended test mass.

SOURCE: Adhikari et al. (2020).

to the square of material's thermal expansion coefficient α, temperature T, and thermal conductivity κ (ROWAN, 2019):

$$S_{TE}(f) \propto \kappa \alpha^2 T^2 \tag{3.2}$$

One can note that, low temperature can minimize thermoelastic noise. It is also possible to use a material with zero thermal expansion coefficient. For Si, the coefficient α crosses zero at a temperature of 123 K (KIM et al., 2016). Therefore, maintaining the temperature of the Si test mass at 123 K reduces thermoelastic noise (in the substrate), as shown in Figure 3.7. In other words, thermal noise will not be dominant in LIGO Voyager.

LIGO Voyager will require high-purity Si test masses (ADHIKARI et al., 2020). Impurities can raise noise curve due to charge carriers which can absorb photons from the high-power laser, heating-up the test mass. This excess of heat must not surpass a critical level, or it will not be possible to maintain the mirror's temperature at 123 K.

The detector's laser wavelength will also change, as Si absorbs light at 1064 nm and will have an initial power of $\sim$ 150 W. Studies are still ongoing to select an

Figure 3.6 - Noise budget for LIGO Voyager.

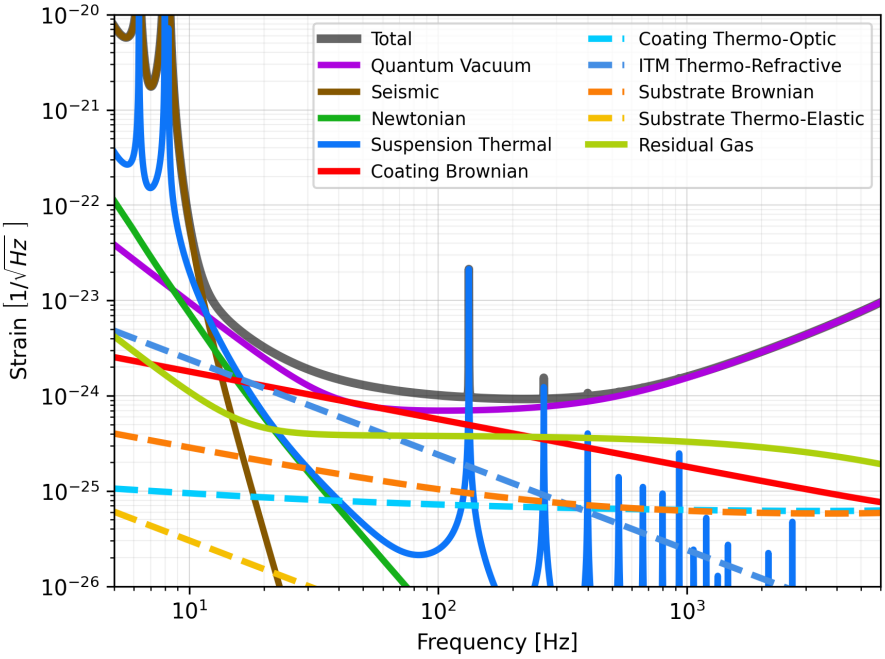

Design noise budget for LIGO Voyager. At low frequencies $f < 10$ Hz, the dominant noise are seismic, suspension thermal, and Newtonian noise. Quantum noise is is dominant for most of the observable frequency band, followed by Brownian noise and residual gas noise. There is a significant improvement compared to Figure 3.2.

SOURCE: Rollins et al. (2020).

appropriate wavelength for the Voyager laser. This choice depends on the properties of Si, the quantum efficiency of the photodiodes, and also the availability of high-frequency lasers with minimal frequency variation (MANSELL, 2018). However, a wavelength range of $\lambda \sim 1500 - 2100$ nm is considered, tending to chose the higher λ value (ADHIKARI et al., 2020). Some studies, as Effler et al. (2023), indicates 2000 nm wavelength.

Constructing LIGO Voyager is a challenge, especially because it involves a cryogenic detector. Many current cryocoolers can introduce significant noise into the system. Further works will design the best alternatives to create an effective cooling system able of cooling the test masses and maintaining their temperature at 123 K while being as noiseless as possible.

The Gravitational Waves Group of INPE (GWINPE), in LIGO collaboration, proposed the use of liquid Nitrogen in pipes that are in contact with the external shields.

Figure 3.7 - Brownian noise of the LIGO Voyager test masses.

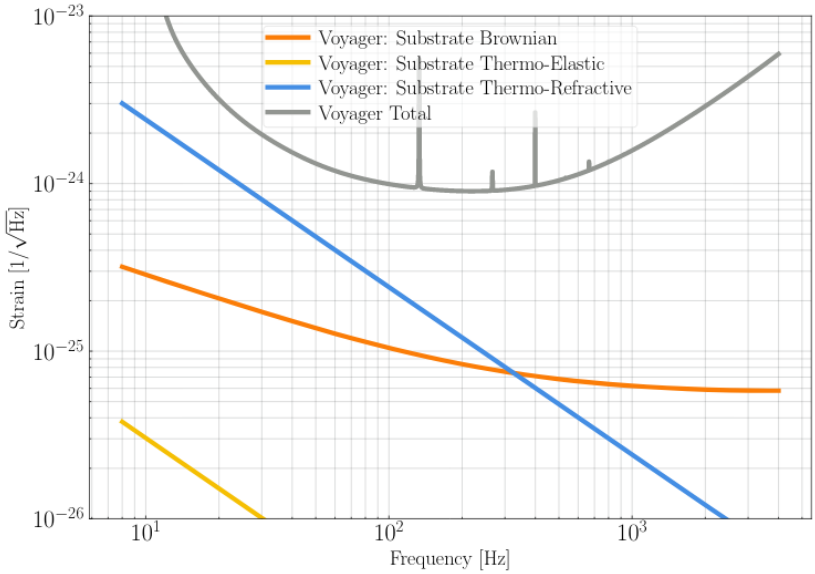

In blue, the refraction noise of the substrate; in yellow, the thermoelastic noise; and in orange, the Brownian noise of the substrate. It can be seen that the last two ones are not limiting the sensitivity for LIGO Voyager, whose total noise curve is represented by the gray line.

SOURCE: Adhikari et al. (2020).

Therefore, test masses can be cooled-down by radiation (LIGO SCIENTIFIC COLLABORATION, 2021). Research in this area is necessary to design and develop this cooling system, also contributing for future cryogenic detectors. The mechanism responsible to generate the liquid Nitrogen flux will introduce Newtonian noise. This subject is also in need of investigations, which will shed light on better design choices.

Another key point for LIGO Voyager is maintaining the temperature at 123 K, which requires removing about 6.3 W from the test masses (ADHIKARI et al., 2020). It remains uncertain if Voyager test mass emissivity will be enough to emit this power through radiation, or if there will be need to coat the mirrors with a high-emissivity paint. This last method, however, will introduce more noise.

Considering the heat extraction mechanisms, the cooling time, the configuration of the system that maintains the temperature at 123 K, and the noise that this system could introduce into the detector are essential aspects for LIGO Voyager and, therefore, for future Gravitational Wave detectors.

3.4 Next generation of gravitational wave observatories

Current generation of detectors, which includes Advanced LIGO (in USA), Virgo (in Italy), and KAGRA (in Japan) form a network of detectors and have made remarkable discoveries. However, they are limited in sensitivity. In order to overcome these limitations, there are proposals for the next generation of gravitational wave observatories. We highlight two of them: Einstein Telescope (ET) and the Cosmic Explorer (CE).

3.4.1 Cosmic Explorer

Cosmic Explorer (CE) is also a dual-recycled Fabry–Pérot Michelson Interferometer, just as Advanced LIGO or Voyager, but with longer arm lengths and new technologies. There will be two observatories in the United States, widely separated and with non-parallel facilities. Until the writing of this thesis, from the available sites, one of them is able to support a 20 km detector, while the other one can support a 40 km arm detector (SHOEMAKER et al., 2022). It is also possible to construct two 40 km interferometers (REITZE et al., 2019).

The longest CE is designed to lower the current LIGO sensitivity curve in a factor of 10. The primary observational science goal is to access most neutron star[2] and black hole mergers in the universe, contributing to multimessenger astronomy (HALL, 2022). The 20 km detector is optimized for neutron star post merger signals. Due to its arm length, the sensitivity is optimized from $1 - 3$ kHz.

It is planned two stages for CE (EFFLER et al., 2023). The first one, targeting operations in the late 2030s, will extend and use technologies developed for A+. The second stage, starting operations in the mid-2040s, improves on the stage 1 sensitivity with new technologies to reduce the quantum and thermal noises of the detector (REITZE et al., 2019). In this upgrade, Thermal noise will be reduced using cryogenics and new materials for test masses and coatings (EVANS et al., 2021).

Many studies, as Effler et al. (2023), proposes that a promising route to maximize CE sensitivity is employing silicon test masses operating at 123 K, with 1.5 or 2 μm laser. The test masses would have 80 cm diameter and 320 kg, which also reduces quantum radiation pressure noise (EVANS et al., 2021).

In addition, as mentioned in Section3.3, silicon has specific characteristics at 123 K,

[2]Stellar to intermediate mass

Figure 3.8 - Sensitivity curves for CE and ET.

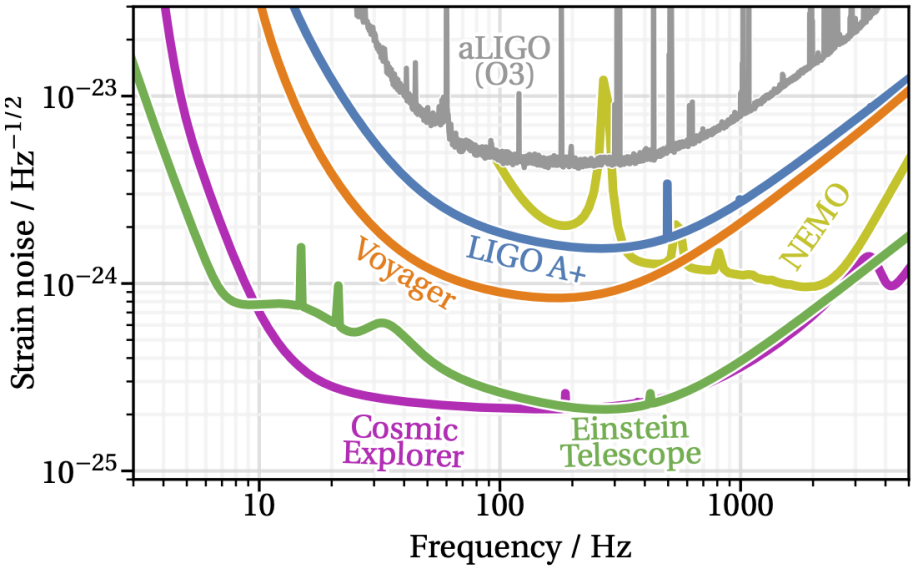

Amplitude spectrum for sensitivity as a function of frequency for Cosmic Explorer (CE), the current aLIGO (O3), LIGO Voyager, and the Einstein Telescope. Also shows other curves, as A+ and NEMO.

SOURCE: Evans et al. (2021).

as low Brownian noise and its coefficient of thermal expansion crosses zero, which vanishes the thermoelastic noise. Also, this temperature is compatible with high optical power (EVANS et al., 2021). Figure 3.8 shows CE sensitivity curve compared to another future detectors and current LIGO designed curve.

This means LIGO Voyager would be a demonstration of technology that could be used to upgrade Cosmic Explorer (EVANS et al., 2021), providing important information for future cryogenic detectors.

3.4.2 Einstein Telescope

Einstein Telescope (ET) is an European gravitational wave detector proposal, also involving a dual-recycled Fabry-Perót Michelson Interferometer. However, in order to be around ten times more sensitive than the current detectors design, ET is based in some basic aspects. First of all, it will be composed by three detectors in a equilateral triangular shape, each arm with 10 km long (ETC, 2024). They will be arranged as shown in Figure 3.9.

In addition, ET will work as a xylophone. It means that each one of the three part of

Figure 3.9 - ET interferometers arrangement.

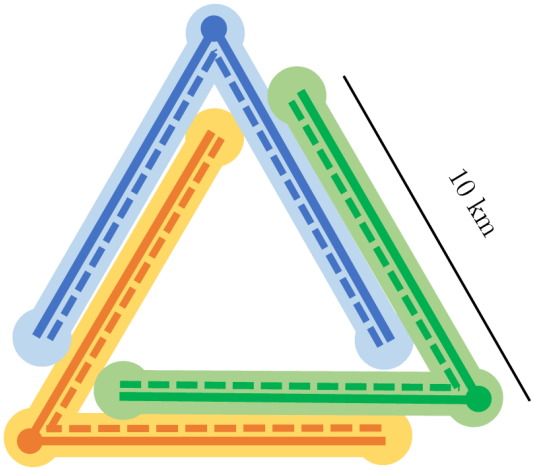

Einstein Telescope interferometers concept configuration. There are three interferometers forming two sides of a equilateral triangle. They will be arranged as shown. ET-LF is represented by continuous line and ET-HF by a dashed line.

SOURCE: Adapted from ETC (2024).

the detector will be, actually, two independent interferometer (ETC, 2020). One will work at room temperature with peak sensitivity at high frequencies. This is the high power detector (ET-HF). The other one, called low-power detector (ET-LF), will work at very low temperatures ($10 - 20$ K), optimized to the low frequency band. In Figure 3.9, ET-LF is represented by continuous line and ET-HF by a dashed line.

The reason of using two different interferometers is to separate the issues related to the use of high power laser, as thermal and radiation pressure, from those related to achieving low-frequency sensitivity, as Brownian noise (ETC, 2020). Therefore, it will be possible to combine both sensitivity curves, one from ET-LF and the other from ET-HF, during the observing runs.

The ET-LF will have silicon-made test masses of 200 kg, cooled-down to $10 - 20$ K in order to reduce thermal noise (ETC, 2024). The silicon mirror will be suspended from the system by silicon fibers. It will be cooled in a dedicated cryostat, which will include two radiation shields at 8 K and 80 K. In addition, absorbed heat from laser light by the test masses or thermal radiation will be extracted by conduction through the suspension fibers (ETC, 2020).

Also, in order to reduce seismic and gravity gradient noise impacts on sensitivity induced by seismic waves and air compression waves, ET will operate under-

ground (AMANN et al., 2020). Consequently, it will be possible to extend down the detection frequency band to a few Hz (ETC, 2024). Figure 3.8 shows sensitivity curve for ET, comparing it to Advanced LIGO during O3, LIGO Voyager, and Cosmic Explorer.

3.5 Chapter summary

This chapter was dedicated to discussing ground-based gravitational wave detectors, their basic design and their working principles using interferometry. Furthermore, we discussed ground-based detector's design sensitivity curve and their noise budget taking aLIGO as example. The main noise sources are: thermal noise, quantum noise, seismic noise, Newtonian noise, and others. After that, we described LIGO Voyager project, whose design involves cryogenics and Si made test masses. It have many advantages, as suppressing thermoelastic noise, since test masses temperature are maintained at 123 K. This detector design served as the motivation for the present work. Finally, future ground-based gravitational wave detectors that will also use cryogenic temperatures and silicon test masses were discussed. These detectors will also benefit from the present work.

In the next chapter, we will briefly discuss heat transfer theory, describe the Si emissivity experiment, the used methodology, and data treatment.

4 EXPERIMENTS ON SILICON EMISSIVITY

This chapter is dedicated to the experiments on silicon effective emissivity. Therefore, we briefly discuss heat transfer theory and define some fundamental equations while discussing the experiment.

4.1 Heat transfer theory

According to the laws of Thermodynamics, heat will naturally flow from a body at temperature T_1 to another at temperature T_2 in an isolated system, as long as $T_1 > T_2$. As this process continues, the temperature gradient between the two bodies decreases until both reach thermal equilibrium. In addition, there are three different heat transfer mechanisms: conduction, convection, and radiation.

4.1.1 Conduction

In general, conduction occurs in the interior of a body, since it has a gradient of temperature inside of it, or when in contact with another body at different temperature (CENGEL, 2003). The rate of heat conduction per unit of area q_{cond} (W/m^2) through a medium depends on the geometry of the medium, the material, and the temperature gradient across the medium. The one-directional form for the conduction can be written as:

$$q_{\text{cond}} = -\kappa \frac{dT}{dx}, \tag{4.1}$$

where κ ($W/m \cdot K$) is the thermal conductivity and dT/dx (K/m) is the temperature gradient along the x-direction. A three-dimensional form can be written as following:

$$q_{\text{cond}} = -\kappa \nabla T, \tag{4.2}$$

where ∇T (K/m) is the temperature gradient. The thermal conductivity factor, in general, also deppends on position and temperature (LIENHARD V; LIENHARD IV, 2024). It is also important to note heat is conducted in direction of the decreasing temperature, this is represented by the negative sign in Equations 4.1 and 4.2.

4.1.2 Convection

This mechanism of heat transfer depends on mass movements from one region to another. This is a intricate process that involves turbulence and fluid motion. Experimentally, it is possible to conclude that the convection heat transfer rate depends on the surface area of the source and the fluid viscosity, which have influence in the mass movements (CENGEL, 2003). Despite being a complex mechanism, the rate

of convection heat transfer by unit of area q_{conv} (W/m^2) can be expressed by the usually called Newton's law of cooling:

$$q_{\text{conv}} = h(T_{\text{s}} - T_{\infty}), \tag{4.3}$$

where T_{s} is the heat source surface temperature, T_{∞} is the fluid temperature sufficiently far from the surface, and h is the convection heat transfer coefficient (W/m^2). However, this coefficient can depend on the temperature difference $T_{\text{s}} - T_{\infty}$.

4.1.3 Radiation

Radiation is the heat transfer by electromagnetic waves emitted by a body at temperature T. The intensity of the energy flux depends on the temperature of the body and its surface area. Since it is a emission of light, no medium is required for radiative transfer. However, the surfaces should be in visual contact for direct radiation transfer (SIEGEL, 2001). We discuss this process in more details since it is important to our experiment to measure Silicon emissivity.

The emissive power per unit of area emitted by a body is represented by $e\,(T)$ (W/m^2). This flux at any wavelength is called the monochromatic emissive power, $e_{\lambda}\,(\lambda,\ T)$. Therefore, the total power per unit of area emitted by this body is the integral of the monochromatic emissive power over all wavelengths:

$$e\,(T) \equiv \int_0^{\infty} e_{\lambda}\,(\lambda, T)\ d\lambda. \tag{4.4}$$

For a black body radiation, this is given by Stefan-Boltzmann law for black body emmition:

$$e_{\text{b}}(T) = \sigma T^4 \tag{4.5}$$

where σ is the Stefan-Boltzmann constant, units $\text{W/m}^2\cdot\text{K}^4$, and T is the black body's temperature. On the other hand, the black body radiation spectrum is described by Plank's law:

$$B_{\lambda}(\lambda, T) = \frac{2hc^2}{\lambda^5} \cdot \frac{1}{e^{hc/\lambda k_{\text{B}} T} - 1}, \tag{4.6}$$

where c is the speed of light in vacuum, h is Planck's constant, and k_{B} is the Boltzmann's constant.

However, most real objects does not emit like a black body. At the same temperature, a non black body radiates less energy than the ideal case. It is possible to express

the non black body radiation as:

$$e_{\mathrm{b}}(T) = \epsilon \sigma T^4 \tag{4.7}$$

where ϵ is the emissivity of the surface. Therefore, a black body has $\epsilon = 1$.

This is valid for an opaque body which radiates energy by electromagnetic waves. However, if the body is semitransparent to the emitted radiation, using a surface area would result in an effective emissivity. In this sense, a more accurate approach for semitransparent bodies would consider that emissivity as a bulk phenomenon, since photons could scape from inside the body, not only from its surface.

Another important equation for our experiment refers to the radiation emitted by an object enclosed within a shell. Consider a body of emissivity $\epsilon\,(T)$ and a surface area A at a temperature T. It is completely enclosed by another surface, named shield, with surface area A_{Sh}, at a temperature T_{Sh}, and an emissivity $\epsilon_{\mathrm{Sh}}\,(T_{\mathrm{Sh}})$. Then the net energy transfer by radiation from the inner body to the shield can be calculated by (SIEGEL, 2001):

$$Q_{\mathrm{rad}} = \frac{\sigma A\,(T^4 - T_{\mathrm{Sh}}^4)}{1/\epsilon\,(T) + (A/A_{\mathrm{Sh}})\,[1/\epsilon_{\mathrm{Sh}}\,(T_{\mathrm{Sh}}) - 1]} \tag{4.8}$$

In the following sections, we will discuss the cooling-down system proposal in the LIGO Voyager context and the experiment arrangement while considering the heat transfer process to measure Si emissivity (ϵ_{Si}).

4.2 Cooling-down and temperature maintenance proposal

Here we explain our cooling-down proposal. Let us consider the end test mass (ETM) chamber configuration for LIGO Voyager (LIGO SCIENTIFIC COLLABORATION, 2021). Figure 4.1 shows LIGO Voyager ETM chamber layout, where we highlight an important fact: the test mass is placed inside an isolated inner shield, which is at ≈ 80 K. This, in turn, is placed inside another shield at ≈ 200 K.

The main goal is to cool-down the test mass radiatively with a two layer heat shield system, avoiding thermal links connected on the test mass. The inner shield may require vibration isolation in order to mitigate scattered light noise. The outer shield is cooled with a high power thermal link while the inner is cooled by a pipeline with nitrogen flux.

This cooling method, which have contributions from GWINPE, is developed based

Figure 4.1 - LIGO Voyager ETM chamber layout.

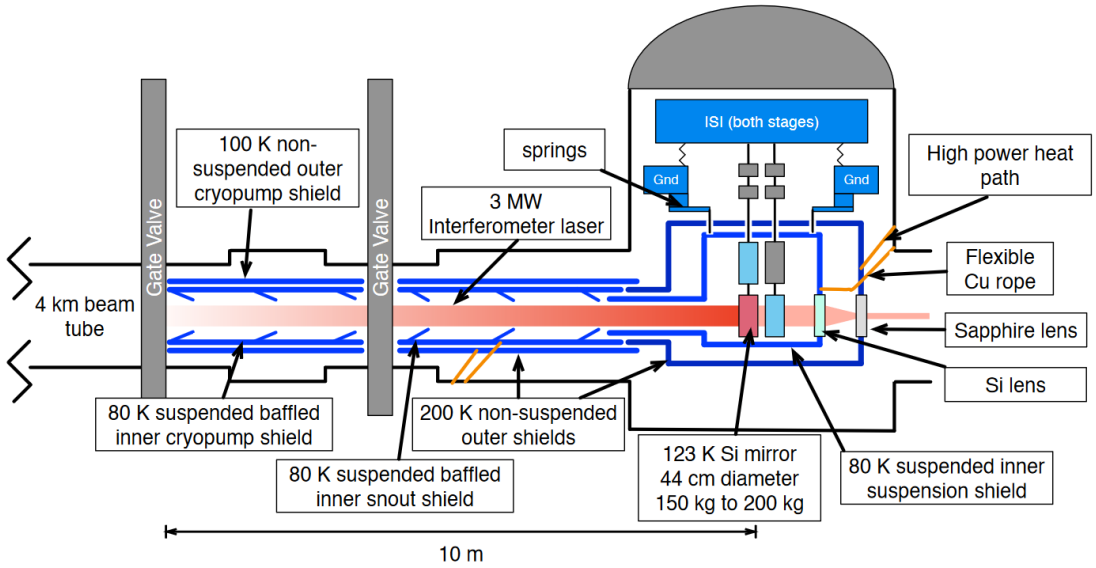

Layout of the ETM chamber configuration with the cryogenic cooling elements. SOURCE: LIGO SCIENTIFIC COLLABORATION (2021).

on reducing thermal noise using sub-cooled liquid nitrogen with a system capable of cooling the test masses by radiation, and the shields by conduction. The liquid nitrogen will flow in a pipeline connected to a copper link placed inside the non-suspended outer vacuum chamber. In addition, this pipeline will be connected directly to the 80 K chamber (suspended inner shield), in an especial connection thermally isolated from the room temperature vacuum chamber.

The nitrogen flux will be generated by magnetic impellers inside the pipeline (this will be discussed in Chapter 9). Furthermore, with this configuration, it is possible to cool-down the test mass by radiation **if Si emissivity is high enough**.

4.3 Experiment setup

As previously mentioned, in addition to the low-temperature regime, silicon-made test masses will be used for LIGO Voyager (LIGO SCIENTIFIC COLLABORATION, 2021) and for Cosmic Explorer (ETC, 2024). Since the idea is to cool-down the test mass by radiation, it is important to conduct experiments dedicated to measure Si emissivity as a function of temperature. Constancio et al. (2020) started the work in this direction, and the present thesis will extend, revise their results, and add

contributions to it.

In addition, to know Si emissivity at cryogenic temperatures is crucial, since it will indicate if the mentioned detector's mirrors are able to cool-down and maintain its temperature at 123 K during the observational runs.

A diagram of the experiment setup is shown in Figure 4.2. We start with a dewar measuring 27 cm in diameter and 30 cm in heigth. Connected to this dewar, there are some tubes to pass thermocouples wires. The Si piece, represented by a blue rectangle, is suspended by thin wires, and the dewar is submerged in NL2. Thermocouples positions are marked by stars.

Since it is aimed to measure the energy dissipated only by radiation, we should reduce all other forms or heat dissipation as much as possible. Therefore, it is necessary to use a cryostat in a high vacuum regime to suppress convection and conduction by air. Ideally, the pressure should be equal or less than 10^{-7} mbar. However, during the experiments we reached a pressure in the order of 10^{-5} and 10^{-6} mbar, sufficient enough to suppress convection and gas conduction inside the dewar. Furthermore, the container also has a long top module with baffles to avoid ambient infrared radiation influence (see Figure 4.3).

For each run, the specimen was suspended by titanium-aluminum-vanadium (Ti90Al6V4) wires, of $\approx$ 20 cm long and diameter of 0.29 mm, to suppress thermal conduction. In addition, the thermocouples used to read the specimen and the shield temperatures were produced using thin wires (0.0799 mm of diameter) also to minimize thermal conduction.

Once tested for vacuum leakages, a cryogenic environment is created around the dewar (also called shield) diving it in a liquid nitrogen (LN2) bath, at $\approx$ 77 K. This can be seen in Figure 4.3 part a. The amount of LN2 was enough to cool the dewar and cover it completely throughout the run. Figure 4.3 (part b) shows the end of a experiment run, when the dewar was removed from LN2.

Therefore, our setup aimed to minimize all other heat transfer forms but radiation, creating a environment to measure the specimen emissivity in function of temperature.

Let us consider a pure Si test mass dissipating heat by radiation only. The energy transfer is given by Equation 4.8. The dewar's interior was painted with a special high emissivity and low outgassing black polyurethane paint - PU1 ($\epsilon_{\mathrm{PU1}} = 0.89$).

Figure 4.2 - Si emissivity experiment.

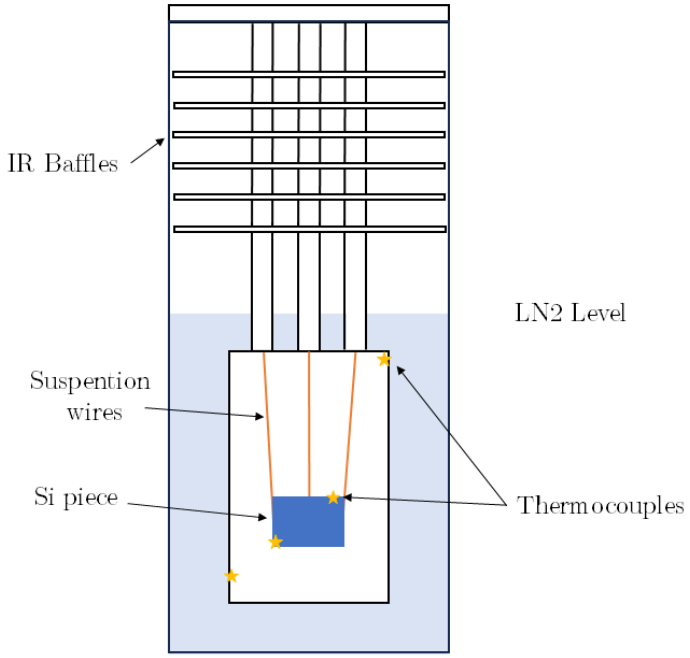

Schematic view of the experiment. The Si piece, which can be irregular, is represented by a blue rectange suspended by thin wires. Termocouples positions are marked by yellow stars. The dewar is submerged into liquid nitrogen (NL2).

SOURCE: From the authors.

We used Equation 4.8 to calculate the Si effective emissivity $\epsilon(T)$ by:

$$\epsilon(T) = \frac{1}{\frac{A_{\mathrm{Si}}\sigma\left(T^4 - T_{\mathrm{sh}}^4\right)}{m_{\mathrm{Si}}C_{\mathrm{p}}(T)\frac{dT}{dt}} - \frac{A_{\mathrm{Si}}}{A_{\mathrm{Sh}}}\left(\frac{1}{\epsilon_{\mathrm{Sh}}} - 1\right)}, \tag{4.9}$$

where $\epsilon(T)$ is the total emissivity as a function of temperature, C_{p} is the specific heat capacity of Si (ANDERSON, 1930), σ is the Stefan-Boltzmann constant, m_{Si} is the mass of the Si piece, A_{Si} is its area, ϵ_{Sh} is the shield emissivity, A_{Sh} is its (inner) surface area, and T_{sh} its the temperature. By "shield" we mean the container holding the specimen, as described in the experiment arrangement section.

As expected, for the case that $A_{\mathrm{Sh}} \gg A_{\mathrm{Si}}$ or $\epsilon_{\mathrm{Sh}} = 1$, Equation 4.9 is simplified to:

Figure 4.3 - The beginning and the end of an experiment run.

Figure a. shows the experiment run in its beginning, while diving in the dewar in the liquid nitrogen bath. Figure b. shows the dewar completely out the LN2, when the run was over.

SOURCE: From the authors.

$$\epsilon_0\left(T\right) = \frac{m_{\mathrm{Si}} C_{\mathrm{p}}\left(T\right) \frac{dT}{dt}}{A_{\mathrm{Si}} \sigma \left(T^4 - T_{\mathrm{sh}}^4\right)} \,, \tag{4.10}$$

and for the analyzed data, the deviation of ϵ from ϵ_0 is in order of 10^{-2}.

In summary, by this experiment, temperature time series was collected to obtain dT/dt and estimate the emissivity of silicon as a function of temperature according to Equation 4.9. All experiment runs were conducted at the Gravitational Waves Laboratory of the National Institute for Space Research (INPE), São José dos Campos, São Paulo State, Brazil.

4.4 Data analysis

Once the dewar is dived in the LN2, we collected temperature data by thermocouples. Analyzing the cooling-down curve, we can calculate the temperature derivative and, with the temperature information, Equation 4.9 results in the emissivity.

It was used five thermocouples: one to measure room temperature at the facility; two to monitor the specimen temperature in two opposite sides; and two to monitor the dewar (acting as the shield) temperature on its top and bottom parts. The

temperature channels were disposed as diametrically as possible. They were fixed to the test masses with small pieces of kapton tape. Their wires accessed the dewars interior passing through the center pipe fixed at the dewar's lid. One can note the mentioned pipes in Figure 4.3. They have their own IR baffles to avoid infrared radiation contamination from the environment.

Emissivity calculations using Equation 4.9 requires shield and specimen temperature, as the specimen temperature derivative as well. Since there are two thermocouples for each, specimen and shield, it was used the mean temperature from the two channels.

However, the thermocouples used in this experiment uses a digital system to read temperature. Reading variations due to low precision, including data noise, introduces short-term fluctuations that propagate through derivative calculations. This is what this work means when referring data as "noisy". Likewise, external disturbances, such as ambient temperature variations, also contributes to readings oscillations.

It means that data have a characteristic noise which can affect dT/dt calculations. The solution found was to smooth data in several different approaches and compare the results, as follows.

4.4.1 Numerical differentiation by finite difference

One first and simple manner to calculate the temperature derivative curve was a applying the numerical differentiation by finite difference approximation. In order to overcome fluctuations in the data, the numerical derivative was calculating considering the $(i-n)$th position before a data point, and the $(i+n)$th one after. In other words, for a given temperature T_i, we approximated the derivative by:

$$\frac{dT}{dt} \approx \frac{\Delta T}{\Delta t} = \frac{T_{\text{i-n}} - T_{\text{i+n}}}{t_{\text{i+n}} - t_{\text{i-n}}} \tag{4.11}$$

Since it still presented large oscillations, a second approach arose by smoothing temperature data using a moving average before calculating the derivative estimation. It means that it calculates the mean for a collection of derivative data points around the i-th one, from the $(i-k)$th to the $(i+k)$th. We also refer to it as a "smoothing filter".

4.4.2 Curve fitting

A third approach was by fitting function curves to temperature data. Given the nature of the cooling-down process, we used an exponential curve to fit data:

$$T(t) = a_0 \cdot e^{-a_1 \cdot t} + b_0 \cdot e^{-b_1 \cdot t} + c_0 \tag{4.12}$$

where a_0, a_1, b_0, b_1, and c_0 are constants. Then, one can use the fitted constants to plot the temperature derivative:

$$\frac{dT}{dt} = -a_0 a_1 \cdot e^{-a_1 \cdot t} - b_0 b_1 \cdot e^{-b_1 \cdot t} \tag{4.13}$$

As a forth approach, it was also considered a high-order polynomial function to temperature data, as the polynomial derivatives are easily calculated. It was used an 10th-degree polynomial function:

$$\sum_{n=0}^{10} a_n \cdot x^n \tag{4.14}$$

where a_n are the coefficients, then its first derivative is given by:

$$\sum_{n=1}^{10} n \cdot a_n \cdot x^{n-1} \tag{4.15}$$

4.4.3 Savitzky-Golay filter

Finally, the Savitzky-Golay (SavGol) filter was used. This is a smoothing technique useful to filter digital data, enhancing data quality while preserving essential features such as peaks.

For a given data of N points and a window length w, it calculates a polynomial fit of order p_{order} in each data subset while moving the filter along the data. Python has a SavGol function (FOUNDATION, 2024), with data, w, and p_{order} as input.

4.5 Experiment limitations

Before discussing the experiment results, we highlight some expected limitations given the experiment design.

The first one relies on the assumption of uniform temperature distribution across the silicon specimen. This is the ideal case. During the experiments, as one can note in Chapter 5, the channels dedicated to follow the Si piece temperature will have different values, depending on where they are positioned on it.

The emissivity calculations rely on temperature readings from thermocouples. However, for a irregular shape and varying surface properties of the specimen, like the presence of spalls or the different distances from the specimen to the dewar's wall, can generate a temperature gradient inside the piece while cooling. Furthermore, uneven exposure to the dewar environment can also lead to different cooling rates for different regions of the specimen. Therefore, the measured temperature may not represent the actual surface temperature of the entire specimen. This effect can be present also in regular shape specimens, such as the cylindrical one.

This divergence in temperatures introduces errors in the calculation of heat transfer and, consequently, the derived emissivity values. In addition, low temperature precision from data acquisition impacts directly the emissivity estimation. These estimations can be improved using more precise temperature data.

Nevertheless, it is important to make sure the thermocouples used to monitor temperature are well fixed and calibrated. Evidently, the experimental setup and further calculations assumes that the thermocouples provide precise temperature readings. However, digital noise and low precision in thermocouple readings introduce random fluctuations that propagate through the differentiation, increasing uncertainty in the emissivity values. This effect will be noted later on the next two chapters.

For the next experiment runs, using multiple redundant thermocouples at different points on the specimen, taking an average to minimize local variations, can reduce the effect of the mentioned issues.

It is also relevant to consider that we assumed ideal radiative heat transfer conditions within the dewar. By reasons explained in the next chapter, the dewar's interior was coated with a high emissivity black ink (PU1), presumed to have a constant emissivity of $\epsilon_{\mathrm{PU1}} = 0.89$ for the temperature range of this experiment.

4.6 Chapter summary

This chapter discussed theoretical foundations and the experimental setup for measuring the silicon (Si) emissivity. First, we discussed heat transfer principles, important equations, and how to prepare the experiment mitigating all heat transfer mechanisms but radiation. The experimental setup involved a cryogenic environment created by a dewar submerged in liquid nitrogen, with silicon specimens suspended by thin wires to minimize heat conduction. The dewar interior was coated with high-emissivity paint to approximate blackbody conditions, while a vacuum regime suppressed convection and conduction by air. Temperature data were collected using thermocouples. Emissivity was calculated based on temperature derivatives over time. Finally, we discussed how to address noise in the data and experiment limitations.

5 SILICON EMISSIVITY EXPERIMENT RUN USING THE STANFORD SPECIMEN

This chapter describes the experiment runs for Silicon emissivity using a cylindrical Si piece gently lent by the Stanford group. Three consecutive runs were conducted with this specimen.

5.1 The Silicon specimen

With 1.034 kg, 15.24 cm in diameter, and 2.45 cm thick, the specimen has a milled edge and a mirror coating on one side. Its surface area is approximately 482.13 cm^2. A picture of the specimen used can be seen in Figure 5.1

Figure 5.1 - Silicon piece lent by Stanford Group.

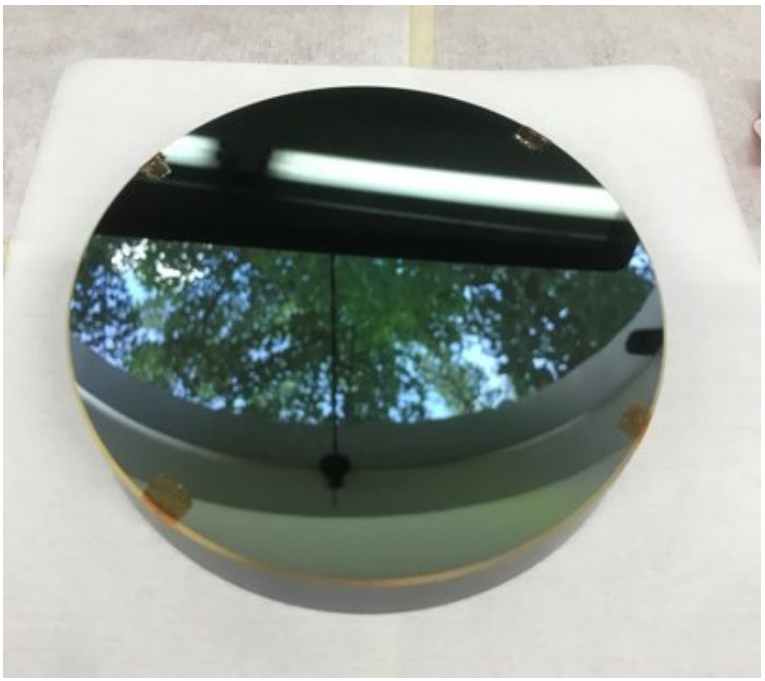

Stanford piece used in this experiment run. This picture shows the coated side.
SOURCE: From the authors.

As discussed previously, the sample is suspended by titanium-aluminum-vanadium (Ti90Al6V4) wires. Four lines were used, each with a 0.29 mm diameter and $\approx$ 20 cm long. Figure 6.3 shows the suspended specimen before enclosing it inside the dewar.

In order to measure the temperature, it was used AWG-40 thermocouple wires made of constantan and copper, with 0.0799 mm of diameter. They were used as channels

Figure 5.2 - Silicon piece suspended by thin wires.

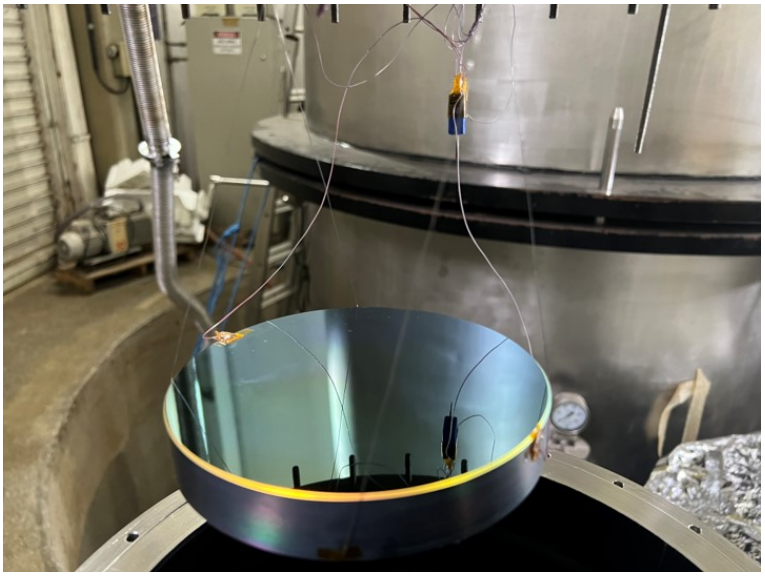

Silicon piece used in this experiment run suspended before the experiment begins.
SOURCE: From the authors.

to follow-up the specimen's and dewar's interior's temperature.

5.2 Issues during the experiment

During the first time the experiment was conducted, the specimen was enclosed by a Aluminum dewar. The top part, called "lid", was also made of Aluminum. However, the pipes through the thermocouples' wires can reach the specimen were made of stainless steal. Therefore, it was not possible to solder both parts directly. In order to bind both parts, it was used an epoxy glue (EP21TCHT-1).

All connections were tested before the run began, and the team did not notice any vacuum leakage greater than 10^{-10} mbar $\cdot$ l/s. Nevertheless, when the Aluminum dewar was immersed in liquid Nitrogen, the pressure increased to $1.7 \cdot 10^{-1}$ mbar. Once rechecking for leaks, it was found that the epoxy connections broke due to the thermal shock. The leakage was in the order of 10^{-6} mbar $\cdot$ l/s.

In order to address this issue, another lid was produced, this time made of stainless steal. Consequently, it was allowed to solder the parts: lid and pipes. This solved the epoxies cracks problem. The dewar was still made of Aluminum, but no leakages were detected.

Figure 5.3 - New dewar used in this experiment.

New dewar used in the emissivity experiment made of stainless steel.
SOURCE: From the authors.

The dewar was dived once again in the liquid Nitrogen and, by the first minutes the pressure dropped, as expected. But another leakage was detected. This time, it was created by the Indium seal, because dewar and lid were made of different materials, the system presented a differential thermal contraction. The indium o-ring was not able to compensate that, breaking and producing a vacuum leakage.

The found solution was producing a new dewar from a commercial stainless steel can. The top part was adapted in order to fit the lid and place the indium seal properly. Figure 5.3 shows the final dewar. With this new one, without detecting leakages or other problems, the data was recorded.

In addition, the interior of the new dewar was completely covered with PU1 paint. This is a black polyurethane paint developed primarily to be used in spacecraft. A PU1 coating provides thermal protection and thermal stability at very low temperatures. It has emissivity of $\epsilon = 0.89$.

Temperature data acquisition started a few minutes before the dewar was immersed

Figure 5.4 - Cooling-down curves for experiment runs using the Stanford piece.

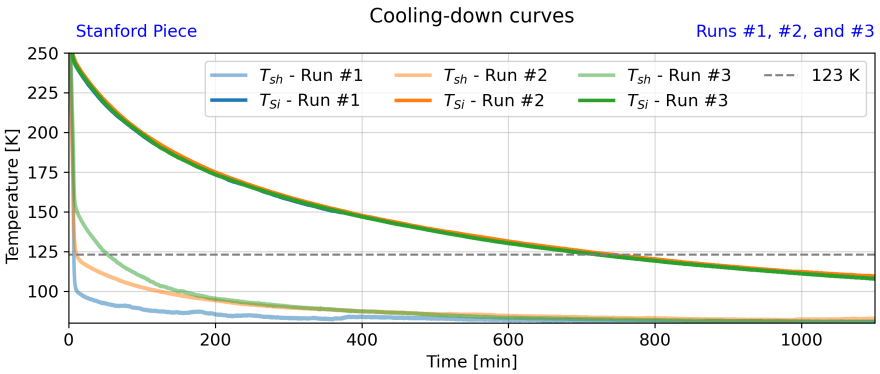

Cooling-down curves for the runs using the Stanford Piece. All runs are separated by different colors: blue for the first run, orange for the second one, and green for the third one. Solid colors stands for the specimen temperature and shaded colors for the shield temperature.

SOURCE: From the authors.

in liquid Nitrogen (LN2). It formed a plateau at room temperature, which was removed from data to avoid errors of data fitting. Cooling-down curve for all three runs using Stanford specimen are shown in Figure 5.4. One can note that in the first minutes of the first and second runs, the shield is already around 100 K. The third run required additional time to reach this temperature, however still hours before the specimen reached 123 K.

5.3 The first run

During the first run, an issue was detected involving temperature data acquisition. As mentioned, we used thermocouples to monitor the temperature, as represented in Figure 4.2. However, one of them, dedicated for the shield, had its polarity inverted for two hours from the start. Therefore, it registered the wrong temperature. The second thermocouple was working normally, allowing us to use its data. This issue was solved for the second and third runs.

Digital acquisition by low precision thermocouples added oscillations in temperature time series. In order to reduce this noise effects, mainly around 123 K, we attempt many methods, as described in Chapter 4: smoothing temperature data and the derivative calculations; using the Savitzky-Golay filter; and fitting data with exponential and polynomial equations. All methods for the first run are summarized on Figure 5.5.

Figure 5.5 - Data for the Stanford piece temperature.

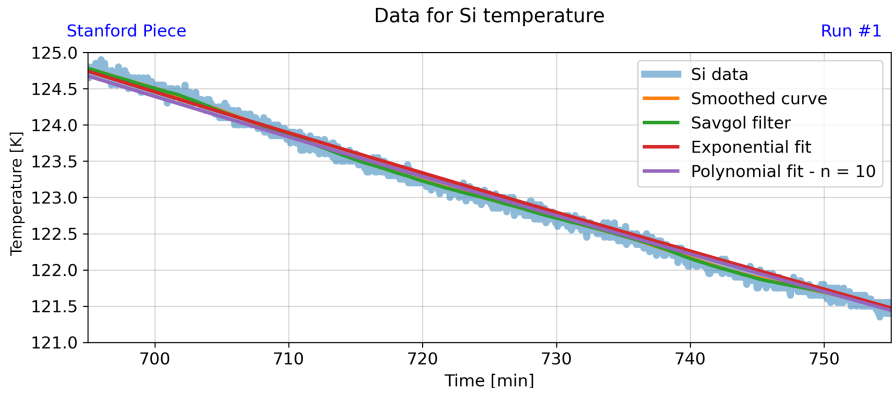

Data for Stanford Si piece temperature. In faded blue, plot shows raw temperature data. In addition, it shows the smoothed data curve, according described in Subsection 4.4.1, data after passing the SavGol filter, and curve fitting with an exponential and a polynomial equation.

SOURCE: From the authors.

First, we smoothed temperature data to estimate the silicon temperature curve derivative, using the method described in 4.4.1. For that, we used $k_1 = 50$. However, as the emissivity result is strongly influenced by these "noise", the calculated derivative was also smoothed using the same parameter.

SavGol filter was also applied in order to reduce temperature data noise. In this work we used the Python SavGol function with window of $w_1 = 201$ and a polynomial order $p_{\text{order, 1}} = 3$. Shield window was $w_1 = 101$. From this reduced data, it was possible to estimate its derivative by numerical differentiation.

In addition, it was fitted an exponential function and a 10-th order polynomial function. Then, the computed coefficients were used to analytically calculate the derivative. The summary of all derivatives are shown in Figure 5.6

Using the reduced specimen and shield temperature data along with the derivative curve, we calculated the specimen emissivity according to Equation 4.9. Figure 5.7 shows the results for the first run using all mentioned approaches.

One can note the large oscillations due to low temperature reading precision, particularly for raw data results in 5.7. These oscillations were reduced by smoothing data passing a simple moving average filter to the derivative curve (in orange). This curve is similar to the SavGol results, in green. In red, the resulted curve for the

Figure 5.6 - Calculated temperature derivative curve for the first run.

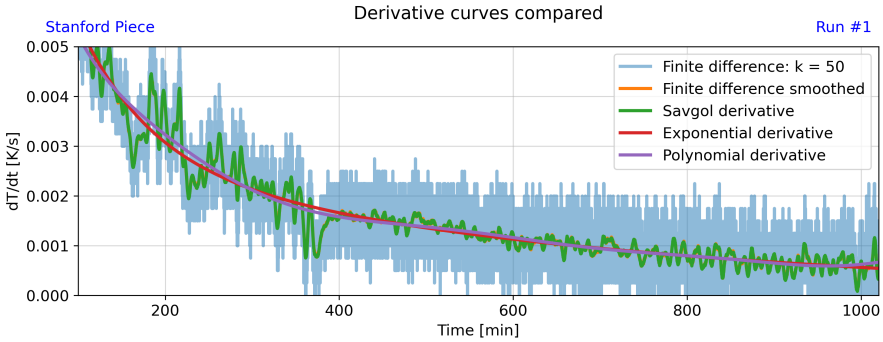

Derivative curves compared for the first run. In faded blue, plot shows numerical differentiation by finite difference, using $k_1 = 50$. Then, in orange, the same result but smoothed. In green, the derivative calculated from SavGol filter. In red, the derivative calculated from the exponential function coefficients, and in purple the result from the polynomial fit.

SOURCE: From the authors.

Table 5.1 - Summary of emissivity values at 123 K for different calculation methods - First run.

Data	Emissivity (ϵ_1)	Error ($\pm\delta\epsilon_1$)
Raw Data - Finite difference	0.622	0.019
Raw data - Smoothed derivative	0.617	0.003
SavGol Filter	0.611	0.003
Exponential fit	0.635	0.002
Polynomial fit	0.631	0.005

SOURCE: From the authors.

exponential fit and in purple the results for the polynomial fit. This last one shows some oscillations in emissivity due to shield temperature fitting, which presented the same behavior.

The main result is the specimen emissivity at 123 K. As all curves still present some data noise, it was needed to estimate the emissivity error around the value at 123 K. For each approach, we summarized the results in Table 5.1.

In Table 5.1, as for the other tables concerning second and third runs, “Raw Data - Finite difference” refers to results obtained by smoothing specimen and shield temperature, but not applying the smoothing filter to the derivative curve. This last

Figure 5.7 - Emissivity for the first run.

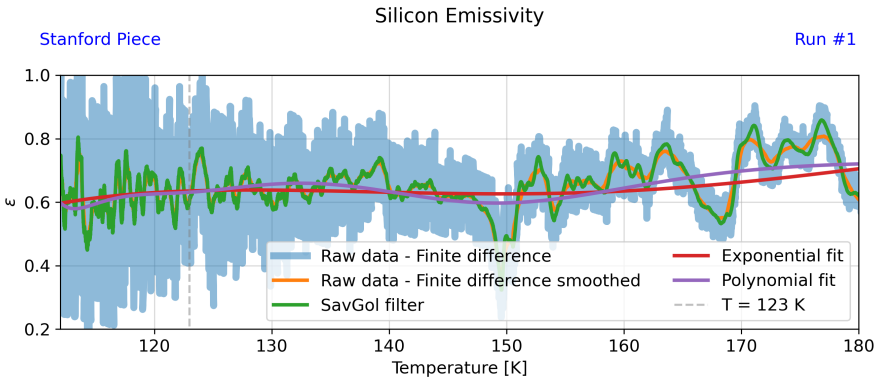

Emissivity results for the first run using the Stanford Si cylindrical piece. In faded blue, results using numerical differentiation by finite difference. In orange, emissivity calculations using the same, but also smoothing the derivative. In green, the results using the SavGol filter. In red and purple, the emissivity using the analytical derivative from exponential and polynomial fitting, respectively.

SOURCE: From the authors.

one is named "Finite difference smoothed" meaning the smoothed derivative. The estimated effective Si emissivity, based on data from the first experiment run, is shown in Figure 5.10.

5.4 The second run

For the second run, the issue involving the temperature data acquisition was solved. Therefore, it was possible to consider a mean value between the two channels dedicated for each important component, i. e., the Si piece and the shield.

As done for first run data, to reduce digital noise effects, it was used a smoothing filter in temperature data and the derivative calculations, as the Savitzky-Golay filter, and fitting methods as well.

The smoothing filter also used $k_2 = 50$ for specimen and shield temperatures. The same was applied to the calculated derivative. SavGol filter parameter was also a window of $w_2 = 201$ and a polynom of order $p_{\text{order, 2}} = 3$. Shield window was $w_2 = 301$. Then, it was possible to estimate its derivative by numerical differentiation. From the computed coefficients from the fitted equations, we analytically calculated the derivative.

The reduced specimen and shield temperature data were used with the derivative

Figure 5.8 - Emissivity for the second run.

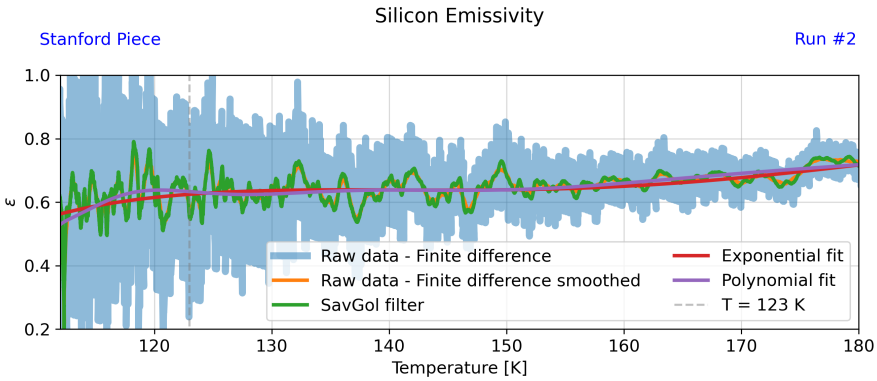

Emissivity results for the second run using the Stanford Si cylindrical piece. In faded blue, results using numerical differentiation by finite difference. Emissivity calculations using smoothed derivatives are in orange. In green, the results using the SavGol filter. Red and purple line shows the emissivity from exponential and polynomial fitting, respectively.

SOURCE: From the authors.

curve to calculate specimen emissivity. Figure 5.8 summarizes the results. One can note that the polynomial fit presents less variations when compared to the first run in 5.7. This is because this run had a better shield temperature fitting, showing less variations around data points. One can note that it is very similar to the result from exponential fitting.

The estimated effective Si emissivity, based on data from the second experiment run, is shown in Figure 5.10.

Table 5.2 - Summary of emissivity values at 123 K for different calculation methods - Second run.

Data	Emissivity (ϵ_2)	Error ($\pm\delta\epsilon_2$)
Raw Data - Finite difference	0.593	0.013
Raw data - Smoothed derivative	0.598	0.003
SavGol Filter	0.596	0.005
Exponential fit	0.625	0.001
Polynomial fit	0.633	0.006

SOURCE: From the authors.

5.5 The third run

Following the previous runs, noise effects were reduced by the same methods. This run used $k_3 = 50$ for temperature smoothing filter. The same parameter was applied to smooth calculated derivative. SavGol filter parameters are $w_3 = 201$ and $p_{\text{order, 3}} = 3$. Then, it was possible to calculate its derivative using the numerical differentiation method or using the fitted equations coefficients.

Finally, we used reduced data with Equation 4.9 to calculate specimen emissivity. Figure 5.9 summarizes the results. Data for the polynomial fit in third run, as in the second one, also shows less variations than in first run.

The specimen emissivity at 123 K, as for the previous runs, was calculated and summarized in Table 5.3. Figure 5.10 shows all results for the three experimental runs, according to the emissivity estimation method. The error bars are also shown, and the mean emissivity result is $\bar{\epsilon} = 0.627 \pm 0.007$.

Table 5.3 - Summary of emissivity values at 123 K for different calculation methods - Third run.

Data	Emissivity (ϵ_3)	Error ($\pm\delta\epsilon_3$)
Raw Data - Finite difference	0.627	0.021
Raw data - Smoothed derivative	0.628	0.002
SavGol Filter	0.639	0.004
Exponential fit	0.642	0.002
Polynomial fit	0.631	0.002

SOURCE: From the authors.

5.6 Chapter summary

This chapter presented the results of the conducted experiment using a cylindrical Si specimen, gently lent by Stanford group. The three experiment runs were described and also the data analysis. The most important result is the Si specimen emissivity at 123 K, calculated by different methods in each run. Figure 5.10 summarizes the results for this experiment. The mean effective emissivity for the Stanford specimen is $\bar{\epsilon} = 0.627 \pm 0.007$.

The following chapter will describe and analyze the second emissivity experiment

Figure 5.9 - Emissivity for the third run.

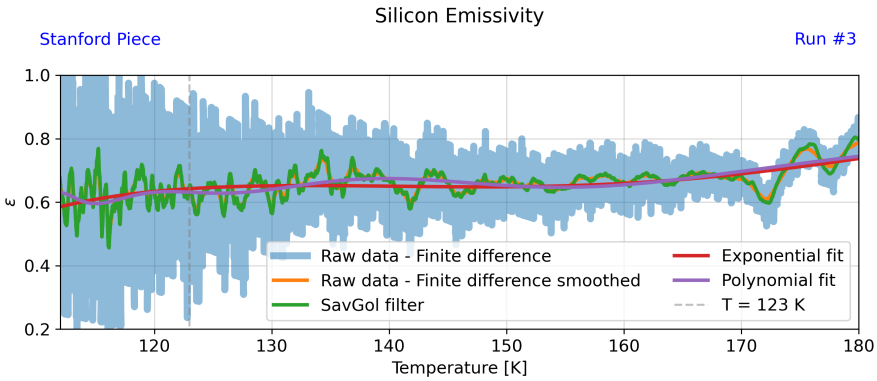

Emissivity results for the third run using the Stanford Si cylindrical piece. In faded blue, results using numerical differentiation by finite difference. In orange, emissivity calculations using the same, but also smoothing the derivative. In green, the results using the SavGol filter. In red and purple, the emissivity using the analytical derivative from exponential and polynomial fitting, respectively.

SOURCE: From the authors.

conducted using an irregular Si piece.

Figure 5.10 - Emissivity estimation methods for Stanford specimen compared.

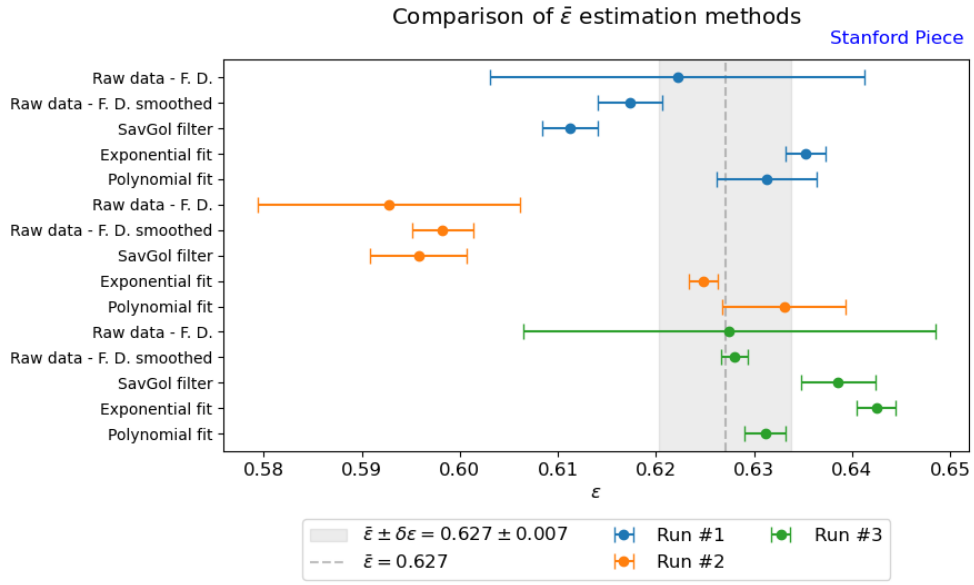

Emissivity results for all experimental runs using the Stanford Si cylindrical piece. In blue, results and error bars for the first run. In orange, estimated emissivity with error bars for the second run. Finally, in green, emissivity calculations and error bars for the third run. Dashed gray line shows the mean emissivity considering all results and the gray region shows the mean value estimated error.

SOURCE: From the authors.

6 SILICON EMISSIVITY EXPERIMENT RUN USING AN IRREGULAR SILICON SPECIMEN

In this chapter, we describe the experiment run for Si emissivity using an irregular shape specimen. Due to an insufficient supply of liquid Nitrogen, the experiment could only be done once. In this way, it was possible to use only one of the two si pieces available.

6.1 The Silicon specimen

The Si specimen has 2.959 kg and purity of 99.5%. Estimating the surface area as best as possible is important, since emissivity is inversely proportional to the surface area (see Equation 4.9). This was a special challenge due to this piece complex shape and rough texture. Three different methods were used to approximate its surface area.

Figure 6.1 - Irregular Silicon piece used in this experiment.

Irregular Si specimen for this experiment run. Its purity is 99.5%.
SOURCE: From the authors.

6.1.1 Estimating the surface area

The first approach involved covering the specimen with tape and summing the total amount required to coat its surface. While this method provided a direct estimation, it is an approximation of the actual surface area, because the tape was not able to fully match up the microscopic irregularities of the specimen. With this method, we estimated the surface area of approximately $A_{\text{Si, 2}} = 739.35$ cm^2.

Figure 6.2 - Irregular Silicon piece scanned vertices plot.

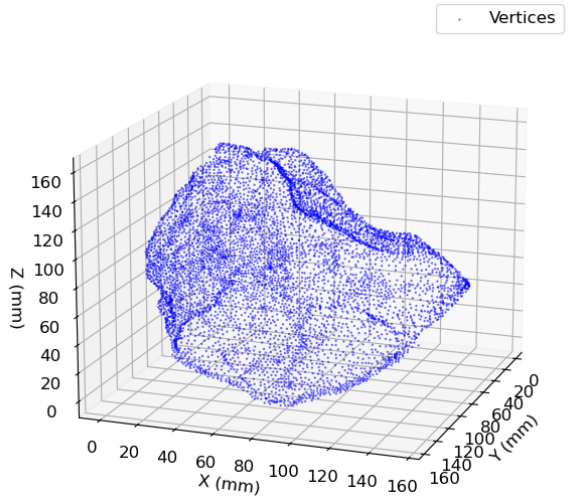

Data points exported from FreeCAD v.021. This dataset was used to calculate a convex hull and model the specimen. However, its irregularities could not be preserved.

SOURCE: From the authors.

The second approach used FreeCAD v0.21 (RIEGEL et al., 2021), an open-source software, to create a 3D scan of the silicon piece and compute its surface area. Figure 6.2 shows the scanned points plotted. One can note that it preserves many of the piece irregularities. For the surface area, the result was $A_{\text{Si, 2}} = 737.62$ cm^2, very close to the first approach using tape. This method provided a more refined measurement than the first one, as it was able to capture finer details.

With the same software, it was possible to export the points coordinates and estimate the surface area by calculating a convex hull, i. e., the smallest convex shape enclosing all scanned surface points, to approximate the area. This technique resulted in the highest estimated value, $A_{\text{Si, 3}} = 763,80$ cm^2.

As one can note, the specimen, showed on Figure 6.1, is very rough. Therefore, the first method already underestimate the surface area, since the tape can not cover all minimum piece irregularities. In comparison, the software was able to scan it with more finesse. Nevertheless, it was not possible to scan the bottom of the piece, and the software considered it flat. This error propagates to the convex hull surface area, since it used the software points to model a convex shape. In addition, the convex hull smooths the surface and do not accounts for concavities and sharp features of the specimen between the data points.

Figure 6.3 - Irregular Silicon piece suspended.

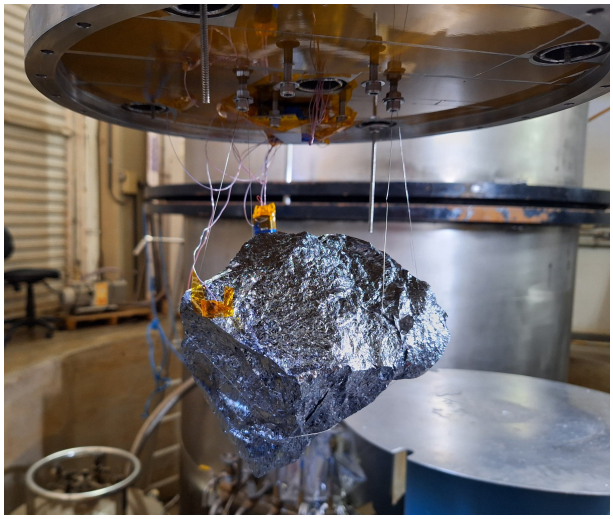

Irregular specimen suspended by titanium-aluminum-vanadium wires before closing the dewar. One can note a thermocouple fixed with kapton tape on the left side of the piece.

SOURCE: From the authors.

For this reason, we considered only the two first approximations and calculated an average of the results from the tape and FreeCAD methods, as they provided the closest approximation of the surface area. Therefore, it was used $A_{\mathrm{Si}} = 738.48\ \mathrm{cm}^2$ as the piece surface area.

6.2 The experiment run

Following the described methods, the sample was also suspended by titanium-aluminum-vanadium (Ti90Al6V4) wires, as the other runs. Figure 6.3 shows the experiment setup just before sealing the system and diving it in LN2.

Once again, temperature data acquisition started some minutes before the dewar was dived in LN2, but this data was removed from the analyzed set in order to avoid issues for temperature fitting when using the selected functions.

As mentioned in Chapter 4, four thermocouples were used to monitor both the specimen and shield (dewar) temperatures. In this run, they were T_1 and T_4 were positioned at the shield's top and bottom, respectively. The other two thermocouples, T_2 and T_3, were placed at the specimen's bottom and top, respectively (as Figure 4.2). Figure 6.4 presents the cooling-down curve for this experiment, displaying

Figure 6.4 - Cooling-down curves for experiment runs using the irregular piece.

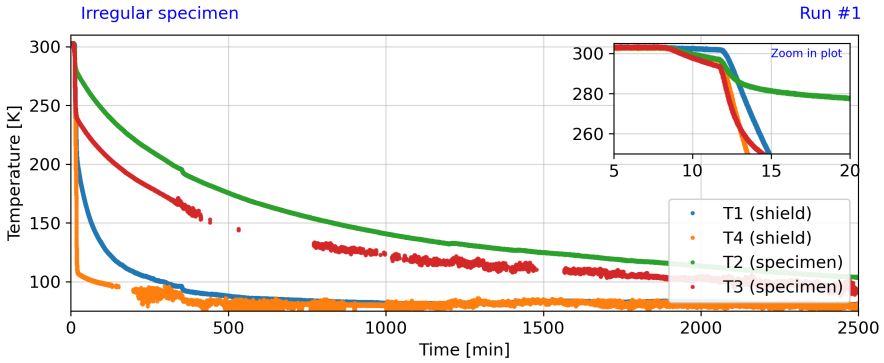

Cooling-down curves for this run using the irregular Si piece. The figure shows temperature data from all thermocouples. T_1 and T_4 (blue and orange) correspond to the dewar temperature channels, while T_2 and T_3 (green and red) represents specimen temperature measurements. Both T_3 and T_4 were malfunctioning. At the upper-right corner, a zoomed-in view of the cooling-down curves during the first minutes for the irregular Si piece run. We highlight that T_3 (red) closely follows the shield thermocouple T_4 (orange), indicating that its recorded data does not represent specimen's temperature and it is not reliable to emissivity calculations.

SOURCE: From the authors.

temperature readings from each thermocouple separately.

6.3 Identified issues during the run

As the experiment was running, it was observed that two thermocouples presented malfunctions, T_3 and T_4. These were responsible for acquiring data from the shield and the Si specimen, respectively. Besides to their failures, both thermocouples exhibited increased digital noise once they resumed operation, affecting data reliability.

The shield thermocouple (T_4) began to present this failures approximately at $t = 130$ min after the run started. This malfunction resulted in a complete loss of information during 1 h and 10 min. This gap accounts for about 5% of total analyzed dataset from this channel.

The specimen thermocouple (T_3) presented three major gaps throughout the experiment. The first and most significant failure started at $t = 400$ min and lasted for 6 h and 15 min, creating a substantial data loss. The second notable issue lasted only a few minutes, but it coincided with the critical temperature of 123 K. Finally, the third failure occurred around $t = 1460$ min and lasted 1 h and 45 min. Overall,

this loss of information for the specimen thermocouple represents about 20% of total analyzed dataset, including te important missing data around 123 K.

Additionally, a significant issue was identified in T_3 channel. As highlighted in Figure 6.4, during the first minutes of the experiment run, T_3 closely followed the shield thermocouple readings, T_4. This suggests that the recorded data from T_3 did not accurately represent the specimen's temperature and, therefore, it is not reliable to emissivity calculation purposes. The most plausible explanation for this behavior is that this thermocouple was not properly fixed to the specimen, leading to erroneous measurements that were contaminated by shield temperature.

Consequently, it was not possible to use T_3 reading in emissivity calculations. In Chapter 4, it is described that the Silicon specimen temperature used in Equation 4.9 would be a mean value of both specimen channels. Nevertheless, given the malfunction presented by T_3, it was only possible to calculate the derivative using T_2 data. This means we were forced to use only one thermocouple, located at the piece's bottom, as a representative temperature of the entire specimen.

As discussed previously, we are assuming uniform temperature distribution across the silicon piece. However, the measurements records only the local temperature at a specific point, which may not be representative of the entire specimen's surface. In this way, we expect that using one channel will introduce errors in emissivity results calculations. Despite this limitation, no alternative was available for this experimental run.

6.4 Emissivity results

In order to estimate Si emissivity for the irregular specimen, it was considered only the data from thermocouples T_1 and T_2, since they were the only ones to not present any malfunction. The mentioned channels were shield and piece temperatures, respectively.

Digital noise effects were reduced by a smoothing filter in temperature data and the derivative calculations. In addition, it was also used the Savitzky-Golay filter, as the methods of fitting data with exponential and polynomial equations. In other words, we followed the method used in Chapter 5.

The smoothing filter in this run used $k_1 = 50$ for temperature data. The same parameter was applied to smooth the calculated derivative. In addition, SavGol filter used window of $w_1 = 101$ and a polynomial order $p_{\text{order, 1}} = 3$. Once with

Figure 6.5 - Emissivity results for irregular shape piece.

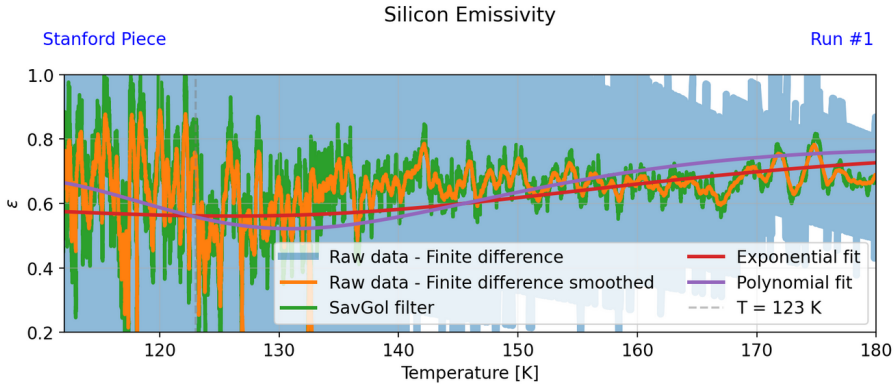

Emissivity results for irregular Si piece. Results using numerical differentiation by finite difference are shown in faded blue. Emissivity calculations using smoothed derivative calculations are in orange. The results using the SavGol filter are in green. Red and purple line shows the emissivity from exponential and polynomial fitting, respectively.

SOURCE: From the authors.

smoothed temperature dataset, we used numerical differentiation to estimate the derivative curve. Moreover, derivative curve from the fitted curve coefficients were used as alternative methods.

Emissivity results are summarized in Figure 6.5. One can note that we have large variations in data, even after passing the smooth filter. From all fitted curves, the exponential is the one that shows the most steady behavior.

As expected, the results also caries fluctuations. We highlight that this run presented more noise in thermocouple readings than the Stanford piece experiment. In order to have an representative value for effective emissivity, we estimated a mean value considering the different approaches and their errors, as seen in Figure 6.6.

We highlight that thermocouple low precision and noise in data led to higher errors in the estimated emissivity, as seem for raw data mean value. This raised the global average and increased the final error bar. Table 6.4 shows emissivity results for each derivative method.

6.5 Chapter summary

This chapter presented the results of the experiment which used an irregularly shaped Silicon specimen to estimate its emissivity around 123 K. Due to a limited liquid Nitrogen supply, only one experiment run was possible. A significant issue was

Figure 6.6 - Estimation methods compared for the irregular shape specimen.

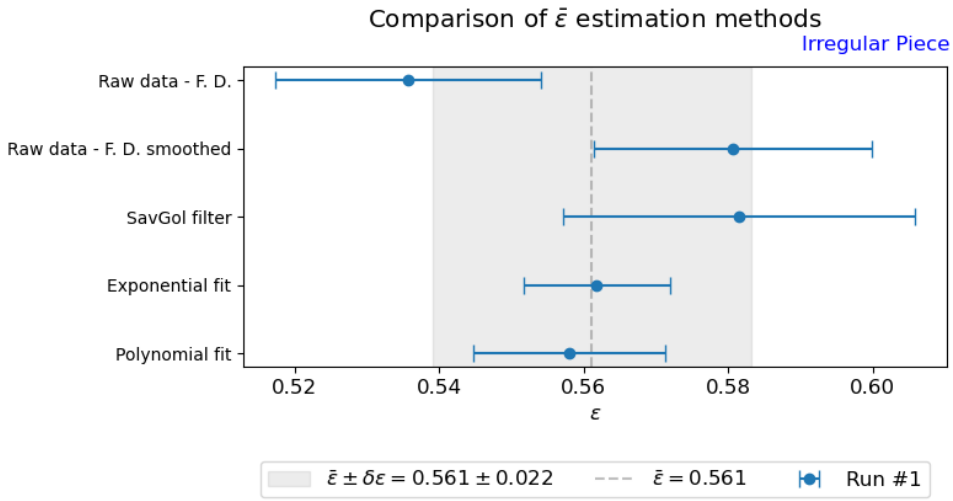

Emissivity results for all experimental runs using the irregular Si specimen. Dashed gray line shows the mean emissivity considering all results and the gray region shows the mean value estimated error.

SOURCE: From the authors.

Table 6.1 - Silicon emissivity results at 123 K for the irregular piece.

Data	Emissivity (ϵ)	Error ($\pm\delta\epsilon$)
Raw Data - Finite difference	0.536	0.018
Raw data - Smoothed derivative	0.581	0.019
SavGol Filter	0.581	0.024
Exponential fit	0.562	0.010
Polynomial fit	0.558	0.013

SOURCE: From the authors.

detected during the run: two thermocouples presented malfunction, resulting in considerable data gaps. Additionally, we noted that one of the specimen's thermocouple was not properly fixed, therefore its readings were not reliable to represent the piece temperature. Consequently, we were forced to use readings from only one channel, under the assumption of uniform temperature distribution across the piece. Silicon emissivity results at 123 K, calculated using different methods, are summarized in Table 6.4, and the mean emissivity result is $\bar{\epsilon} = 0.561 \pm 0.022$.

The following chapter will describe a theoretical model and compare it to emissivity results from the experimental runs.

7 THEORETICAL MODEL FOR SILICON EFFECTIVE EMISSIVITY AT CRYOGENIC TEMPERATURES

In this chapter, we present a theoretical model for calculating the emissivity of Silicon at cryogenic temperatures. We begin by treating Silicon as a semitransparent material for radiation emitted at temperatures around 123 K. Next, we outline how the theoretical approach estimates specimen's effective emissivity, and we compare it with the experimental results. Finally, we provide estimated emissivities for the test masses of LIGO Voyager, Cosmic Explorer, and Einstein Telescope.

7.1 Emissivity of a semitransparent material

An isothermal opaque body at temperature T emits radiation, as described in Chapter 4. However, none of the radiation generated within the body reaches the surface, meaning all the emitted radiation must, by definition, be generated by the surface itself.

In contrast, for a semitransparent radiator, some photons generated in its interior does reach the surface and is emitted into the surrounding medium. Hence, it is not possible to consider emissivity in such materials purely as a surface phenomenon. Instead, it is a **bulk phenomenon**, which will dependent on the body's geometry and volume (GARDON, 1956).

Silicon is semitransparent for wavelengths near the peak of the black body spectrum at 123 K. Consequently, photons at these wavelengths and originated inside a Silicon body can escape, join the photons emitted by the surface atoms, and contribute to total emitted radiation.

Comparing the spectral flux emitted by an isothermal semitransparent body with the corresponding hemispherical emissivity power of a black body at the same temperature, it is possible to define the hemispherical spectral emissivity. For a material of refractive index n, this is given by (GARDON, 1956):

$$\epsilon_{\lambda\chi} = 2 \cdot \int_0^{\frac{\pi}{2}} \left(1 - e^{-\frac{\alpha_\lambda \cdot \chi}{\cos\gamma}}\right) \Upsilon' \sin(\beta) \cos(\beta)\ d\beta\,. \tag{7.1}$$

The result presented in Equation 7.1[1] is in function of the product $\alpha_\lambda \cdot \chi$, known as

[1]Equation 24 in Gardon's paper is missing factor of 2. In this work, we use the corrected expression (Equation 7.1).

dimensionless thickness. This is the product of the body's "mean thickness"[2] (χ) and the absorption coefficient (α_λ), which is wavelength dependent. Additionally, β represents the angle of refraction, while γ is the incident angle at the body's border for internally emitted radiation.

The term Υ' is given by:

$$\Upsilon' = \frac{1}{2} \cdot \left[\frac{\tau'_\perp}{1 - \rho'_\perp e^{-\frac{\alpha_\lambda \cdot \chi}{\cos(\gamma)}}} + \frac{\tau'_\parallel}{1 - \rho'_\parallel e^{-\frac{\alpha_\lambda \cdot \chi}{\cos(\gamma)}}} \right] \tag{7.2}$$

where τ' is the fraction of light energy transmitted across the surface, and ρ' is the fraction that is reflected. Each fraction is separated in parallel and perpendicular polarization components.

The relation between τ' and ρ' is given by:

$$\tau'_i = 1 - \rho'_i \quad \text{for } i = \perp \text{ or } \parallel . \tag{7.3}$$

Also, the coefficient $\rho'_\perp$ can be expressed as

$$\rho'_\perp = \frac{\sin^2(\beta - \alpha)}{\sin^2(\beta + \alpha)} . \tag{7.4}$$

Similarly, for $\rho'_\parallel$:

$$\rho'_\parallel = \frac{\tan^2(\beta - \alpha)}{\tan^2(\beta + \alpha)} . \tag{7.5}$$

Finally, using the Snell's law:

$$\alpha = \arcsin\left[\frac{\sin(\beta)}{n}\right] \tag{7.6}$$

where n is the index of refraction. For Silicon, we will use $n = 3.4$ (EDWARDS; OCHOA, 1980).

[2] The meaning of the irradiator "mean thickness" will be further explored and clarified in Section 7.5.

Figure 7.1 - Hemispherical emissivity for a semitransparent material in function of its dimensionless thickness.

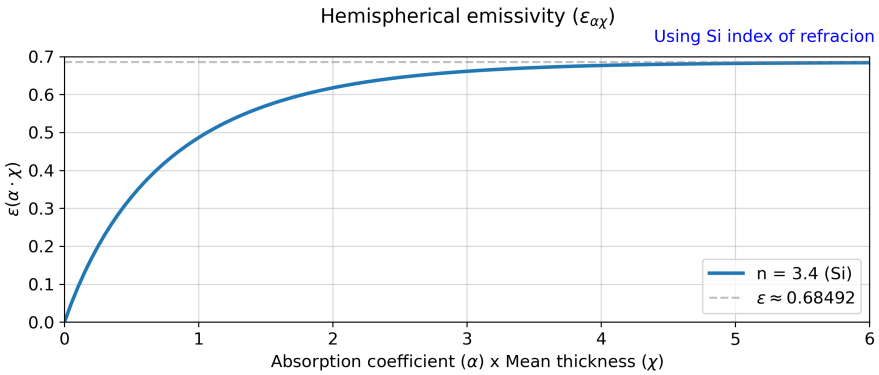

The blue curve shows the calculated hemispherical emissivity for a semitransparent material with a refractive index $n = 3.4$, such as Silicon. As one can note, the emissivity approaches an asymptotic horizontal limit for high dimensionless thickness, and it is nearly constant for $\alpha \cdot \chi \geq 4$. For Silicon, this limit is $\epsilon_{\max} \approx 0.68492$.

SOURCE: From the authors.

7.2 Total hemispherical emissivity

In practical applications, it is important to determine the total hemispherical emissivity, which accounts radiation in all directions and for all wavelengths. Figure 7.1 presents the hemispherical emissivity (ϵ) as function of the dimensionless thickness ($\alpha \cdot \chi$) , calculated using Equation 7.1. We highlight that, for a given semitransparent material with refractive index n, the hemispherical emissivity remains nearly constant when $\alpha \cdot \chi \geq 4$. This value can be reached either by the high radiator's thickness or by presenting a high absorption coefficient.

If one know the Silicon absorption coefficient for emitted radiation wavelengths around 123 K and the thickness of the specimens used in Chapters 5 and 6, the hemispherical emissivity can be estimated and compared with experimental results.

In this work, we used three approaches for effective emissivity calculations. The first method involves calculating a weighted average of the hemispherical spectral emissivities, where the weighting factor corresponds to the emissive power of black body radiation. Specifically, we considered a range of the black body spectrum around the peak of emission, ranging from λ_0 to λ_1. The total effective emissivity was determined as:

$$\bar{\epsilon} = \frac{\int_{\lambda_0}^{\lambda_1} B(\lambda, T) \cdot \epsilon_{\lambda\chi}}{\int_{\lambda_0}^{\lambda_1} B(\lambda, T) d\lambda} \, d\lambda. \tag{7.7}$$

The second approach involved computing a mean value for the absorption coefficient (α), as will be described in Section 7.4. A third one attempted to extend the mean absorption coefficient in wavelength by assuming values to the extinction coefficient, as further discussed.

7.3 Maximum emissivity approximation

An useful approximation for the maximum emissivity of a semitransparent material can be obtained considering the limit for $\alpha \cdot \chi \rightarrow \infty$ in Equations 7.1 and 7.2. In addition, using the Taylor series for the sine function

$$\sin\theta = \sum_{k=0}^{\infty} \frac{(-1)^k}{(2k+1)!} \theta^{2k+1} \, , \tag{7.8}$$

and the approximation $\alpha \approx \beta/n$, Equation 7.1 simplifies to:

$$\epsilon_{\max} \approx 2 \cdot \int_0^{\frac{\pi}{2}} \left[1 - \sum_{k=0}^{\infty} \left(\frac{n-1}{n+1} \right)^{4k+2} \right] \sin\beta \cos\beta \, d\beta \, . \tag{7.9}$$

This leads to:

$$\epsilon_{\max} \approx 1 - \sum_{k=0}^{\infty} \left(\frac{n-1}{n+1} \right)^{4k+2} \, . \tag{7.10}$$

The maximum value obtained from Equation 7.10 provides a reliable approximation for refractive index values in the range $n \in [1, 3.75]$, with a percentage error of less than 5%. For the refractive index of silicon, the estimated maximum emissivity is $\epsilon = 0.67359$. The maximum value calculated evaluating Equation 7.1 for silicon using very high $\alpha \cdot \chi$ product is $\epsilon = 0.68492$. Therefore, this approximation result is deviated by just 1.6%.

7.4 Absorption coefficient

Silicon at low temperatures presents low intrinsic carrier density (MISIAKOS; TSAMAKIS, 1993). Consequently, in the temperature regime relevant to this work,

Figure 7.2 - Extinction coefficient for Silicon at different temperatures.

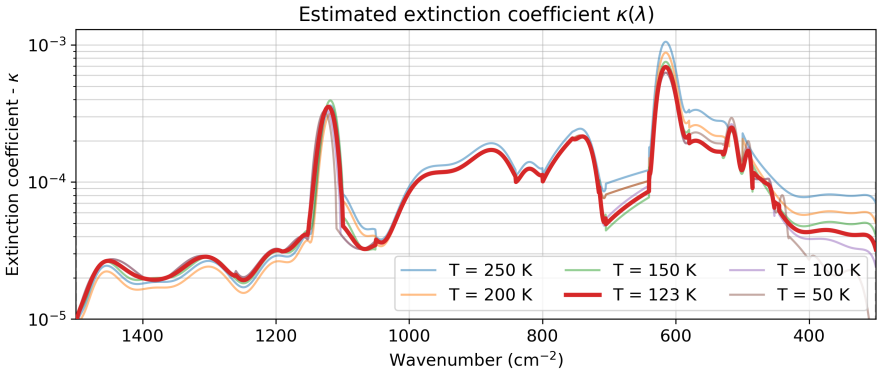

Estimated curves for Silicon extinction coefficient as function of wavenumber (cm^{-1}). The plot presents curves for different temperatures and, in bold red line, data for $T = 123$ K used in this work.

SOURCE: Reading (2023).

free carrier absorption do not significantly contribute to the total absorption. Instead, absorption is primarily dominated by multi-phonon absorption (CONSTANCIO et al., 2020), which is given by:

$$\alpha = \frac{4\pi\kappa\left(\lambda\right)}{\lambda} \tag{7.11}$$

where $\kappa\left(\lambda\right)$ is the extinction coefficient.

The extinction coefficient κ is wavelength-dependent. For these calculations, we used data available online by Reading (2023), which provided a plot of the Silicon extinction coefficient as a function of the wavenumber for temperatures ranging from 50 K to 300 K, in 50 K intervals.

Since no numerical data was online – only the figure – we estimated curves to reproduce the extinction coefficient values from the provided plot. Furthermore, no curve was available for $T = 123$ K. To address this issue, we estimated $\kappa(123\ \mathrm{K})$ by taking the mean value between the 100 K and 150 K curves. We aimed to replicate the nuances of this data as accurately as possible. Figure 7.2 shows the estimated curves for Silicon extinction coefficients as a function of the wavenumber (in cm^{-1}) at different temperatures. The red line represents $\kappa\left(\lambda\right)$ for $T = 123$ K.

Figure 7.3 - Black body emission at 123 K compared with available Silicon extinction coefficient available for this work.

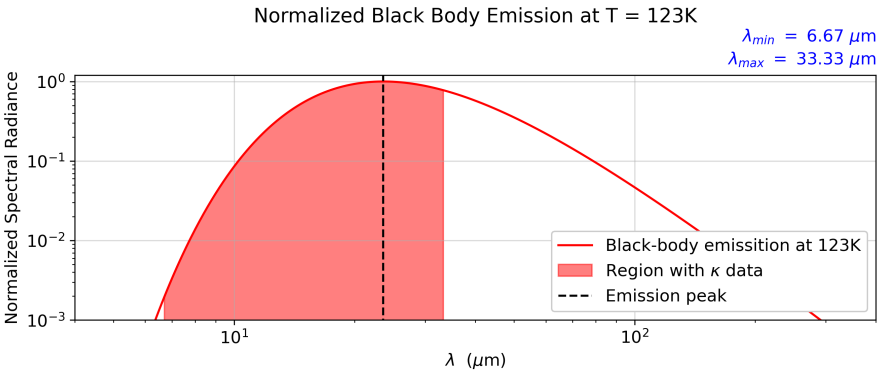

Normalized black body emission spectrum at 123 K, showing the spectral radiance as a function of wavelength, in red line. The shaded region indicates the range where extinction coefficient data for Silicon is available for this work, which includes the emission peak, marked by a dashed black line.

SOURCE: From the authors.

The effective emissivity estimation considered a mean absorption $\bar{\alpha}$. In order to calculate it, Equation 7.11 was weighted according to the emission at temperature T for wavelengths around the emission peak. This approach is expressed as:

$$\bar{\alpha} = \frac{\int_{\lambda_0}^{\lambda_1} B(\lambda, T) \cdot \alpha(\lambda)}{\int_{\lambda_0}^{\lambda_1} B(\lambda, T) d\lambda} d\lambda. \tag{7.12}$$

However, the available wavelengths data ranges from 300 cm^{-1} to 1500 cm^{-1}. This means that the extinction coefficient data partially covers the black body emission spectrum at 123 K, although it extends beyond the peak of emission at $\lambda_{\text{peak}} = 23.55$ μm. In terms of wavelength, the covered region starts at $\lambda_{\text{min}} = 6.67$ μm to $\lambda_{\text{min}} = 33.33$ μm.

Figure 7.3 illustrates how much of the spectrum is covered by κ data. Radiation emitted at λ_{min} accounts for 0.21% of peak emission energy, while λ_{max} represents 77.5%.

It is important to note that while the region around the peak is covered, the absence of κ data may lead to an underestimation of effective emissivity if Equation 7.12 considers all wavelengths. Therefore, we followed two different methods.

Table 7.1 - Mean Silicon absorption coefficient at 123 K calculated considering $\kappa = 0$ or $\kappa = 1 \cdot 10^{-6}$ in the data uncovered region.

Extinction coefficient	Wavelength range μm	Mean absorption $\bar{\alpha}$
$\kappa_{\text{out}} = 0$	6.67 – 33.33	67.864 cm^{-1}
$\kappa_{\text{out}} = 1 \cdot 10^{-6}$	6.33 – 156.33	34.469 cm^{-1}

SOURCE: From the authors.

The first method considered only the available wavelengths for the extinction coefficient data, i. e., from 6.67 μm to 33.33 μm. The second method considered a constant minimum value of $\kappa_{\text{out}} = 1 \cdot 10^{-6}$ and a wider range for wavelength, from 6.33 μm to 156.33 μm. These limits were chosen to match wavelengths which normalized spectral radiance for a black body at 123 K is 0.001.

Table 7.1 summarizes the results for Silicon mean absorption coefficient $\bar{\alpha}$. One can note the effect of κ_{out} over a large range of wavelengths with no absorption data. The mean absorption for this method is almost half of the result obtained by the first approach.

Following our assumptions, the emissivity for a semitransparent material do not depend only on absorption coefficient. It is needed to account also the body thickness. Therefore, even with a small value of mean absorption, if the product $\alpha \cdot \chi$ is sufficiently high, as mentioned in Section 7.2, the dimensionless thickness will result in an effective emissivity near the maximum. In despite of that, small Silicon specimens, such as the one used by (CONSTANCIO et al., 2020), will have a very small χ. Consequently, the difference between the two mean absorption coefficients methods will lead to significantly different emissivities.

In the next section, we will discuss the thickness (χ) computations techniques and the results for the specimens used in the experiments.

7.5 Mean thickness

In his paper GARDON (1956), developed a theory for semitransparent sheet with thickness χ. In the present work, we are using the same mathematical model to estimate the effective emissivity of semitransparent silicon at cryogenic temperatures. Therefore, it is needed to define a "thickness" to the radiator.

In general terms, the thickness is a quantity related to the distance that a photon

generated in the radiator's interior can travel before reaching the body's surface. Greater the thickness, greater the distance, and vice-versa. It is also important to consider that the photon can, in principle, be emitted in any direction.

In this sense and in order to quantify χ, we defined the mean thickness as **the average distance a photon, emitted inside the radiator, travels until reaching the surface**. This requires calculating the distance for multiple points within the radiator to the surface, considering all directions. The mean thickness is then given by summing all computed distances and dividing by the total number of paths:

$$\chi = \langle d \rangle = \frac{1}{N} \sum_{i=0}^{N} d_i \tag{7.13}$$

where N represents the number of paths for points inside the radiator's body, and d_i the travel distance from the i-th path.

Furthermore, the light beam emitted inside the radiator can be internally reflected before escaping it. This effect should be considered since it would increase the mean thickness.

7.5.1 Code implementation for mean thickness

A Python script was developed in order to implement the described ray-tracing approach and estimate the mean thickness for different radiator's geometries: a rectangular prism, a cylinder and also the irregular shape for the Silicon piece.

First, it creates grid of points within the given geometry, forming a collection of points G. From these points, light paths will be further calculated in isotropical angular directions. A set of key parameters is defined, such as the dimensions of the radiator, also the grid spatial resolution in the x, y, and z directions, and the angular resolution $\Delta\theta$ for ray propagation directions.

The core computational routine is encapsulated in a function that simulates the propagation of light beams originating from a given point $p_i = (x_i, y_i, z_i)$ selected from the grid G. For each of them, it creates a spherical coordinate system (ρ, θ, ϕ) centered at p_i. The values of ρ, θ and ϕ will increase by small increments: $\Delta\rho$, $\Delta\theta$ and $\Delta\phi$, respectively.

The distance calculation begins by selecting a direction defined by a pair of angular

coordinates, θ and ϕ, which determine the latitudinal and longitudinal orientation, respectively. The magnitude ρ in (θ, ϕ) direction is created with small initial value and incrementally increased in discrete steps $\Delta\rho$ until it reaches the surface of the structure. The total distance for a given beam path (d_{i})is then recorded. Once the surface is reached, it adjusts the angular coordinates and repeats the distance calculation for p_i.

The cylinder's script considers a reflecting surface at the top. In addition, it was implemented a routine for internal reflections. In this sense, once the surface is reached, the code calculates the incident angle and test if it is grater than the critical angle γ, according to Snell's Law. If so, it changes the angular coordinates, and follows to increasing ρ until the beam reaches the radiator's surface again. Consequently, it accounts only one internal reflection when it occurs.

This process continues iteratively, covering a set of isotropical orientations for each reference point p_{i}. Upon completing the computations, the algorithm proceeds to the next point in the G until covering them all. The total number of computed light paths N and their cumulative sum $\sum d_i$ are recorded. Finally, the mean thickness is determined by dividing the sum of all measured distances by the total number of computed paths (Equation 7.13).

In order to grant an isotropic distribution of light paths emerging from the point p, the script must adjust the longitude angle increment $\Delta\phi$ according to latitude θ. In this way, no latitude will be privileged with an unequal distribution of points. The relationship between the $\Delta\theta$ and $\Delta\phi$ is given by:

$$\Delta\phi = \frac{\Delta\theta}{\sin(\theta)} \tag{7.14}$$

In summary, it was possible to calculate the mean thickness for the different geometries. However, this script was improved in order to reduce the computational cost.

7.5.2 Irregular shape specimen code

Different scripts were written for different specimens geometry. The irregular specimen code presented a particular challenge, since it is not symmetric and not similar to any regular convex polyhedron.

Figure 7.4 - Modeled convex hull compared to scanned irregular silicon specimen vertices.

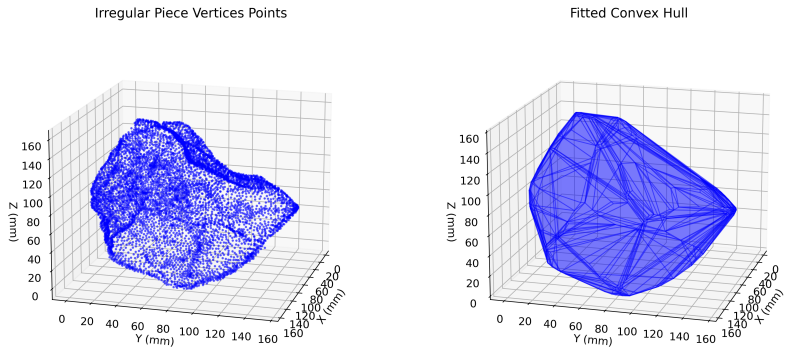

Modeled convex hull compared to scanned irregular silicon specimen vertices.
SOURCE: From the authors.

However, during the surface area estimation (described in Subsection 6.1.1), the specimen was scanned and modeled by a collection of vertices-like points. As a solution for defining the Si piece boundaries in space, we modeled a convex hull to represent the specimen. Figure 7.4 shows a comparison between the vertices points and the modeled convex hull.

Particularly, this specimen presents a rough surface and the scanned vertices reproduces considerably well many of its features. However, the convex hull smoothed the surface, neglecting concavities and sharp features of the specimen between the data points. Consequently, this error will propagate through mean thickness calculations, although this was the best solution found to this problem.

The script checks if ρ is inside the convex hull. If so, it continues iterating discrete steps $\Delta\rho$. Once outside the convex hull, it records the distance d_i and changes direction, as described. For this script, however, no internal reflections were considered.

7.5.3 Optimizing mean thickness algorithm

In order to return a result with sufficient precision, the original function must increase ρ in small increments $\Delta\rho$. However, this can lead to high computational cost. To address this, it was implemented an adaptive $\Delta\rho$.

In this new method, the code starts with a large initial step size $\Delta\rho_0$ and this is progressively refined upon encountering the radiator's surface. This adaptive step-size ensures accurate determination of distance d_i and stops when the distance incre-

ment is less than a predefined precision $\Delta\rho_{\min}$. On the other hand, if $\Delta\rho_0$ causes the beam to exit the specimen on the first attempt, the script restarts the process using a reduced step size, $\Delta\rho_0/2^m$, $m \geq 1$. This adjustment continues iteratively, incrementing m until $\Delta\rho_0/2^m < \Delta\rho_{\min}$

Another issue is the total number of light paths N in function of the longitudinal increment $\Delta\phi$. This relation is given by

$$N = N_p \cdot \left[2 + \sum_{i=0}^{N_\theta} \left\lfloor \frac{2\pi \sin(\theta_i)}{\Delta\theta} \right\rfloor \right] \tag{7.15}$$

where $N_\theta = 2\pi/\Delta\theta$, total points for a given latitude, and N_p is the number of points collected in G. Therefore, since N is inversely proportional to $\Delta\theta$, high angular resolution produces a very large number of light paths to calculate.

To reduce the computational cost associated with processing a large number N, the script used parallel computing via the Python `joblib` library, distributing the workload into multiple cores. This modification significantly enhances performance, enabling a faster analysis of mean thickness.

Internal reflections effects the final mean thickness result, since it will increase the light paths d_i while not changing N. This was successfully implemented for cylindrical radiators. Symmetry artifacts were used in order to simplify calculations and reduce computational cost.

While the algorithm is optimized through parallelization and adaptive step-size refinement, its computational complexity remains as a limiting factor, particularly for high angular resolution simulations. Future improvements could involve optimizations in ray-tracing logic, improved step-size adaptation strategies, and the incorporation of visual analytics for enhanced interpretation.

7.5.4 Men thickness results

This subsection summarizes the mean thickness calculated according to the described method. Table 7.2 shows the results, according to the input parameters. Distances between two points inside the collection G are given by Δx_i, where i ranges from 1 to 3 and $(x_1, x_2, x_3) = (x, y, z)$. The latitudinal step is given by $\Delta\theta$, in degrees, and the minimum precision required is given by $\Delta\rho_{\min}$, in millimeters. Finally, the mean thickness χ is in millimeters.

Table 7.2 - Mean thickness calculated for the different specimens.

Specimen	Δx_i (mm)	$\Delta\theta$ (deg)	$\Delta\rho_{\min}$ (mm)	χ (mm)
Rectangular piece	0.5	5.0	0.1	10.5
Stanford piece	1.0	5.0	0.1	66.9
Irregular piece	3.0	5.0	1	46

SOURCE: From the authors.

We highlight that the cylinder geometry script accounts for the possibility of one internal reflection per light beam. This is not true for the irregular shape script, nor the rectangular prism. Therefore, its mean thickness may be greater than the result in Table 7.2.

In addition, it was needed to set different input values for the parameters according to each specimen geometry due to computational cost. Mean thickens for a rectangular prism specimen used by Constancio et al. (2020) was also calculated.

7.6 Chapter summary

This chapter developed a theoretical model for silicon emissivity at cryogenic temperatures. It began by addressing the concept of emissivity for semitransparent materials. Since photon emitted within a semitransparent radiator can reach the surface and contribute to radiative heat transfer, emissivity is not considered a surface phenomenon, but a bulk one. Consequently, emissivity is given by Equation 7.1, which depends on the product of two key parameters: the mean thickness χ and the absorption coefficient α. The mean thickness is associated with the geometry and volume of the radiator, while the absorption coefficient α characterizes the material's optical properties. Subsequently, the methods to estimate both parameters were presented, along with the results for Silicon absorption coefficient around the emission peak at 123 K, and the mean thickness of the specimens used in the experiments.

The following chapter will present the calculated effective emissivity values for the silicon specimens based on this model. In addition, it will compare these theoretical results to experimental measurements and discuss implications for future gravitational wave detectors.

8 THEORETICAL SILICON EFFECTIVE EMISSIVITY RESULTS

This chapter is dedicated to the theoretical estimation for the effective emissivity of Silicon specimens and compare them with the experimental results. Additionally, it discusses the theoretical projections relevant for future gravitational waves detectors.

8.1 Effective emissivity for Silicon at 123 K

The effective emissivity of Silicon at 123 K was estimated by three distinct approaches. The first method involves calculating a weighted average of the hemispherical spectral emissivity, where the weights are given by the spectral distribution of black body radiation. This integration considered wavelengths that the extinction coefficient was available. Therefore:

$$\bar{\epsilon} = \frac{\int_{\lambda_0}^{\lambda_1} B(\lambda, T) \cdot \epsilon_{\lambda\chi}}{\int_{\lambda_0}^{\lambda_1} B(\lambda, T) d\lambda} \, d\lambda. \tag{8.1}$$

The second approach estimates the effective emissivity based on the mean absorption coefficient, $\bar{\alpha}$, integrated over the same range of available extinction coefficients for Silicon at 123 K. The resulting effective emissivity is denoted as $\epsilon\left(\bar{\alpha}\right)$, with the corresponding wavelength interval covering from 6.67 μm to 33.33 μm.

On he other hand, the third method attempted to extend the wavelength range to include regions where the normalized spectral radiance is equal or greater than 0.001. This leads to an extended mean absorption coefficient $\bar{\alpha}_{\text{ext}}$, and the corresponding effective emissivity is labeled as $\epsilon\left(\bar{\alpha}_{\text{ext}}\right)$. In this case, the wavelength interval ranges from 6.33 μm to 156.33 μm.

A summary of the results is shown in Table 8.1. The values calculated to the rectangular prism correspond to the specimen studied by Constancio et al. (2020).

Table 8.1 - Effective emissivity results for Silicon specimens.

Specimen	$\bar{\epsilon}$	$\epsilon\left(\bar{\alpha}\right)$	$\epsilon\left(\bar{\alpha}_{\text{ext}}\right)$
Rectangular prism	0.312	0.408	0.264
Stanford	0.603	0.680	0.636
Irregular	0.556	0.665	0.582

SOURCE: From the authors.

Table 8.2 - Effective emissivity results comparison for the rectangular prism specimen.

Experimental result	$\bar{\epsilon}$	$\epsilon(\bar{\alpha})$	$\epsilon(\bar{\alpha}_{\text{ext}})$
0.41 ± 0.01	0.312	0.408	0.264

SOURCE: Constancio et al. (2020).

8.2 Comparative analysis

This section presents a comparative analysis between the theoretical effective emissivity results and the experimentally estimated values in the literature and in this work. The first case to be addressed is the rectangular prism, followed by the other two specimens.

8.2.1 Rectangular prism specimen

For the rectangular prism specimen, the estimated effective emissivity determined experimentally is $\bar{\epsilon}_{\text{exp}} = 0.41$ (CONSTANCIO et al., 2020). It was considered as experimental error $\delta\epsilon = 0.01$. Table 8.2.1 presents a comparison between this this experimental value and the theoretical estimations obtained in this work.

The result considering a mean absorption coefficient, i.e., $\epsilon(\bar{\alpha}) = 0.408$ demonstrates good agreement with the experimental result. This suggests that to model Silicon as a semitransparent radiator, including the chosen method for calculation considering a mean absorption coefficient $\bar{\alpha}$, provides a reliable approximation for silicon effective emissivity in cryogenic conditions.

In contrast, the result from the weighted average of spectral emissivity, $\bar{\epsilon} = 0.312$, underestimates the experimental result. This indicates that the absence of data for portions of the infrared spectrum, where there is non-negligible emission, led to an underestimated mean effective emissivity. Additionally, the third estimated value, $\epsilon(\bar{\alpha}_{\text{ext}}) = 0.264$, which extends the integration to wavelengths corresponding to just 0.1% of the normalized spectral radiance, significantly deviates from the experimental result.

However, it is important to note that the mean thickness script for this specimen does not consider internal reflections. By our calculations with other specimen geometries, results considering implemented internal reflections can increase the mean thickness by a factor of about 2. Consequently, in this assumption, the case with the

best theory-experiment agreement is given by the extended absorption coefficient, resulting in $\epsilon\left(\bar{\alpha}_{\text{ext}}\right) = 0.404$. The other results deviates significantly with this new mean thickness.

8.2.2 Stanford specimen

For the Stanford specimen, the experimental effective emissivity was measured as $\bar{\epsilon}_{\text{exp}} = 0.627 \pm 0.007$. Table 8.2.2 summarizes the comparison with the theoretical results.

Table 8.3 - Effective emissivity results comparison for the Stanford specimen.

Experimental result	$\bar{\epsilon}$	$\epsilon\left(\bar{\alpha}\right)$	$\epsilon\left(\bar{\alpha}_{\text{ext}}\right)$
0.627 ± 0.007	0.604	0.680	0.636

SOURCE: From the authors.

Considering the experimental effective emissivity error for the Stanford specimen, the best agreement was found using the extended spectral range approach ($\epsilon\left[\bar{\alpha}_{\text{ext}}\right] = 0.636$). Although this method integrates absorption over a broader wavelength range, it extrapolates extinction coefficient absorption data and consider a possible contribution to emissivity generated in that spectral region.

The Stanford prism results suggest that extending the absorption integral beyond the limited spectral range leads to the best theoretical-experimental agreement for calculating effective emissivity. Internal reflections and reflections in the mirrored face contributes to increase mean thickness width. This, when combined with a lower absorption coefficient α, results in a theoretical emissivity that agrees with the experimental result.

8.2.3 Irregular specimen

For the irregular specimen, the experimentally measurement is $\bar{\epsilon}_{\text{exp}} = 0.561 \pm 0.022$. As summarized in Table 8.2.3, two of three estimates are the closest from the experimental result: $\bar{\epsilon}$ and $\epsilon\left(\bar{\alpha}_{\text{ext}}\right)$.

Although it is not possible to distinguish between the two approaches, all of them uses the proposed theoretical model and agrees with the experimental result. It suggests that the theory assumptions, particularly regarding bulk radiative behavior,

Table 8.4 - Effective emissivity results comparison for the irregular specimen.

Experimental result	$\bar{\epsilon}$	$\epsilon(\bar{\alpha})$	$\epsilon(\bar{\alpha}_{\text{ext}})$
0.561 ± 0.022	0.556	0.665	0.582

SOURCE: From the authors.

are valid to estimate effective emissivity of semitransparent materials at cryogenic temperatures. Moreover, we highlight the irregular shape mean thickness script do not considers internal reflections. Unfortunately, this case is too complex to implement this feature. Moreover, we highlight the irregular shape mean thickness code do not considers internal reflections. Unfortunately, this case is too complex to implement this feature.

8.2.4 Important considerations

All theoretical results for the different specimens emphasizes the significance of considering internal reflections in the emissivity model, more precisely in the mean thickness calculation. To determine the most accurate theoretical approach, it is essential to incorporate this feature into the simulation scripts.

A increased mean thickness by internal reflections leads to best theory-experiment agreement when using a lower mean absorption coefficient. This last, according to our case study, is given by extending the spectrum range to higher wavelengths and considering the extinction coefficient as a constant, $\kappa_{\text{out}} = 1 \cdot 10^{-6}$. In other words, the increased mean thickness combined with the lower absorption coefficient $\bar{\alpha}_{\text{ext}}$ leads to a theoretical emissivity in agreement with the experimental result for all specimens.

However, despite the potential advantages of including an extended wavelength range to the emissivity estimation, it is important to consider some limitations. First, the energy contribution of photons beyond the extinction coefficient data range can be negligible far beyond the emission peak. The extinction coefficient for this range in question was extrapolated. This can introduce uncertainties to the result. We considered a constant value κ_{min}, although it is also possible that real extinction coefficient can be different from it, including a null value.

Furthermore, improving the quality of experimental data, mainly for the irregular specimen, is important for reducing the uncertainty associated with emissivity mea-

surements. This can be achieved by repeating the experiment with an increased number of thermocouples, strategically positioned on the specimen allowing more accurate temperature follow-up.

Finally, more precise calibration of temperature channels and enhanced data acquisition techniques and precision would further reduce noise and variability. Together, these refinements will produce a narrower uncertainty range, and reinforcing the validation of the theoretical approach.

8.3 Effective emissivity for LIGO Voyager, Cosmic Explorer, and Einstein Telescope test masses

Here it is presented the effective emissivity estimations for LIGO Voyager, Cosmic Explorer and Einstein Telescope test masses according to the proposed model. The geometric parameters used in calculations were as follows: for LIGO Voyager test masses, a radius of $r_{\mathrm{V}} = 225$ mm and a length of $l_{\mathrm{V}} = 550$ mm; for Cosmic Explored, $r_{\mathrm{CE}} = 400$ mm and $l_{\mathrm{CE}} = 500$ mm; and for Einstein Telescope, $r_{\mathrm{ET}} = 250$ mm and $l_{\mathrm{ET}} = 500$ mm. All mean thickness calculations used a spacial resolution $\Delta x_i = 5$ mm, an angular resolution of $\Delta\theta = 5.0°$, and a precision of $\Delta\rho_{\mathrm{min}} = 0.1$ mm.

Mean thickness, mean absorption coefficient and effective emissivity results are summarized in Table 8.3. Both LIGO Voyager and Cosmic Explorer presented high dimensionless thickness values ($\chi \cdot \alpha$), which lead to estimated emissivity close to the maximum limit: $\epsilon_{\mathrm{V}} = \epsilon_{\mathrm{CE}} = 0.685$. These detectors are designed to operate at 123 K.

In contrast, Einstein Telescope is expected to operate at significantly lower temperature, around 10 K. As discussed in Section 7.4, extinction coefficient data are not available for such low temperatures. Therefore, for the purpose of this calculations, we assumed a temperature of $T = 50$ K for Einstein Telescope and already ex-

Table 8.5 - Effective emissivity results for future cryogenic gravitational wave detects' test masses.

Detector	Temperature (K)	χ (mm)	α (cm^{-1})	Emissivity (ϵ)
LIGO Voyager	123	383.5	34.5	0.685
Cosmic Explorer	123	415.5	34.5	0.685
Einstein Telescope	50	578.8	0.5	0.235

SOURCE: From the authors.

pecting a overestimated result. Under these conditions, the effective emissivity was estimated as $\epsilon_{\mathrm{ET}} = 0.235$.

Despite the relatively large mean thickness for Einstein Telescope, its emissivity is significantly reduced by the absorption coefficient. It is important to note that available extinction coefficient data do not cover the peak of emission for a black body at $T = 50$ K. Consequently, it is expected that the major contribution from the emission peak is not accounted. Furthermore, the actual operational temperature of the test masses is 10 K, significantly lower than the assumed 50 K. This potentially overestimates the real ET theoretical emissivity result, and it is possibly much less than $\epsilon_{\mathrm{ET}} = 0.235$.

Nevertheless, the results for LIGO Voyager and Cosmic Explorer are promising. Assuming $\epsilon = 0.685$, Voyager test mass would radiate approximately 7.4 W of thermal power. Cosmic Explorer would be able of emit around 12.5 W. These calculations consider a surrounding shield at 80 K (see Figure 4.1). Following Adhikari et al. (2020) work, these calculations consider coated face emissivity $\epsilon_{\mathrm{face}} = 0.5$. For reference, there is an optimistic estimation that Voyager test masses will absorb around 6.3 W from the laser (ADHIKARI et al., 2020). Therefore, an emissivity of $\epsilon = 0.685$ combined with large test masses dimensions leads to an sufficient emitted power to maintain operating temperature around 123 K.

Impurities in the Silicon test mass substrate can raise the temperature due to photon absorption. Nevertheless, considering the effective emissivity results and the total power the test mass can emit, there is a safety margin that allows for continued operation within acceptable limits.

In this sense, based on the emissivity results, it is not necessary to cover the Voyager test mass' barrel face with a high-emissivity black ink. Nevertheless, it is important to consider that Silicon presents a high quality factor for mechanical modes around 123 K (NAWRODT et al., 2008). Therefore, there could be an motivation to use the ink to lower the mechanical Q-factor and avoid issues involving parametric instabilities.

8.4 Chapter summary

This chapter presented theoretical estimates of the effective emissivity of Silicon at 123 K, calculated for three different specimens and compared to the corresponding experimental results. The comparison highlights the importance of implementing

internal reflections into the computational scripts, as this feature has a significant influence on the final result. Assuming mean thickness with internal reflections, emissivity estimations which consider the mean absorption coefficient averaged over a broader spectral region showed the best agreement with the experimental results. This indicates the importance of including contributions from wavelengths from this extended region.

The model was then extended to estimate the effective emissivity of LIGO Voyager, Cosmic Explorer, and Einstein Telescope test masses. For Voyager and Cosmic Explorer, the estimated emissivity was $\epsilon = 0.685$. In contrast, it was not possible to estimate precisely the emissivity for Einstein Telescope, due to lack of extinction coefficient data at the designed operating temperature. The data available covers wavelengths far the emission peak. The reported value was $\epsilon_{\mathrm{ET}} = 0.235$, calculated assuming a temperature of 50 K. Therefore, this probably overestimates the true emissivity.

Nonetheless, results for Voyager and Cosmic Explorer are promising. Based on $\epsilon = 0.685$, both test masses are expected to radiate around 7.4 W and 12.5 W of thermal power, respectively, assuming a surrounding shield of 80 K. These values can be higher if one considers lower shield temperatures, reaching 8.5 W for Voyager using 60 K shields. Therefore, considering the emissivity results, it is not necessary to paint test masses barrel face with a high-emissivity black ink.

Next chapter is dedicated to discuss the Newtonian noise introduced by a cooling-down system intended to create a cold environment of 80 K around the test masses, i.e., the shields. It will enabling them to thermally radiate heat and maintain thermal stability.

9 NEWTONIAN NOISE INTRODUCED BY IMPELLERS IN LIGO VOYAGER AND COSMIC EXPLORER

Since future ground-based gravitational wave detectors, such as LIGO Voyager and Cosmic Explorer, are proposing the use of cryogenics, they will require a cooling-down system capable of removing heat from test masses and maintaining its low temperature. As discussed in chapter 4, the high vacuum inside the chambers makes air convection and conduction negligible. Furthermore, metallic links to conduct heat from the test masses could introduce noise by the vibration modes (BAJPAI et al., 2022; YAMADA et al., 2021) and by ground motion coupled through the links itself.

The third alternative is to remove the required heat by radiation. This choice started the silicon emissivity at 123 K question, addressed in the last chapters.

In order to create a cold environment surrounding the test masses, a closed-loop pipeline in which a sub-cooled (65–77 K) liquid nitrogen (LN2) is circulating can be used. However, this system can introduce Newtonian noise due to bubble formation within the pipe. This noise was addressed by Bonilla et al. (2021).

On the other hand, the LN2 flux will require a pumping device. GWINPE's propose is to use a magnetically driven rotating impellers. However, this mechanism will also introduce Newtonian noise in the system.

In this chapter, we present a model for the gravitational interaction between the impellers and the test masses. In addition, the Newtonian noise produced by the impellers are also estimated and used to evaluate the viability of this cooling-down system.

9.1 Newtonian noise model

In order to estimate the Newtonian noise introduced by the impellers, we first calculate the gravitational interaction between each impeller and the test mass. Consider n_p impellers of n_b blades. Each blade was modeled as a point mass circulating a central point, which represents the impeller's center. The frequency of rotation is f (in Hz).

We are taking into consideration a pipeline system that includes a serpentine around the test mass cold shield, and a liquid Nitrogen flux produced by, at least, two impellers: one at the input and one at the output. In addition, the vector normal to

the impeller's plane is pointed towards the test mass symmetry axis. Furthermore, the axis formed by the impellers' centers is parallel to the same test mass symmetry axis, and these two are separated by a distance x_0. A vector $\vec{r}$ extends from the center of mass of the test mass to each blade (point masses), forming an angle θ (azimuth angle) with the cylinder's axis of symmetry.

The gravitational force exerted on an uniform cylinder by a point mass was investigated by Lockerbie et al. (1996). The axial acceleration per unit mass can be expanded in terms of the the ratio of cylinder length l, and the distance of the point mass to the center of the cylinder r as follows:

$$\alpha\left(r,\theta\right)=G\cdot\sum_{n=0}^{\infty}\left[\frac{P_{2\mathrm{n}+1}\left(\cos\theta\right)}{r^{2}}\left(\frac{l}{2r}\right)^{2n}\sum_{k=0}^{n}\binom{2n+1}{2k}\frac{P_{2\mathrm{k}}\left(0\right)}{k+1}\left(\frac{2b}{l}\right)^{2k}\right], \tag{9.1}$$

where b is the cylinder radius, and θ is the azimuthal angle, as shown in Figure 9.1. In addition, $P_k(x)$ represents the k-th Legendre polynomial.

Equation 9.1 results in the axial acceleration $\alpha\left(r,\theta\right)$ due to each impeller blade at a given moment in time. Contributions of all blades must be considered and summed in a total axial acceleration for one specific impeller. The sum of all impellers' axial acceleration leads to the total axial acceleration. Furthermore, the blades rotate with frequency f resulting in a time series for blades' position, as for the axial acceleration.

In Figure 9.1 part a), one can see a representation of the coordinate system chosen for the calculations. The point mass is represented by a dot and the test mass, side viewed, by a rectangle. In general, the impellers' centers are at the points $(x_0, 0, z)$. Considering $l/2$ the half length of the test mass and the origin of the coordinates at the cylinder center of mass, as in (9.1), the impellers' centers are located at the points $(x_0, 0, l/2)$ and $(x_0, 0, -l/2)$.

Another view for the system is shown in Figure 9.1 part b), using a general position for the impeller's center (small black dot). Its position is at the point $(x_0, 0, z)$. The blades, considered point masses, are represented by three dots.

For a given configuration of n_p, n_b, x_0, and f, the model outputs a total axial acceleration time series. Once calculated its Fourier transform, it is integrated twice in the frequency domain, resulting in the Power Spectral Density (PSD) of displacement. Finally, taking the square root of the PSD, it calculates the Amplitude Spectral

Figure 9.1 - Coordinate system for the noise calculations.

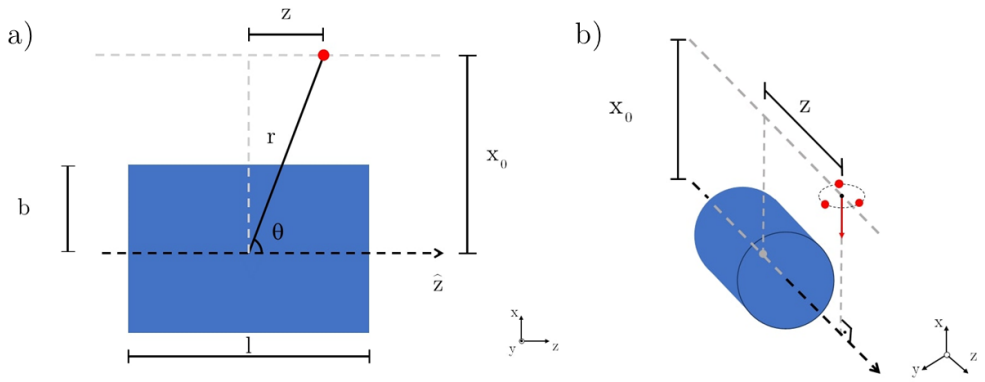

The impellers blades are represented by dots. The vector normal to the impeller's plane is pointed towards the test mass symmetry axis. a) Representation of the test mass side view, with the coordinate system. Note that the axis in which the impellers' centers are found is parallel to the test mass symmetry axis (z axis). These two are lines separated by a distance x_0. b) The axis in which the we put the impellers' centers is parallel to the test mass symmetry axis (z axis), and these two are separated by a distance x_0.

SOURCE: From the authors.

Density (ASD) of the displacement in units of m/$\sqrt{\text{Hz}}$. Finally, it is compared to LIGO Voyager and Cosmic Explorer designed curves for ASD of displacement.

We assumed that all impellers are in phase and have the same rotational frequency f, which is the worst case for producing Newtonian noise. Nevertheless, an even number of impeller blades should, in principle, minimize the noise due to the blades arrangement symmetry. The effect of each impeller blade on the test mass is roughly canceled out by the effect of its pair, in the diametrically opposite side. This cancellation is not perfect, because the distances to the test mass, considering opposite blades in the same impeller, are not exactly the same.

It is important to note that LIGO Voyager and Cosmic Explorer do not have the same test mass design. LIGO Voyager uses a length of $l_v = 550$ mm and diameter $d_v = 450$ mm (LIGO SCIENTIFIC COLLABORATION, 2021). In the case of the Cosmic Explorer, because the dimensions of its test mass have not yet been fully defined, we used two sets of parameters (length and diameter): one is $l_c = 644$ mm and $d_c = 526$ mm, the other is $l_c = 800$ mm and $d_c = 450$ mm. For our results, we considered $x_0 \geq 1.0$ m, an impeller mass of $m = 100$ g, and an impeller radius of $\delta = 8$ cm.

Table 9.1 - Maxima of the ASD of displacement Newtonian noise values calculated for LIGO Voyager and Cosmic Explorer (CE), using $l_c = 644$ mm and $d_c = 526$ mm, with the ratio between Voyager and CE results.

x_0 (m)	n_p	n_b	f_0 (Hz)	Voyager ASD (m/$\sqrt{\mathrm{Hz}}$)	CE ASD (m/$\sqrt{\mathrm{Hz}}$)	Ratio
1	2	3	10	$4.141 \cdot 10^{-20}$	$4.360 \cdot 10^{-20}$	0.950
1	2	3	20	$1.035 \cdot 10^{-20}$	$1.090 \cdot 10^{-20}$	0.950
1	2	3	60	$1.150 \cdot 10^{-21}$	$1.211 \cdot 10^{-21}$	0.950
1	2	5	10	$1.874 \cdot 10^{-23}$	$2.486 \cdot 10^{-23}$	0.754
1	2	5	20	$4.685 \cdot 10^{-24}$	$6.214 \cdot 10^{-24}$	0.754
1	2	5	60	$5.206 \cdot 10^{-25}$	$6.905 \cdot 10^{-25}$	0.754
2	2	3	10	$5.073 \cdot 10^{-22}$	$6.141 \cdot 10^{-22}$	0.826
2	2	3	20	$1.268 \cdot 10^{-22}$	$1.535 \cdot 10^{-22}$	0.826
2	2	3	60	$1.409 \cdot 10^{-23}$	$1.706 \cdot 10^{-23}$	0.826
2	2	5	10	$1.492 \cdot 10^{-26}$	$2.346 \cdot 10^{-26}$	0.636
2	2	5	20	$3.730 \cdot 10^{-27}$	$5.865 \cdot 10^{-27}$	0.636
2	2	5	60	$4.145 \cdot 10^{-28}$	$6.517 \cdot 10^{-28}$	0.636
3	2	3	10	$3.213 \cdot 10^{-23}$	$3.978 \cdot 10^{-23}$	0.808
3	2	3	20	$8.032 \cdot 10^{-24}$	$9.945 \cdot 10^{-24}$	0.808
3	2	3	60	$8.925 \cdot 10^{-25}$	$1.105 \cdot 10^{-24}$	0.808
3	2	5	10	$1.832 \cdot 10^{-28}$	$2.923 \cdot 10^{-28}$	0.627
3	2	5	20	$4.581 \cdot 10^{-29}$	$7.308 \cdot 10^{-29}$	0.627
3	2	5	60	$5.090 \cdot 10^{-30}$	$8.120 \cdot 10^{-30}$	0.627

SOURCE: From the authors.

9.2 Analysis for different configurations

In order to compare the different results for distinct configurations, once can first consider $n_\mathrm{p} = 2$. Table 9.1 shows the comparison between the Newtonian noise calculated for impellers of 3 and 5 blades for all studied configurations. As it is expected, the larger the distance x_0, the less the noise level. In addition, the noise introduced by impellers of $n_\mathrm{b} = 5$ is lower than the one caused by impellers of $n_\mathrm{b} = 3$. This is also true for $n_\mathrm{b} = 7$, presenting noise below 10^{-23} for all frequencies and distances calculates. This is because adding more blades means a less anisotropic distribution of mass and, consequently, a large number of blades implies less Newtonian noise.

Also in Table 9.1, we compare the maxima noise values calculated. One can note that the ratio between Voyager and CE is dependent on the distance x_0 and the number of blades n_b, which means 3-bladed impellers generate more noise.

For LIGO Voyager case, 3-bladed noise can be 10^5 more intense than the 5-bladed

Figure 9.2 - Newtonian noise peaks for LIGO Voyagr test mass configuration.

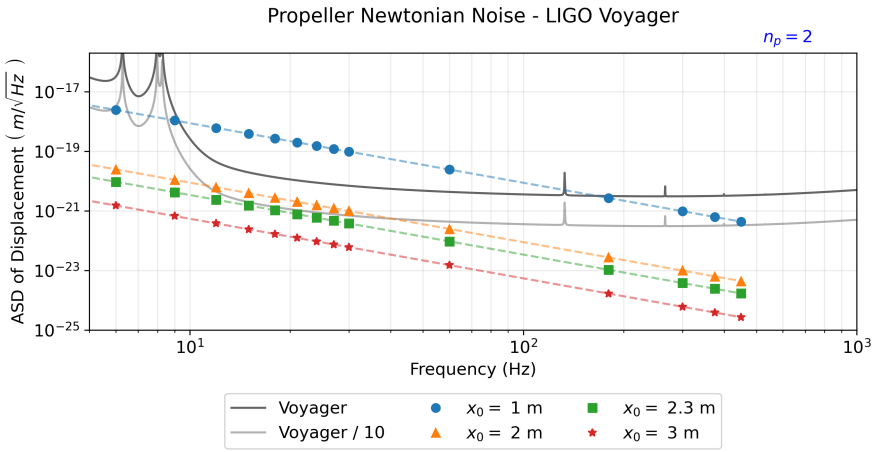

Newtonian noise peaks for different impeller rotation frequencies in the LIGO Voyager configuration.

SOURCE: From the authors.

one, depending on the distance x_0. On the other hand, as seen in Table 9.1, Cosmic Explorer presents similar ratios for noise peaks, ranging from 10^3 to 10^5 depending on x_0. For $x_0 \geq 2$ m, the peaks of 5-blade calculations are very low, below approximately 10^{-25} m/$\sqrt{\text{Hz}}$.

Finally, focusing on the frequencies, it can be noted that different impeller rotation frequencies f_0 will result in a peak noise at $f_n = f_0 \cdot n_\text{p}$. Assuming that the noise frequency is stable, we highlight that it is possible to use a notch filter to attenuate it. In the same way, one can design its frequency to match the power line noise or one of the wire suspension lines, since they are usually removed from the spectra. If the noise coupling is linear and not affected by other coupling mechanisms, it is also possible to try to cancel it, since the value is well known.

9.3 Minimum distance to noise level below sensitivity curve

For design choices, it is important to determine a safe distance for the impellers, i. e., z_0, that one can choose in order to have the impellers' noise level bellow the sensitivity curve. We defined a maximum threshold as 1/10 of the detector's sensitivity curve. Figures 9.2, 9.3, and 9.4 shows the sensitivity curve for Voyager, CE1 and CE2, respectively with noise maxima values.

For these noise peaks, it was used different frequencies f_0, ranging from 1 to 100, and

Figure 9.3 - Newtonian noise peaks for Cosmic Explorer 1st test mass configuration.

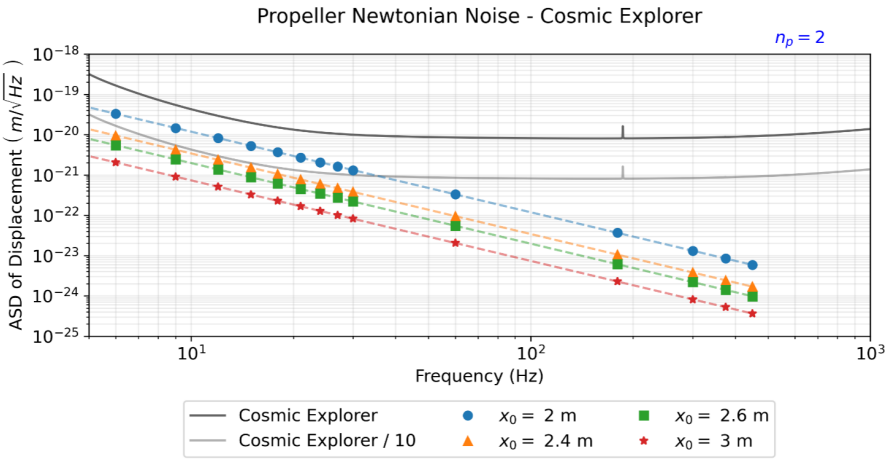

Newtonian noise peaks for different impeller rotation frequencies in the Cosmic Explorer configuration, using $l_c = 644$ mm, $d_c = 526$ mm.

SOURCE: From the authors.

some distances x_0 to find where all peaks were lower than the threshold. Additionally, it was considered $n_\mathrm{b} = 3$, since the noise produced by this impeller design is higher.

For LIGO Voyager configuration, our model shows that the noise peaks will lie below threshold if $x_0 \geq 2.3$ m (Figure 9.2). Cosmic Explorer results were also calculated and the first test mass dimensions ($l_c = 644$ mm and $d_c = 526$ mm), all noise peaks are below threshold if $x_0 \geq 2.4$ m (Figure 9.3).

For the second Cosmic Explorer test mass dimensions ($l_c = 800$ mm and $d_c = 450$ mm), all noise maxima are smaller than the chosen threshold if $x_0 \geq 2.6$ m (Figure 9.4). In addition, if $x_0 \geq 3$ m the noise peaks will lie below threshold for all three configuration. Impellers at distances $x_0 \geq 1$ m produce noise peaks below the threshold for analyzed designs if $n_\mathrm{b} = 5$. These results are summarized in Table 9.2.

The impellers are responsible for generating flux pushing the liquid forward within the pipeline. Particularly, the impeller's rotation creates a lower pressure region is created behind each blade. Depending on its angular velocity and the flux rate, the liquid Nitrogen boiling point can be lowered enough to form some bubbles. Possibly, they can merge into a one big bubble, attached behind each blade. These attached bubbles will reduce the Newtonian noise caused by the impellers. However, this possibility needs more investigation.

Figure 9.4 - Newtonian noise peaks for Cosmic Explorer 2nd test mass configuration.

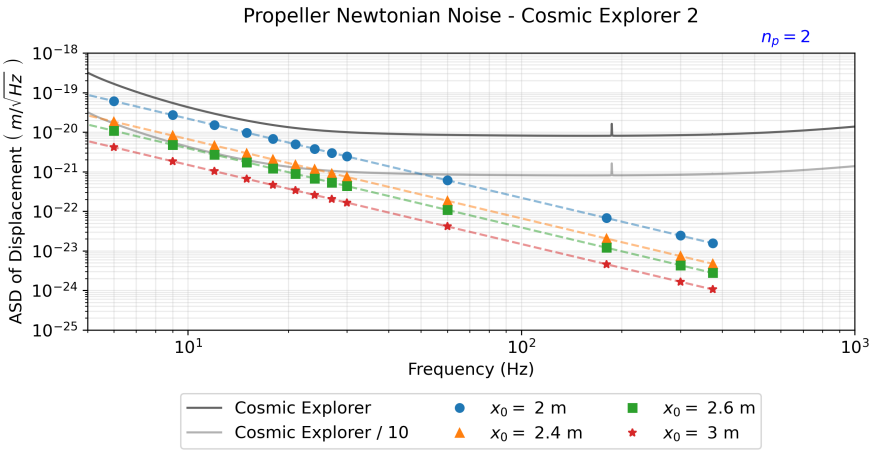

Newtonian noise peaks for different impeller rotation frequencies in the Cosmic Explorer configuration, using $l_c = 800$ mm, $d_c = 450$ mm.

SOURCE: From the authors.

Table 9.2 - Minimum x_0 (m) in which all peaks are below the sensitivity curve calculated for LIGO Voyager and Cosmic Explorer.

Detector	l (mm)	d (mm)	n_b	x_0 (m)
LIGO Voyager	550	450	3	2.3
			5	1.0
Cosmic Explorer	644	526	3	2.4
			5	1.0
Cosmic Explorer	800	450	3	2.6
			5	1.0

SOURCE: From the authors.

9.4 Newtonian Noise zero

The impeller's centers are located at the points $(x_0, 0, z)$. Varying the z coordinate, it is possible to calculate the noise peak for different impellers' center positions. This sweep search showed a zero noise for a specific θ_0 angle, which implies a specific z coordinate, depending on the number of blades n_b. Note that θ_0 is the angle formed by the vector pointing from the origin to the impeller's center and the z axis.

On Figure 9.5, one can see the plot for the ASD of displacement calculated for one

impeller with 3 blades, $x_0 = 1$ m, and $f = 20$ Hz. Varying the z coordinate, the model resulted in a zero value around $z \approx 0.8918$ m.

The cancellation of the Newtonian noise can be understood by expanding Equation 9.1 to first relevant order in (δ/r_0), where δ is the impeller radius, and r_0 is the distance between the center of the impeller and the center of the test mass. As shown by Reis et al. (2025), if one expand the monopole term for the axial acceleration for n_b blades, the lowest order α_0 is given by:

$$\alpha_0 = \frac{G}{r_0^2}\left(\frac{\cos(\theta_0)}{2}\right)^{n_\mathrm{b}-1}\frac{(2n_\mathrm{b}+1)!!}{(n_\mathrm{b}-1)!}\left[\cos^2(\theta_0) - \frac{n_\mathrm{b}}{2n_\mathrm{b}+1}\right]\left(\frac{\delta}{r_0}\right)^{n_\mathrm{b}}\cos(n_\mathrm{b}\beta(t)), \quad (9.2)$$

where θ_0 is the azimuth angle of the center of the impeller, and $\beta(t)$ represents the time-dependent angular motion of the impeller. Therefore, the monopole contribution to impeller Newtonian noise from this equation becomes zero at:

$$\theta_0 \;=\; \arccos\left[\left(\frac{n_\mathrm{b}}{2n_\mathrm{b}+1}\right)^{1/2}\right]. \quad (9.3)$$

Equation 9.3 gives an approximation for the z coordinate at the zero Newtonian noise. For $n_\mathrm{b} = 3$, as shown in Figure 9.5, then $\theta_0 \approx 49.1^\mathrm{o}$, which leads to $z \approx 0.8660$.

In this model, as each blade rotates, two geometric quantities vary periodically: its distance to the test mass and the azimuthal angle relative to the cylinder's symmetry axis. Although these variations are small, they produce an oscillatory component in the axial gravitational force on the test mass.

When these two effects are combined, the resulting axial acceleration from a single blade consists of a constant background term plus a small sinusoidal fluctuation at the impeller's rotation frequency. Summing over all blades of a single impeller, most of the first-order oscillations cancel each other, leaving only harmonics at an integer multiple of the rotation rate (REIS et al., 2025).

The Newtonian noise zero found is explained by analyzing how the gravitational force generated by the blade varies during its rotation. At an specific angle θ, the influences of distance variations and projection onto symmetry axis exactly balance, driving to a null amplitude of the oscillatory component. In other words, although

each blade still exerts a non-zero gravitational force, their combined, time-varying contribution do not changes with time.

Since experimentally confirmed, one can chose a impeller's z position as defined so that the blades ideally never introduce a varying gravitational force in the system, therefore mitigating (or, at least, reducing significantly) the impellers' Newtonian noise particular noise without moving the impeller arbitrarily far away.

9.5 Considerations about the Newtonian noise model

The presented model revealed a possibility for the impeller's position choice: the combination of blades position and angle produces a noise zero for specific positions in our coordinate system. In addition, there is a region around the zero-noise position which results in lower levels and can be used to allocate more than one impeller, if needed.

This result implies that in a realistic design for the cryogenic system, we can select the impeller position and orientation so as to minimize the impact of their Newtonian coupling to the test mass.

Figure 9.5 - Newtonian noise calculations for different z-coordinates.

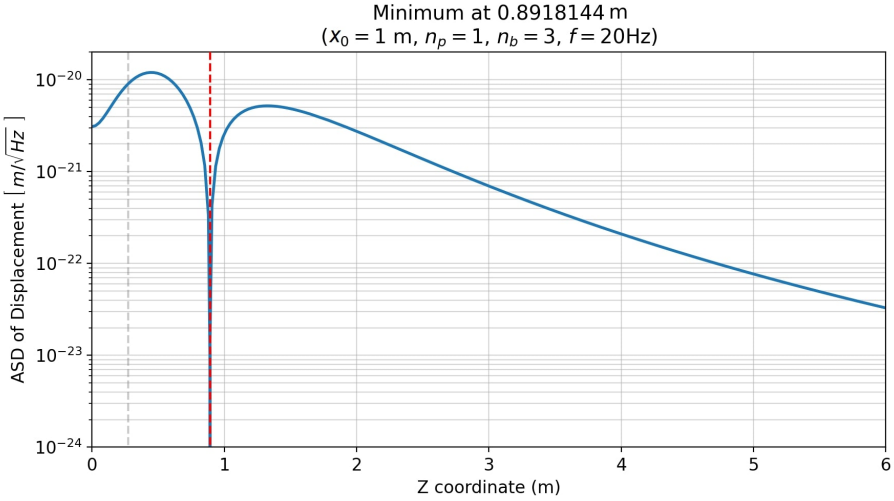

Noise peaks for different z coordinates, using the Voyager test masses design, $x_0 = 1.0$ m, $n_{\mathrm{p}} = 3$, and $f = 20$ Hz. The null Newtonian noise is located at $z \approx 0.8918$ m. The red dashed line marks the z value in which we have zero noise, while the gray dashed line represents the test mass half-length. This profile is the same for negative z coordinates.

SOURCE: From the authors.

In addition, by ensuring that the distance criterion presented in Table 9.2 is met, the formation of bubbles on the pipeline walls (BONILLA et al., 2021) becomes a greater concern than impeller Newtonian noise for LIGO Voyager and Cosmic Explorer.

However, this model has its limitations. It treats the blades as point masses, but it can be improved by representing each blade as several equal-mass points and calculating their contributions to the total axial acceleration. Moreover, the Newtonian noise results for the case of the Cosmic Explorer need to be reviewed if its test masses are produced with other dimensions than the ones we assumed in this work.

9.6 Chapter summary

This chapter presented studies concerning the Newtonian noise generated by impellers used in a closed-loop pipeline cooling-down system for cryogenic detectors. For this purpose, a model was developed for estimation of the gravitational interaction between the impeller and the test mass. The model was then applied to the LIGO Voyager and Cosmic Explorer test masses. From its results, the study can contribute for some design choices.

The minimum distance x_0 in which the Newtonian noise is lower than 1/10 the sensitivity curve will depend on the number of blades, n_b. The results for $n_\mathrm{b} = 3$ are, in LIGO Voyager case, $x_0 \geq 2.3$ m. For Cosmic Explorer, we analyzed two different test mass possibilities and, for the minimum distance x_0 can be 2.4m or 2.6m. However, considering $n_\mathrm{b} = 5$, the peaks are below the threshold if $x_0 \geq 1.0$m for all considered detectors designs. In addition, it was found a region of low noise, which can be used to allocate impellers while mitigating Newtonian noise coupling.

Next chapter will focus on work done in LIGO Livingston Observatory during the PrInt scholarship.

10 ACTIVITIES AT LIGO LIVINGSTON OBSERVATORY

This Chapter outlines the research activities and scientific contributions carried out by the student from March to August 2023, while working at the Laser Interferometer Gravitational-Wave Observatory in Livingston, Louisiana, United States. This was possible due to a CAPES PrInt Scholarship and the LIGO Fellows program of LIGO Livingston Observatory (LLO).

The student was engaged in the research, installation, maintenance, and calibration of several environmental monitoring instruments, especially accelerometers and magnetometers. Auxiliary channels (as these instruments are known) were tested and replaced, and new sensors were also installed. In addition, it was possible to contribute to detector's noise mitigation and magnetic coupling functions calculations for O4b.

10.1 LIGO Fellows program

The student participate in academic and experimental activities at the Laser Interferometer Gravitational-Wave Observatory in Livingston (LLO), LA, United States, from 01/03/2023 to 31/08/2023, under the project number 88887.717392/2022-00. All research at the facility was done under the supervision of Dr. Brian O'Reilly, but collaborating more closelly to Dr. Anamaria Effler, head of the Physical Environment Monitor (PEM) group in LLO.

10.1.1 Physical and environmental noise

The environment surrounding the gravitational wave detector can influence the precise measurement of the differential arm length (DARM) in the interferometers. These external environmental disturbances can couple into the interferometer readout and significantly reduce detector's sensitivity. In addition, it can also introduce transient non-astrophysical signals.

These disturbances, known as **environmental noise**, can be generated by physical contact mechanisms, such as vibrations, or temperature fluctuations, electromagnetic waves, static electric and magnetic fields, and high-energy radiation.

The Physical Environmental Monitoring (PEM) group is responsible to monitor and characterize these noise sources and how they couple into DARM. This work is done through a network of different sensors distributed across the observatories. LIGO sites contain several monitoring channels, as accelerometers, magnetometers,

Figure 10.1 - LLO map marking PEM sensors.

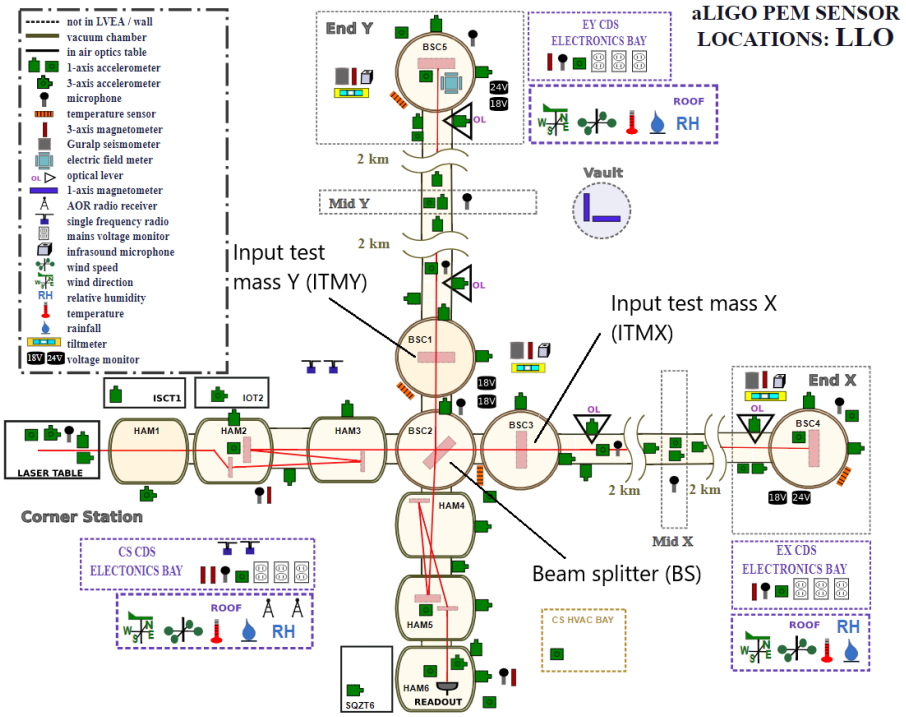

The Physical Environmental Monitoring system layout at the LIGO Livingston detector during O3b. The laser beam is shown as a red line; core optics, as the test masses, are shown as rectangles inside the vacuum chambers.

SOURCE: Nguyen et al. (2021).

current clamps, microphones, thermometers, etc. Figure 10.1 shows LLO site with PEM channels during O3b. New sensors are also installed in order to complement the current network, as the accelerometer installed at the LLO Corner Station (SC) shown in Figure 10.2

Studying environmental noise is important in searches of unmodeled gravitational waves sources, because these searches are based on excess power without using waveform templates. An event candidate like this could be generated by environmental noise, but monitoring them by PEM channels can help to distinguish between astrophysical and non-astrophysical signals.

In addition, monitoring PEM channels is used to improve detector's sensitivity through reducing contamination by environmental noise. It is common to track down troublesome noise sources and coupling mechanisms in order to remove them, isolate from the detector, or reduce coupling by modifications in the detector.

Figure 10.2 - Installed accelerometer installed at the LLO Corner Station.

One of five accelerometers installed by the student at LLO Corner Station. There were all cabled at the same workday and, in the next, connected to Data Aquisition. See aLOG 64180.

SOURCE: From the authors.

10.1.2 PEM coupling functions for LIGO sites

In order to quantify how much LIGO detectors are influenced by environmental disturbances while operating, the PEM group performs controlled injections that intentionally induce measurable responses in DARM channel. Acoustic injections are made using speakers, and the "witness" channels are accelerometers and microphones. Seismic injections are produced using mechanical shakers, which effects are monitored by accelerometers and seismometers. Magnetic injections are performed using wire coils, and their effects are detected by magnetometers across the facility.

Before discussing the done work, it is necessary to introduce the concept of coupling function and coupling factors.

Consider a noise injection performed at the coupling site, where the witness sensor is located, and this injection produces a signal in this sensor as a response in DARM as well. The coupling function for this environmental noise is given by the collection of coupling factors for each DARM frequency bin. This last represents the relation between the sensor signal and the DARM response, determined by comparing the amplitude spectral densities (ASDs) of both channels during injection and background (quiet/no-injection) times. Therefore, the coupling function CF(f) is

calculated as (NGUYEN et al., 2021):

$$\mathrm{CF}(f) = \sqrt{\frac{[Y_{\mathrm{inj}}(f)]^2 - [Y_{\mathrm{bkg}}(f)]^2}{[X_{\mathrm{inj}}(f)]^2 - [X_{\mathrm{bkg}}(f)]^2}} \tag{10.1}$$

where $X_{\mathrm{inj}}(f)$ and $X_{\mathrm{bkg}}(f)$ are the ASDs of the witness sensor during injection and background times, respectively. On the other hand, $Y_{\mathrm{inj}}(f)$ and $Y_{\mathrm{bkg}}(f)$ are the ASDs of DARM for injection and background times, respectively.

The coupling factor is used to quantify ambient contribution of noise in DARM spectrum. This can be done by multiplying sensor's background level and the coupling function. Similarly, it is possible to compute the contributions of a transient noise in DARM when validating a gravitational wave signal.

Nevertheless, LIGO facilities have many witness channels used to monitor environment noise. With multiple coupling sites, each one with a dedicated witness sensor, the DARM response to various injections can be modeled as a linear combination of the sensor signals weighted by their respective coupling functions. Multiple independent injections can be performed in order to determine coupling functions of all witness sensors involved.

However, a perfect sensor placement at the exact coupling site is an ideal scenario. The coupling sites are often unknown and probably are distributed throughout the detector facility. Therefore, the coupling functions derived from this method represent estimates for environmental noise. Nevertheless, reliable coupling factors can be calculated if the sensors are distributed to cover the most probable coupling sites as much as possible.

It is impractical to inject signals at each sensor. Therefore, given a channel, its coupling function is composed by the coupling factors calculated using the nearest injection, i. e., determined by the highest sensor amplitude. In other words, PEM group produces a set of injections near the sensors and, from each of them, computes the single-injection coupling function. The final **composite coupling function** is formed taking the coupling factor corresponding to the highest sensor's signal amplitude for a given frequency.

This approach requires that the injection signal be significantly stronger than the background noise, both in the sensor and in DARM. In general, a reliably measurement is determined by thresholds, typically defined as a ratio of injection ASD

to background ASD. If an injection exceeds the sensor and DARM thresholds, the coupling factor is calculates as a **measurement** by Equation 10.1 at a specific frequency bin. However, if there is a signal in sensor exceeding the threshold, but not the DARM one, the coupling factor is calculated omitting the background term, resulting in an **upper limit**, as follows:

$$\mathrm{CF}_{\text{Upper Limit}} = \frac{Y_{\mathrm{bkg}}(f)}{\sqrt{[X_{\mathrm{inj}}(f)]^2 - [X_{\mathrm{bkg}}(f)]^2}} \,. \tag{10.2}$$

It is important to note that, in order to define measurements, the injected signals are intense enough to produce a response in DARM. However, the injection amplitudes are limited by the sensitive range of the witness channels. If saturated, a sensor will overestimate the coupling factor. Consequently, this limits the number of possible measured coupling factors calculated by this method.

10.1.3 Magnetic injection in LLO

In order to produce magnetic coupling functions for LLO, many magnetic signals were injected around the site. On total, twelve magnetic injections were performed in different locations, as shown by Figure 10.3.

There were two types of magnetic field injections: combs and broadbands. Comb injections were made by small coils, in frequencies multiple of 7.1 Hz, 14.2 Hz and 49.7 Hz. Therefore, there was three comb magnetic injection by location. They were combined according to sensor intensity. For a given sensor, the 7.1 Hz field is stronger in sensor than others for frequencies up to 100 Hz by design. From 100 Hz to 200 Hz, 14.2 Hz comb injection are the stronger injection in sensor's spectrum. Finally, for frequencies greater than 200 Hz, the 49.7 Hz comb injection intensity dominates in sensors. Joining all of them according to its frequency range of higher intensity leads to the "final" magnetic comb injection.

The other injection type is called broadband injection, done by large coils fixed on the facilities walls. These were subdivided in a few ranges: 10 Hz to 40 Hz, 40 Hz to 100 Hz, 100 Hz to 200 Hz, 200 Hz to 1000 Hz, and 1000 Hz to 4000 Hz. Similarly to comb injections, the broadband ones are combined to result in one final injected signal according to the strongest amplitude in sensor. Figure 10.4 illustrates a broadband injection done in LVEA and the response in DARM.

The magnetic field injections effected all magnetometers and all stations in order

Figure 10.3 - Performed magnetic injections for LLO coupling function.

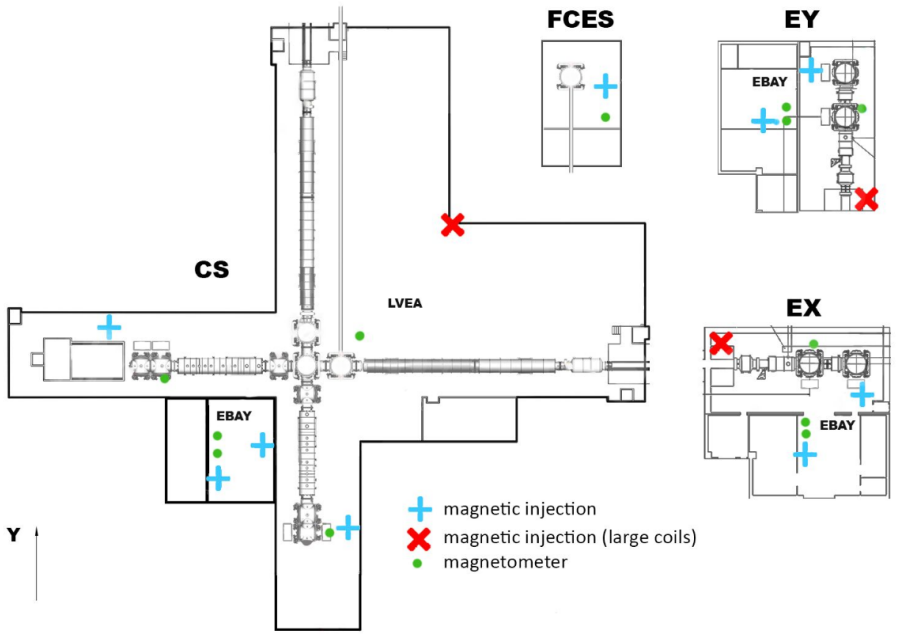

Map representing LLO site with all injection locations: in CS, the LVEA and EBAY rooms, FCES, EY and EX. Magnetic injections made with large coils are represented by red cosses. The ones made using a small coils is marked by blue plus signs. Magnetometers are marked by green dots.

SOURCE: Adapted from Nguyen et al. (2021).

to cover all possible coupling sites. In order to calculate coupling function for each sensor and estimate ambient noise, it was necessary to combine all injections data into one single "resulting" one. This was done choosing the highest sensor signal by channel.

The tests were performed across all stations and were observed in all respective magnetometers. This was done in order to ensure a coverage of every potential coupling sites. In order to calculate coupling function for each sensor and to estimate the corresponding ambient noise contribution to DARM, it was necessary to combine the data from all injections into a single representative dataset. This was done by selecting, for each channel, the injection instance that resulted in the maximum sensor response.

The data produced was used to calculate the coupling factors for each sensor, as described in the next subsection.

Figure 10.4 - Magnetic Injection signal in a LVEA magnetometer and the DARM response.

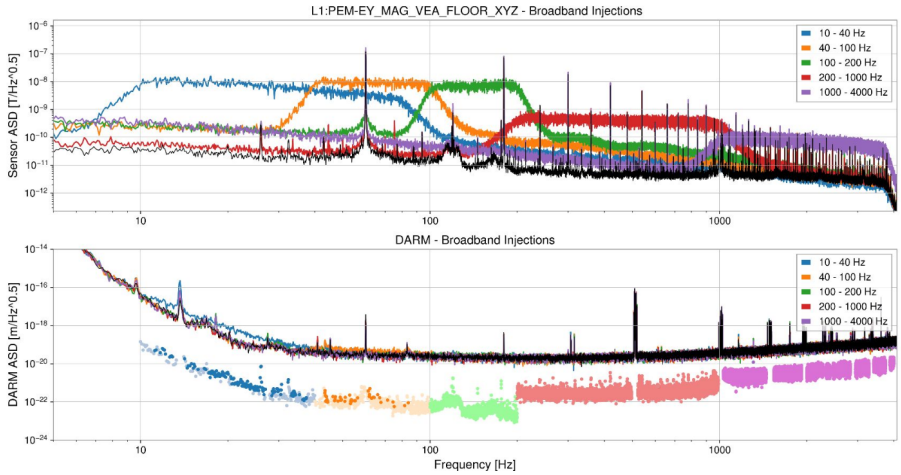

The first plot shows the different broadband injections according to the described ranges in a magnetometer in the LVEA floor. The response in DARM are also shown in the second plot. Estimated ambient noise bases on calculated coupling factors are shown as dots.

SOURCE: From the authors.

10.1.4 Magnetic coupling functions for O4b

Using data from the magnetic injections, it was possible to compute coupling factors for magnetic fields at each magnetometer located at LLO. From it, magnetometer coupling functions were generated.

Previously, the coupling factors were calculated using a LIGO Collaboration package called PEM Coupling Function Tools (NGUYEN, 2018). However, the outputs often presented spurious coupling factors incorrectly labeled as measurements rather than upper limits. This issue arose from random variability in data. For some frequency bin, the DARM background level was lower than usual while DARM data during injection happened to be higher. As result, the analysis mistakenly interpreted this as a true response to injected magnetic field and calculated the coupling factor as a measurement. Consequently, many coupling factors were inaccurately computed and misclassified.

To solve this issue, the student developed a new script based on the orginal package, specifically designed to avoid such spurious results. The solution involved using a smoothed DARM background, which presents reduced variability. The ratios between the injected response, Y_{inj}, and the background Y_{bkg} was then recalculated

and compared with the predefined threshold. This either confirmed a measurement or reclassified it as an upper limit, using the appropriate expression in each case.

Once with the corrected coupling functions, it was possible to estimate the magnetic field contribution to DARM, the estimated (magnetic) ambient noise. This is the result of multiplying coupling factors by injection-free sensor levels, i. e., the coupling factors and the sensor background during quiet time.

Every station have multiple magnetometers at different locations. All data were combined choosing the highest sensor response to injection at each frequency bin. Similarly, it was possible to produce coupling functions and estimated ambient noise for each individual station — namely the Corner Station, End-X Station, End-Y Station, and the Filter Cavity End Station — as well as sitewide plots, enabling a comprehensive assessment of magnetic field coupling across the entire observatory. Each function includes labels indicating whether data represent measured values or upper limits, along with the corresponding station and channel name. Figure 10.5 shows the final sitewide plot for magnetic estimated ambient noise.

The files with all results, as well as the plots were published on the LIGO PEM website (PEM, 2025). In addition, the magnetic injection methods and estimated ambient noise curves were presented to the LIGO Collaboration DetChar group.

10.1.5 83 Hz line hunt

In March 2023 (see aLOG 63964), it was reported an environment noise found at LLO with unknown causes. This noise consisted in a line at 83.15 Hz and a hill around it with no apparent periodicity. The LLO PEM group was looking for the noise source to mitigate it.

Initial analyses suggested a possible correlation with environmental sources near the Y-arm, particularly exhaust fans and dehumidifiers. In order to find the coupling site, and possibly the noise source, several acoustic injections were made, with the student's participation.

A sweep injection from 50 Hz to 100 Hz was performed to further evaluate frequency-specific coupling, trying to recreate the 83 Hz line in DARM. Therefore, it was used a speaker at the door before Y-End Station (ES) generating acoustic signal with sufficient intensity to cause a response in DARM, while not saturating accelerometers. This injection showed varying levels of response at different frequencies, with notable injected energy at 83.15 Hz. However, there was no considerable response in

Figure 10.5 - LIGO Livingston (L1) sitewide Estimated Magnetic Ambient Noise.

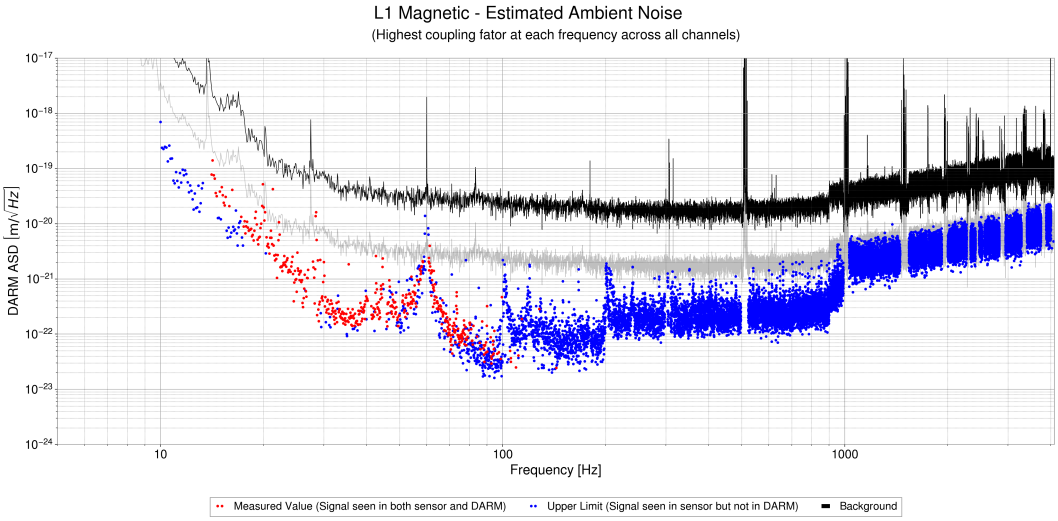

Magnetic ambient estimates are made by multiplying coupling factors and injection-free sensor levels. This plot represents the estimated noise for the Livingston observatory. Red circles indicate estimates from measured coupling factors, i.e. where the injection signal was seen in the sensor and in DARM. Blue circles represent upper limit coupling factors, i.e. where a signal was seen in the sensor but not in DARM. In black line, the DARM level and in faded gray, the DARM/10 level. This plot and others are available in the PEM O4b Sitewide Summary Plots webpage (PEM, 2025).

SOURCE: PEM (2025).

DARM, again casting doubt on a simple mechanical coupling scenario. Figure 10.6 part a) shows the sweep injection spectrograms.

However, it was found that the dehumidifier fan channels showed on/off transitions aligned with the noise, as seen in Figure 10.6 part b), although not presenting the hunted line. These observations suggested that the fan at the Y2J door was contributing with the excess noise around the 83 Hz line.

When comparing this sweep to the fan turning-on time spectrum, it was possible to conclude that although the injected energy into the accelerometers was much larger, it still failed to replicate the 83 Hz line feature in DARM. This comparison indicated that the coupling might not be mechanical, at least not at the sensor locations tested.

To further investigate the coupling mechanism, a series of acoustic injections were conducted along the Y-arm. The tests were done at five distinct arm locations: Y2J,

Figure 10.6 - Spectrograms to DARM and Y-arm accelerometers.

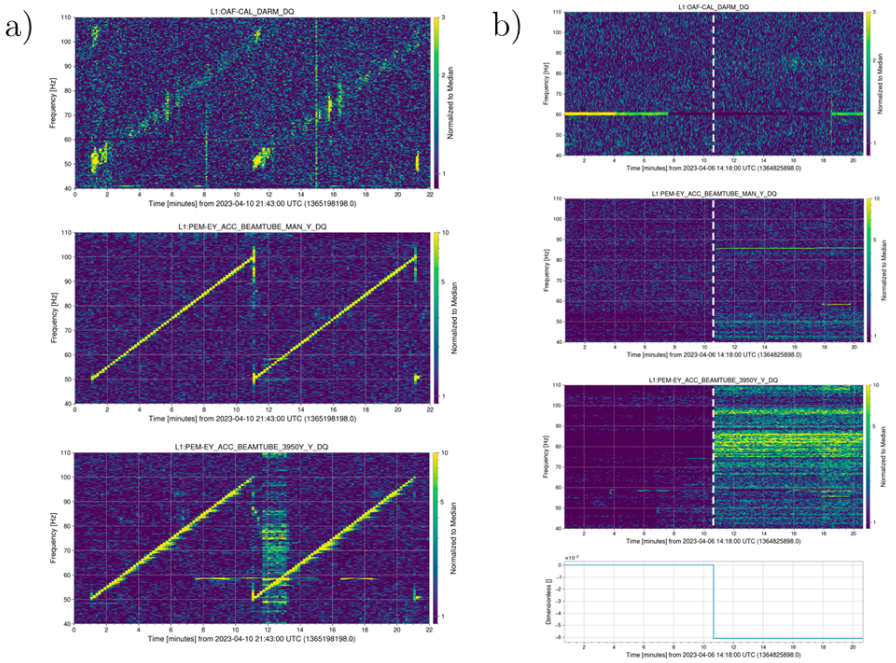

Spectrograms used to investigate the 83.15 Hz noise coupling site and source. Figure a) shows the sweep injection done in the end of the Y-arm. Plots, up to down, shows normalized spectrograms to DARM channel with no significant response at 83.15 Hz, the accelerometer at the Y-Manifold, and the nearest accelerometer to Y-End Station which is fixed at the laser beamtube. Figure b) shows normalized spectrograms for the same channels. In addition, it shows the time when the dehumidifier fan at Y2J door is on. This time was marked by a white dashed line. In this case, we can see a coupling in DARM, but no line at 83 Hz. See aLOG 64360.

SOURCE: From the authors.

Y2A, the Y-Midstation (Y-Mid), Y1J, and Y1A. We injected acoustic signals ranging from 60 Hz to 100 Hz. Data was collected from eight accelerometers distributed along the Y-arm and from the DARM channel. Figure 10.7 shows a representative map of the injections locations and the accelerometers.

While injecting significantly more than the dehumidifier fan, it was not possible to excite the 83 Hz with the conducted acoustic injections, besides all sensors available were effected by the injected signal. These results suggest that vibrational coupling through air or structure is unlikely at the locations monitored, although it remains possible that the actual coupling point is unmonitored.

Magnetometers and current clamp data were also examined during known fan on/off transition times. Spectrograms showed some magnetometer channels with persistent

Figure 10.7 - Acoustic injection locations in Y-arm.

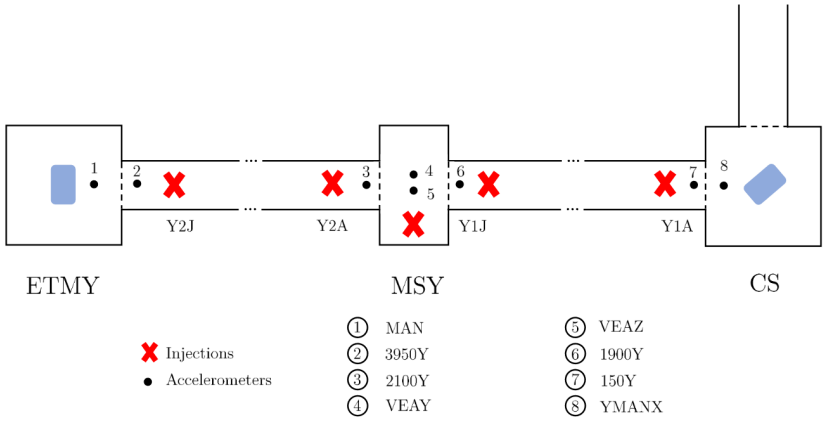

Schematic map showing acoustic injection locations, marked by red crosses, and the witness accelerometers, marked by black dots. See aLOG 64278.

SOURCE: From the authors.

lines near 85 Hz (see aLOG 64368). However, these lines were present both before and after Y2J fan started operation, suggesting they were not be caused directly by the them.

Investigators, however, found that the excess noise was not related with the 83.15 Hz peak. That was proved analyzing times when the dehumidifier fan was on (blue curve) or off (orange curve), but in both cases there was no noise line. As shown in Figure 10.8, the noise line, in black, just showed up coincidentally when an injection was being conducted. Consequently, it was concluded that the Y2J fan was responsible for some noise in DARM, but it was unrelated to the 83 Hz line.

The fan noise was solved with improvements in fan damping, since it was attached on Y2J door. Finally, the 83 Hz line source was found as a Residual Gas Analyzer (RGA) fan at X mid. When physically isolated, the line disappeared from DARM (see aLOG 65264).

10.2 Rapid Response Team and Data Quality Shifts

The Rapid Response Team (RRT) is a group in LIGO Collaboration responsible to provide human vetting to decide whether to confirm or retract all significant candidates during an observing run. When a high-significance candidate is detected, as a

Figure 10.8 - DARM data for times when Y2J dehumidifier fan was on and off.

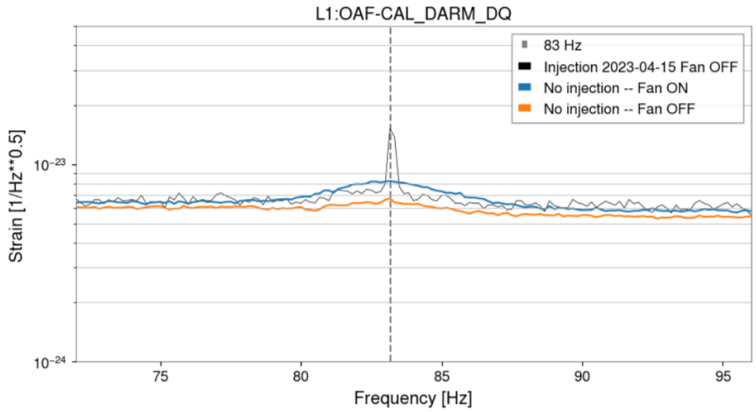

DARM strain spectrum around 83 Hz. In blue, DARM data for time when the fan was on and there was no injection. Orange curve shows data for a time when the fan was off and no injections were being conducted. The difference between these two emphasizes the fan noise in the gravitational wave channel. However, there is no 83 Hz line, an evidence that these were unrelated noise sources. Coincidentally, the 83 Hz line was present during an acoustic injection in Y2J door, when dehumidifier fan was turned off. See aLOG 65264.

SOURCE: From the authors.

signal with possibly electromagnetic counterpart, a team of scientist is gathered to discuss its assessment for each event. Then, an Initial Circular or Retraction Notice will be issued with an accompanying GCN Circular. There is no rapid response for low-significance candidates.

RRT is a group formed by non-expert members, in-site experts working in detectors' control rooms, and experts from different areas as detector characterization, pipelines analysis, public alert pipeline, calibration, parameter estimation, and others.

The student attended the RRT as a Responder Level 0 in the first half of the fourth observational run (O4a). As such, he was tasked with being the first person to respond to signals of interest and contributing whether the Collaboration should notify the broader community that it has been detected an high-significance signal. This allows electromagnetic telescopes to perform follow-up observations and to attempt to find a source for the gravitational wave emission in the electromagnetic counterpart.

Being daily present at the observatory provided the student the opportunity to assist

scientists working in Data Quality (DQ). In this talks, it was needed to meet with collaborators who evaluating the quality of LLO. Therefore, the student's major role primarily involved reporting any observatory activities that could impact the data quality during the week. For instance, during periods of unusually high seismic noise in the anthropogenic band, often caused by heavy logging activities near the site, the student reported these events regularly to the Data Quality team. These reports helped to explain sudden LLO lock-downs.

10.3 Presented works

In March 2023, the student attended in person to the LVK Meeting, held in Chicago, USA. There it was possible to presented a poster (REIS; AGUIAR, 2023) on the work regarding the preliminary results of Newtonian noise introduced by impellers into the LIGO Voyager test masses.

The student was also the organizer and chair of a bi-weekly meeting at the LIGO Livingston Observatory. These were opportunities for participants of offering an audience for scientists, students, and visitors to present and discuss their ongoing work. The last meeting organized was his LSC Fellows Talk, which aimed to present all work developed since March until August 2023. LLO scientists and the Louisiana State University (LSU) group members attended to this final presentation.

Finally, the magnetic coupling function for LLO was presented during the LIGO DetChar Teleconference, to all scientists who work with Detector Characterization (DetChar) and may have interest in the results.

10.4 Chapter summary

This Chapter was dedicated to the activities conducted at the LIGO Livingston Observatory (LLO) during the author's participation in the LIGO Fellows Program. The work focused on investigations into physical and environmental noise, from searching environment noise sources to producing magnetic injections and calculating coupling functions. A significant portion of the work addressed the computation of magnetic coupling functions, more precisely calculating estimated magnetic ambient noise for the O4b observing run. This involved improving existing tools by implementing an analysis to better distinguish true detector responses from statistical fluctuations. The Chapter also presented the investigation of a persistent 83 Hz noise line in DARM and a excess noise around it. Through extensive analysis and acoustic injection tests, it was proven that the excess noise was linked to specific

dehumidifier fan in the Y-arm. The line was generated by an RGA in the Mid-X Station. Both were mitigated. In addition to technical contributions, the author also participated in the Rapid Response Team and helped Data Quality shifters during their turn, gaining experience in real-time detector characterization and contributing to LIGO's operational efforts.

11 CONCLUSIONS

This thesis aimed to explore and contribute to the technological challenges of future ground-based interferometric gravitational wave detectors, particularly those involving cryogenic temperatures.

Since most future detectors designs consider the use of silicon test masses, the first part of this work was dedicated to investigate the emissivity of silicon at cryogenic temperatures, especially at 123 K. The experimental setup was built in order to measure the cooling-down curve of a Silicon specimen. From this data, one can derive the effective emissivity.

Thermocouple data presented large variations due to limitations in precision. Then, it was needed to apply different methods to estimate emissivity from the data. The major issue was found while estimating temperature derivative. Five methods were applied: numerical differentiation by finite difference, a smoothing filter in the last approach, the Savitzky-Golay filter, and two different curve fitting, a 10th-polynomial function fit and an exponential fit. From them, it was possible to estimate the temperature derivative and the emissivity using Equation 4.9.

Two different specimens were used. The first one was a cylinder with 15.24 cm of diameter and 2.45 cm thick, with a mirror coating face. Three experimental runs were conducted with this piece. Combining the five different results from each experimental run, the Silicon emissivity at 123 K from this specimen was estimated at $\epsilon = 0.627 \pm 0.007$.

The second specimen was an irregular shape piece of Silicon. It was specially challenging to estimate this specimen surface area, due to its complex shape and rough texture. Insufficient liquid Nitrogen supply limited the experimental runs to only one. Besides the overestimated surface area, issues related to thermocouple malfunction and a non-properly fixed added uncertainties to the final measurement. For the irregular specimen, the emissivity at 123 K was estimated at 0.561 ± 0.020.

A theoretical model considering Silicon at cryogenic temperatures as a semitransparent material was proposed in addition to the experimental results. This model depends on two key parameters: the mean thickness χ and the absorption coefficient α. The first is associated to the radiators dimensions, while the second contain information about the material's optical properties. From this model, Silicon effective emissivity at 123 K was calculated for the two specimens. The values were

then compared to the experimental results from this works, and also the emissivity estimated for a rectangular prism in Constancio et al. (2020).

The comparison highlighted the importance of implementing internal reflections into the scripts, since this feature has a significant influence on the final result. On the other hand, the experimental results were consistent with the theoretical estimations, which considered a semitransparent radiator model that incorporates geometry-dependent mean thickness and wavelength-dependent absorption coefficients.

The theoretical effective emissivity for LIGO Voyager, Cosmic Explorer and Einstein Telescope were calculated. Due to its large dimensions, Voyager and Cosmic Explorer emissivity resulted in $\epsilon_{\text{Voyager}} = \epsilon_{\text{CE}} = 0.685$. This is a promising result, since Voyager can radiate approximately 7.4 W of thermal power, and Cosmic Explorer around 12.5 W. These values can be higher if one considers lower shield temperatures, reaching 8.5 W for Voyager using 60 K shields.

This indicates that an emissivity of $\epsilon = 0.685$ is enough to maintain operating temperature at 123 K without using any high-emissivity back paint in the test mass barrel face. However, there could be an motivation to use the ink to lower the Silicon mechanical Q-factor and avoid issues involving parametric instabilities.

Impurities in the Silicon test mass substrate can absorb photons and heat the temperature. However, considering the emissivity results, there is a safety margin that allows for continued operation within acceptable limits, since it is expected that LIGO Voyager will absorb around 6.3 W of power from the laser.

Furthermore, it was possible to calculate an overestimated effective emissivity for Einstein Telescope, due to lack of information about Silicon extinction coefficient at 10 K. The result for Einstein Telescope at 50 K was $\epsilon_{\text{ET}} = 0.235$. The actual value is expected to be lower.

This work also accounted for the problem of maintaining test masses temperature. Considering the GWINPE proposal of creating a cold environment around test masses by a closed-loop pipeline, it was created a computational model to calculate the Newtonian noise generated by impellers responsible of generating the liquid Nitrogen flux. From the results, it was possible to shed some light on the design choices, such as LIGO Voyager.

It was showed that the generated Newtonian noise levels depend on the number of

blades and the distance to the test mass center. In order to calculate the minimum distance x_0, we considered a threshold of one order of magnitude lower than the sensitivity curve. Therefore, a 3-bladed impeller in LIGO Voyager can be placed at a distance of $x_0 \geq 2.3$ m. For Cosmic Explorer, two different test masses configurations were analyzed. The minimum distance x_0 can be 2.4 m or 2.6 m, depending of test mass dimensions.

However, considering 5-bladed impellers, the peaks are below 1/10 of the sensitivity curve if $x_0 \geq 1.0$ m for all considered detectors designs. A pair of impellers with 7 blades each also produce noise peaks bellow the threshold for all investigated distances and frequencies.

The impeller Newtonian noise model showed that, by the combination of blades position and angle, there is a minimum noise region with a zero for specific positions. Consequently, there is a zone around the zero-noise position that results in lower noise levels. This can be strategically used to allocate one or more propellers without introducing any levels of Newtonian noise.

Finally, it was reported the collaborative work developed at the LIGO Livingston Observatory. This includes the instrumental tasks within the LLO PEM Group, aimed at mitigating transient noise, performing acoustic and magnetic injections, producing magnetic coupling functions, and estimating magnetic ambient noise levels at the site. This were valuable experiences for the student.

Cryogenic ground-based gravitational wave interferometric detectors will allow humanity to observe plenty of signals from the Universe. This thesis aimed to contribute to the Gravitational Waves Astrophysics field dedicating studies on these kind of detectors. Future interferometers, with their unprecedented sensitivity, promise to expand our understanding of the Cosmos, revealing new insights into the Universe. Using this new temperature regime, it will be possible of capture even better the faint ripples of space-time and push the boundaries of human knowledge.

REFERENCES

AASI, J. et al. Advanced LIGO. **Classical and Quantum Gravity**, v. 32, n. 7, p. 0740045, 4 2015. ISSN 13616382. Available from: <https://iopscience.iop.org/article/10.1088/0264-9381/32/7/074001>. 23, 28, 30, 33

ABAC, A. G. et al. Observation of gravitational waves from the coalescence of a 2.5–4.5 $m_{\odot}$ compact object and a neutron star. **The Astrophysical Journal Letters**, v. 970, n. 2, p. L34, jul 2024. Available from: <https://dx.doi.org/10.3847/2041-8213/ad5beb>. 19

_____. GW231123: a binary black hole merger with total mass 190-265 $M_{\odot}$. **arXiv e-prints**, p. arXiv:2507.08219, jul. 2025. 20

ABBOT, B. P. et al. GWTC-1: a gravitational-wave transient catalog of compact binary mergers observed by LIGO and Virgo during the first and second observing runs. **Physical Review X**, v. 9, n. 3, p. 1–49, 11 2018. Available from: <https://arxiv.org/abs/1811.12907v3>. 15

ABBOTT, B. P. et al. Binary black hole mergers in the first Advanced LIGO observing run. **Physical Review X**, v. 6, n. 4, p. 041015, 10 2016. ISSN 21603308. 3, 15

_____. Observation of gravitational waves from a binary black hole merger. **Physical Review Letters**, v. 116, n. 6, p. 061102, 2 2016. ISSN 10797114. 3, 14, 15, 16

_____. GW170817: observation of gravitational waves from a binary neutron star inspiral. **Physical Reviev Letters**, v. 119, p. 161101, Oct 2017. Available from: <https://link.aps.org/doi/10.1103/PhysRevLett.119.161101>. 16, 17, 18

_____. Multi-messenger observations of a binary neutron star merger. **The Astrophysical Journal Letters**, v. 848, n. 2, p. L12, oct. 2017. ISSN 2041-8213. Available from: <http://dx.doi.org/10.3847/2041-8213/aa91c9>. 17, 18

ABBOTT, R. et al. GWTC-2: Compact Binary Coalescences Observed by LIGO and Virgo during the First Half of the Third Observing Run. **Physical Review X**, v. 11, n. 2, p. 021053, 6 2021. Available from: <https://journals.aps.org/prx/abstract/10.1103/PhysRevX.11.021053>. 15

_____. Observation of gravitational waves from two neutron star–black hole coalescences. **The Astrophysical Journal Letters**, v. 915, n. 1, p. L5, 6 2021. ISSN 2041-8205. Available from: <https://iopscience.iop.org/article/10.3847/2041-8213/ac082ehttps://iopscience.iop.org/article/10.3847/2041-8213/ac082e/meta>. 19

_____. GWTC-3: Compact binary coalescences observed by ligo and virgo during the second part of the third observing run. **Physical Review X**, v. 13, n. 4, dec. 2023. ISSN 2160-3308. Available from: <http://dx.doi.org/10.1103/PhysRevX.13.041039>. 15

ADHIKARI, R. X. et al. A cryogenic silicon interferometer for gravitational-wave detection. **Classical and Quantum Gravity**, v. 37, n. 16, 1 2020. Available from: <http://arxiv.org/abs/2001.11173http://dx.doi.org/10.1088/1361-6382/ab9143>. 34, 35, 36, 37, 92

AGUIAR, O. D. Past, present and future of the resonant-mass gravitational wave detectors. **Research in Astronomy and Astrophysics**, v. 11, n. 1, p. 1–42, dec. 2010. ISSN 1674-4527. Available from: <http://dx.doi.org/10.1088/1674-4527/11/1/001>. 23

AMANN, F. et al. Site-selection criteria for the einstein telescope. **Review of Scientific Instruments**, v. 91, n. 9, sep. 2020. ISSN 1089-7623. Available from: <http://dx.doi.org/10.1063/5.0018414>. 41

ANDERSON, C. T. The heat capacity of silicon at low temperatures1. **Journal of the American Chemical Society**, v. 52, n. 6, p. 2301–2304, 1930. Available from: <https://doi.org/10.1021/ja01369a017>. 48

BAJPAI, R. et al. Vibration analysis of kagra cryostat at cryogenic temperature. **Classical and Quantum Gravity**, v. 39, n. 16, p. 165004, jul 2022. Available from: <https://dx.doi.org/10.1088/1361-6382/ac7cb5>. 95

BONILLA, E.; SHAPIRO, B.; LANTZ, B.; AGUIAR, O. D.; CONSTANCIO, M. Noise requirements of the cryogenic shielding for next generation cryocooled gravitational wave observatories: newtonian noise. **Physical Review D**, v. 104, n. 12, p. 122005, 12 2021. ISSN 24700029. Available from: <https://journals.aps.org/prd/abstract/10.1103/PhysRevD.104.122005>. 95, 104

BRAND, J. V. D. Seismic noise and gravity-gradient noise. In: REITZE, D.; SAULSON, P.; GROTE, H. (Ed.). **Advanced interferometric**

gravitational-wave detectors: in 2 volumes. New Jersey: World Scientific Publishing Co., 2019. v. 1, chapter 6, p. 161–184. ISBN 9789813146082. Available from: <https://www.worldscientific.com/doi/abs/10.1142/9789813146082_0006>. 31, 33

BUIKEMA, A. et al. Sensitivity and performance of the advanced ligo detectors in the third observing run. American Physical Society (APS), v. 102, n. 6, sep. 2020. ISSN 2470-0029. Available from: <http://dx.doi.org/10.1103/PhysRevD.102.062003>. 28, 29, 30, 33

CAPOTE, E. et al. Advanced LIGO detector performance in the fourth observing run. **arXiv e-prints**, p. arXiv:2411.14607, nov. 2024. 30, 31

CENGEL, Y. **Heat transfer: a practical approach**. McGraw-Hill, 2003. (McGraw-Hill series in mechanical engineering). ISBN 9780072458930. Available from: <https://books.google.com.br/books?id=nrbfpSZTwskC>. 43

CERVANTES-COTA, J. L.; GALINDO-URIBARRI, S.; SMOOT, G. F. A brief history of gravitational waves. **Universe**, v. 2, n. 3, p. 22, 9 2016. Available from: <https://www.mdpi.com/2218-1997/2/3/22/htmhttps://www.mdpi.com/2218-1997/2/3/22>. 2

CHATTOPADHYAY, D. et al. Modelling the formation of the first two neutron star–black hole mergers, gw200105 and gw200115: metallicity, chirp masses, and merger remnant spins. **Monthly Notices of the Royal Astronomical Society**, v. 513, n. 4, p. 5780–5789, may 2022. ISSN 1365-2966. Available from: <http://dx.doi.org/10.1093/mnras/stac1283>. 19

CHRISTENSEN, N. Stochastic gravitational wave backgrounds. **Reports on Progress in Physics**, v. 82, n. 1, 11 2018. Available from: <https://arxiv.org/abs/1811.08797v1>. 14

CONSTANCIO, M. et al. Silicon emissivity as a function of temperature. **International Journal of Heat and Mass Transfer**, v. 157, p. 119873, 8 2020. ISSN 00179310. 25, 46, 79, 81, 86, 87, 88, 120

D'ORAZIO, D. J. et al. Multimessenger constraints on magnetic fields in merging black hole–neutron star binaries. **The Astrophysical Journal**, v. 927, n. 1, p. 56, mar. 2022. ISSN 1538-4357. Available from: <http://dx.doi.org/10.3847/1538-4357/ac4bdb>. 19

EDWARDS, D. F.; OCHOA, E. Infrared refractive index of silicon. **Applied Optics**, v. 19, n. 24, p. 4130–4131, Dec 1980. Available from: <https://opg.optica.org/ao/abstract.cfm?URI=ao-19-24-4130>. 76

EFFLER, A.; FRITSCHEL, P.; HALL, E. D.; LANDRY, M.; LAZZARINI, A.; O'REILLY, B.; REITZE, D. H.; SHOEMAKER, D.; C., T. **A Roadmap for the LIGO Observatories in the Era of Cosmic Explorer**. 2023. Available from: <https://dcc.ligo.org/public/0188/M2300107/005/ngGW_MPSAC_Laboratory_White_Paper_LIGO-M2300107-v5.pdf>. 36, 38

ETC, S. C. **Einstein Telescope: science case, design study and feasibility report**. 2020. Available from: <https://apps.et-gw.eu/tds/?r=17196>. 40

_____. **ET design report**. 2024. Available from: <https://apps.et-gw.eu/tds/ql/?c=15418>. 39, 40, 41, 46

EVANS, M. et al. **A horizon study for cosmic explorer: science, observatories, and community**. 2021. Available from: <https://arxiv.org/abs/2109.09882>. 38, 39

FALCIANO, F. T. Geometria, espaço-tempo e gravitação: conexão entre conceitos da relatividade geral. **Revista Brasileira de Ensino de Fisica**, v. 31, n. 4, p. 4308–4317, 10 2009. ISSN 01024744. 1

FLANAGAN, E.; HUGHES, S. A. The basics of gravitational wave theory. **New Journal of Physics**, v. 7, n. 1, p. 249, 9 2005. ISSN 1367-2630. Available from: <https://iopscience.iop.org/article/10.1088/1367-2630/7/1/204https://iopscience.iop.org/article/10.1088/1367-2630/7/1/204/meta>. 10, 13

FONSECA, E. et al. Refined mass and geometric measurements of the high-mass psr j0740+6620. **The Astrophysical Journal Letters**, v. 915, n. 1, p. L12, jul. 2021. ISSN 2041-8213. Available from: <http://dx.doi.org/10.3847/2041-8213/ac03b8>. 19

FOUNDATION, P. S. **Python Programming Language**. 2024. Available from: <https://docs.scipy.org/doc/scipy/reference/generated/scipy.signal.savgol_filter.html>. 51

FREISE, A.; STRAIN, K. Interferometer techniques for gravitational-wave detection. **Living Reviews in Relativity**, v. 13, n. 1, feb. 2015. ISSN 1433-8351. Available from: <http://dx.doi.org/10.12942/lrr-2010-1>. 23

GANAPATHY, D. et al. Broadband quantum enhancement of the ligo detectors with frequency-dependent squeezing. **Phys. Rev. X**, v. 13, p. 041021, Oct 2023. Available from: <https://link.aps.org/doi/10.1103/PhysRevX.13.041021>. 30, 31, 32

GARDON, R. The emissivity of transparent materials. **Journal of the American Ceramic Society**, v. 39, n. 8, p. 278–285, 1956. Available from: <https://ceramics.onlinelibrary.wiley.com/doi/abs/10.1111/j.1151-2916.1956.tb15833.x>. 75, 81

GAZZINELLI, R. **Theory of special relativity**. 2. ed. São Paulo: Blucher Publisher, 2009. 1–160 p. ISBN 9788521204886. 1

HALL, E. D. Cosmic Explorer: a next-generation ground-based gravitational-wave observatory. **Galaxies**, v. 10, n. 4, p. 90, 8 2022. ISSN 2075-4434. Available from: <https://www.mdpi.com/2075-4434/10/4/90/htmhttps://www.mdpi.com/2075-4434/10/4/90>. 38

KAWAMURA, S.; NAKANO, M. Interferometer configuration and response. In: REITZE, D.; SAULSON, P.; P., G. (Ed.). **Advanced interferometric gravitational-wave detectors: in 2 volumes**. New Jersey: World Scientific Publishing Co., 2019. v. 1, chapter 2, p. 33–58. ISBN 9789813146082. 26

KIM, D. S. et al. A nuclear quantum effect with pure anharmonicity and the anomalous thermal expansion of silicon. **Proceedings of the National Academy of Sciences of the United States of America**, National Academy of Sciences, v. 115, n. 9, p. 1992–1997, 10 2016. Available from: <http://arxiv.org/abs/1610.08737http://dx.doi.org/10.1073/pnas.1707745115>. 35

KOKKOTAS, K. D. **Gravitational waves**. 2007. 3891–3923 p. Available from: <https://inspirehep.net/files/3ace6af68a739dcd04d870728dc9695b>. 12, 13

LIENHARD V, J. H.; LIENHARD IV, J. H. **A heat transfer textbook**. 6. ed. Cambridge, MA: Phlogiston Press, 2024. Version 6.00. Available from: <https://ahtt.mit.edu>. 43

LIGO SCIENTIFIC COLLABORATION. **Instrument science white paper**. [S.l.], 7 2021. 1–180 p. Available from: <http://www.ligo.org/>. 3, 37, 45, 46, 97

LOCKERBIE, N. A.; XU, A.; VERYASKIN, A. V. The gravitational coupling between longitudinal segments of a hollow cylinder and an arbitrary gravitational source: relevance to the step experiment. **Classical and Quantum Gravity**, IOP Publishing, v. 13, n. 8, p. 2041, 1996. 96

MAGGIORE, M. **Gravitational aves. Volume 1: theory and experiments**. New York: Oxford University Press, 2008. 1–554 p. ISBN 9780191717666. 2, 9, 10, 11, 12, 13, 24, 26

MAIORANO, M.; PAOLIS, F. D.; NUCITA, A. Principles of gravitational-wave detection with pulsar timing arrays. **Symmetry**, v. 13, n. 12, p. 2418, dec. 2021. ISSN 2073-8994. Available from: <http://dx.doi.org/10.3390/sym13122418>. 23

MANSELL, G. L. **Squeezed light sources for current and future interferometric gravitational-wave detectors**. Canberra, 4 2018. 1–182 p. Available from: <https://openresearch-repository.anu.edu.au/handle/1885/154249>. 34, 36

MARKAKIS, C. et al. Neutron star equation of state via gravitational wave observations. **Journal of Physics: Conference Series**, v. 189, n. 1, p. 012024, 10 2009. ISSN 1742-6596. Available from: <https://iopscience.iop.org/article/10.1088/1742-6596/189/1/012024https://iopscience.iop.org/article/10.1088/1742-6596/189/1/012024/meta>. 15

MCCLELLAND, D. E.; MAVALVALA, N.; SCHNABEL, R. Quantum noise. In: REITZE, D.; SAULSON, P.; GROTE, H. (Ed.). **Advanced interferometric gravitational-wave detectors: in 2 volumes**. New Jersey: World Scientific Publishing Co., 2019. v. 1, chapter 4, p. 101–135. ISBN 9789813146082. 30

MCIVER, J.; SHOEMAKER, D. H. **Discovering gravitational waves with Advanced LIGO**. [S.l.], 3 2021. 1–37 p. Available from: <https://dcc.ligo.org/DocDB/0172/P2000530/002/aLIGO_Contemporary_Physics_submission.pdf>. 25, 26, 34

MISIAKOS, K.; TSAMAKIS, D. Accurate measurements of the silicon intrinsic carrier density from 78 to 340 K. **Journal of Applied Physics**, v. 74, n. 5, p. 3293–3297, sep. 1993. 78

NAWRODT, R. et al. High mechanical q-factor measurements on silicon bulk samples. **Journal of Physics: Conference Series**, v. 122, n. 1, p. 012008, jul

2008. Available from:
<https://dx.doi.org/10.1088/1742-6596/122/1/012008>. 92

NGUYEN, P. **PEM coupling function tools**. 2018. Available from:
<https://git.ligo.org/philippe.nguyen/pemcoupling>. 111

NGUYEN, P. et al. Environmental noise in advanced ligo detectors. **Classical and Quantum Gravity**, v. 38, n. 14, p. 145001, jun. 2021. ISSN 1361-6382. Available from: <http://dx.doi.org/10.1088/1361-6382/ac011a>. 106, 108, 110

NI, W. **Space gravitational wave detection: progress and outlook**. 2024. Available from: <https://arxiv.org/abs/2409.00927>. 23

PEM, L. **LIGO PEM website**. 2025. Available from:
<https://pem.ligo.org/>. 112, 113

RÄZ, T.; SAUER, T. The collaboration between Marcel Grossmann and Albert Einstein as a case of the application of mathematics. **14th Marcel Grossman Meeting On Recent Developments in Theoretical and Experimental General Relativity, Astrophysics and Relativistic Field Theories, Proceedings**, World Scientific Publishing Co. Pte. Ltd., p. 3368–3371, 2018. Available from: <www.worldscientific.com>. 2

READING, U. of. **Silicon Properties**. 2023. https://www.reading.ac.uk/infrared/library/infraredmaterials/ir-infraredmaterials-si.aspx. 79

REIS, J. A. M.; AGUIAR, O. D. Newtonian noise generated by propellers in ligo voyager cooling-down system. In: **LVK collaboration meeting - march edition**. LVK Collaboration, 2023. Available from:
<https://dcc.ligo.org/LIGO-G2300347>. 117

REIS, J. A. M.; BONILLA, E. L.; AGUIAR, O. D. Newtonian noise introduced by impellers in ligo voyager and cosmic explorer gravitational wave observatories. **Classical and Quantum Gravity**, v. 42, n. 8, p. 085017, apr 2025. Available from: <https://dx.doi.org/10.1088/1361-6382/adbcf3>. 102

REITZE, D. et al. **Cosmic Explorer: the U.S. contribution to gravitational-wave astronomy beyond LIGO**. 2019. Available from:
<https://arxiv.org/abs/1907.04833>. 38

RIEGEL, J.; MAYER, W.; HAVRE, Y. **FreeCAD**. 2021. Available from:
<https://www.freecad.org/>. 68

RILES, K. Recent searches for continuous gravitational waves. **Modern Physics Letters A**, World Scientific Publishing Co. Pte Ltd, v. 32, n. 39, 12 2017. Available from: <https://arxiv.org/abs/1712.05897v1>. 14

ROLLINS, J. G.; HALL, E.; WIPF, C. et al. **Pygwinc: gravitational wave interferometer noise calculator**. 2020. ascl:2007.020 p. Available from: <https://ui.adsabs.harvard.edu/abs/2020ascl.soft07020R/abstract>. 28, 36

ROWAN, S. Thermal noise. In: REITZE, D.; SAULSON, P.; GROTE, H. (Ed.). **Advanced interferometric gravitational-wave detectors: in 2 volumes**. New Jersey: World Scientific Publishing Co., 2019. v. 1, chapter 5, p. 137–160. ISBN 9789813146082. 30, 35

SATHYAPRAKASH, B. S.; SCHUTZ, B. F. Physics, astrophysics and cosmology with gravitational Waves. **Living Reviews in Relativity 2009 12:1**, v. 12, n. 1, p. 1–141, 12 2009. ISSN 1433-8351. Available from: <https://link.springer.com/article/10.12942/lrr-2009-2>. 11

SHOEMAKER, D. H. et al. **Next generation observatories – report from the Dawn VI Workshop; October 5-7 2021**. 2022. Available from: <https://arxiv.org/abs/2112.12718>. 38

SIEGEL, R. **Thermal radiation heat transfer**. 4. ed. Taylor & Francis, 2001. ISBN 9781560328391. Available from: <https://books.google.com.br/books?id=O389yQ0-fecC>. 44, 45

THORNE, K. Gravitational radiation. In: HAWKING, S.; ISRAEL, W. (Ed.). **Three hundred years of gravitation**. Cambridge: Cambridge University Press, 1989. chapter 9, p. 330–458. ISBN 0521379768. Available from: <https://ui.adsabs.harvard.edu/abs/1989thyg.book..330T>. 2, 23

WALDMAN, S. J. The advanced ligo gravitational wave detector. **arXiv**, 2011. Available from: <https://arxiv.org/abs/1103.2728>. 25

WEBER, J. **Gereral relativity and gravitational waves**. New York: Interscience Publishers, 1961. 200 p. ISBN 9781258821036. 11

_____. Gravitational shielding and absorption. **Physical Review**, v. 146, n. 4, p. 935–937, 6 1966. ISSN 0031899X. Available from: <https://journals.aps.org/pr/abstract/10.1103/PhysRev.146.935>. 2

WEISS, R. Gravitational waves and their interactions with detectors. In: REITZE, D.; SAULSON, P.; GROTE, H. (Ed.). **Advanced interferometric gravitational-wave detectors: in 2 volumes**. New Jersey: World Scientific Publishing Co., 2019. v. 1, chapter 1, p. 3–31. ISBN 9789813146082. Available from: <www.worldscientific.com>. 23, 28, 31

WOOSLEY, S. E.; HEGER, A. The pair-instability mass gap for black holes. **The Astrophysical Journal Letters**, American Astronomical Society, v. 912, n. 2, p. L31, may 2021. ISSN 2041-8213. Available from: <http://dx.doi.org/10.3847/2041-8213/abf2c4>. 20

YAMADA, T. et al. High performance thermal link with small spring constant for cryogenic applications. **Cryogenics**, v. 116, p. 103280, 2021. ISSN 0011-2275. Available from: <https://www.sciencedirect.com/science/article/pii/S0011227521000382>. 95

PUBLICAÇÕES TÉCNICO-CIENTÍFICAS EDITADAS PELO INPE

Teses e Dissertações (TDI)

Teses e Dissertações apresentadas nos Cursos de Pós-Graduação do INPE.

Notas Técnico-Científicas (NTC)

Incluem resultados preliminares de pesquisa, descrição de equipamentos, descrição e ou documentação de programas de computador, descrição de sistemas e experimentos, apresentação de testes, dados, atlas, e documentação de projetos de engenharia.

Propostas e Relatórios de Projetos (PRP)

São propostas de projetos técnico-científicos e relatórios de acompanhamento de projetos, atividades e convênios.

Publicações Seriadas

São os seriados técnico-científicos: boletins, periódicos, anuários e anais de eventos (simpósios e congressos). Constam destas publicações o Internacional Standard Serial Number (ISSN), que é um código único e definitivo para identificação de títulos de seriados.

Pré-publicações (PRE)

Todos os artigos publicados em periódicos, anais e como capítulos de livros.

Manuais Técnicos (MAN)

São publicações de caráter técnico que incluem normas, procedimentos, instruções e orientações.

Relatórios de Pesquisa (RPQ)

Reportam resultados ou progressos de pesquisas tanto de natureza técnica quanto científica, cujo nível seja compatível com o de uma publicação em periódico nacional ou internacional.

Publicações Didáticas (PUD)

Incluem apostilas, notas de aula e manuais didáticos.

Programas de Computador (PDC)

São a seqüência de instruções ou códigos, expressos em uma linguagem de programação compilada ou interpretada, a ser executada por um computador para alcançar um determinado objetivo. Aceitam-se tanto programas fonte quanto os executáveis.